Coupling between optical Tamm states and fluorescent nanocrystals ; determination of the dipole nature of single colloidal nanoplatelets

Fu Feng

THESE DE DOCTORAT de l'Université Pierre et Marie Curie

Spécialité

La physique, de la particule à la matière condensée

Présentée par

Fu FENG

Pour obtenir le grade de

DOCTEUR de l' UNIVERSITÉ PIERRE ET MARIE CURIE

Coupling between optical Tamm states and fluorescent nanocrystals; determination of the dipole nature of single colloidal nanoplatelets

---

Thèse dirigée par Laurent COOLEN

à l'Institut des NanoSciences de Paris

Soutenance prévue le 19 Septembre 2016

devant le jury composé de:

Anna Rodina (Rapportrice)

Joel Bellessa (Rapporteur)

Benoit Dubertret (Examinateur)

Jean-Pierre Hermier (Examinateur)

Nicolas Treps (Examinateur)

Agnes Maitre (Membre invitée)

Laurent Coolen (Directeur de thèse)

Contents

Introduction

Introduction

Technological progress in the recent 30 years for reducing the size of semi-conductor materials offers the possibility to fabricate devices in which the electrons and holes are confined in a very small volume in three dimensions. When the dimension of the material is small (a few nanometers), the charges experience quantum confinement effects. This kind of nanomaterial is called nanocrystal or quantum dot [1]. These structures have the remarkable property that the energy levels are discretized, in a sense making them artificial atoms.

At the beginning of 1980s, Efros, Ekimov et al. started the growth of II/VI semi-conductor nanocrystals in a vitreous matrix [2]. A few years later, colloidal synthesis methods were developed and nanocrystals with increasingly good optical properties were obtained [3–5]. These emitters have drawn intense attention because of their versatile manipulation in solution and biochemical functionalization, high quantum efficiency, and photostability, tunable emission wavelength and broad absorption spectrum. By fluorescence microscopy, it is possible to study the optical properties of individual nanocrystals ; non-classical effects such as single photon emission (even for nanocrystals at room temperature) are evidenced.

Studying individual nano-emitters offers new ways to test the concepts of electromagnetics in the visible domain. Other manipulations are possible by nano-structuring the environment around an emitter ; for instance, the use of antennas, which is ubiquitous in the radio and microwave domains, can be extended to nano-photonics, provided that sufficiently precise nano-fabrication techniques are available. The group "Nanophotonics and quantum optics" at the Institut de NanoSciences de Paris (INSP) studies how to manipulate light by coupling fluorescent emitters (individually or collectively) with their optical environment. The emission

properties of nanoemitters depend strongly on their optical environment. This is expressed, as for the decay time of a radiating dipole, by Fermi's golden rule :

$$T_{i\to f} = \frac{2\pi}{\hbar}| < f|H'|i > |^2\rho(\omega) \quad (1)$$

where $|i>$ and $|f>$ are the initial and final state of the nanoemitter transition ; the polarization of these states can influence highly the emission properties (determined by the symmetries of the transition and its associated orientation). ρ is the local state density which is mainly determined by the optical environment around the emitter and depends on the emission angular frequency ω. The electric field at the emitter position is included in the hamiltonian H' (for a dipolar electric transition). Previously, our team has studied the coupling between the nanocrystal and different nanophotonic structures such as photonic crystals, plasmonic structures, plasmonic patch antennas etc...

Subject and outline of the thesis

My thesis can be divided mainly into three parts. In the first chapter, I give a general description of the colloidal nanocrystals with some examples of their main optical properties. I then present the homemade fluorescence microscope which I built during this PhD project, together with various detection systems : Hanbury-Brown and Twiss analysis, Michelson interferometry, decay curves... Of special interest to this thesis will be the measurement of the emission angular distribution (radiation pattern), by imaging in the Fourier plane, possibly combined with spectroscopy. The Fourier plane of the sample is coupled with an EMCCD camera so that the emission pattern can be analyzed. At last, the Fourier plane of the sample can also be coupled with the entrance slit of a spectrometer so that the CCD camera coupled with the spectrometer yield directly the emission dispersion relation.

The second part of my thesis describes the study of the coupling between nanocrystals and optical Tamm states, which are electromagnetic states confined at the interface between a Bragg mirror and a metallic surface. We successfully coupled a layer of colloidal CdSe/CdS nanocrystal with 2D and 0D optical Tamm structure. The lateral confinement effects introduced by the limited radius of the metallic disk were evidenced. We have also studied the emission dispersion relation from different portions of the optical Tamm structure and highlight the

relation between the electromagnetic field phase gradient and the emission pattern. Finally, by exciting different positions in the nanocrystals layer, we demonstrated that the emission direction is highly dependent on the position of the emitters.

In the third part of the thesis, we demonstrate a method to determine the emission dipole nature (linear 1D dipole or 2D dipole, incoherent sum of two 1D dipoles) and its associated orientation. The main idea of the method is to measure the emission pattern and emission polarization from a single emitter simultaneously. For an appropriate substrate (gold or glass), these measurements can provide very different results depending on the 1D or 2D nature of the dipole, so that we can determine whether the emitter is 1D or 2D. This method is applied to the study of colloidal nanoplatelets. Perfect agreements between the theoretical calculations and experimental measurements confirm that the emission from square nanoplatelets can be well described by a 2D dipole in the plane of the emitter. Studies on rectangular nanoplatelets also show us the influence of asymmetric core and shell shape of the emitter on the emission.

In the end, a short conclusion and some perspectives will be given.

Bibliography

[1] M. A. Reed, J. N. Randall, R. J. Aggarwal, R. J. Matyi, T. M. Moore, and A. E. Wetsel. Observation of discrete electronic states in a dimensional semiconductor nanostructure. *Phys. Rev. Lett*, 60(6):535 – 537, 1988.

[2] A.I. Ekimov, A.L. Efrs, and A.A. Onushchenko. Quantum size effect in semiconductor microcrystals. *Solid State Comm*, 56(11):921 – 924, 1985.

[3] C.B. Murray, D.J. Norris, and M.G. Bawendi. Synthesis and characterization of nearly monodisperse CdE (E=S,Se,Te) semiconductor nanocrystallite. *J. Am. Chem. Soc.*, 115(19):8706 – 8715, 1993.

[4] A.P. Alivisatos. Semiconductor clusters, nanocrystals, and quantum dots. *Science*, 271(5251):933 – 937, 1996.

[5] M.A. Hines and P. Guyot-Sionnest. Synthesis and characterization of strongly luminescing zns-capped cdse nanocrystals. *J. Phys. Chem.*, 100(2):468 – 471, 1996.

Chapter 1

Microphotoluminescence set-up with Fourier plane spectroscopy

Introduction

Fluorescence microscopy is a widespread tool, especially for biological observation. When fluorescent emitters such as molecules or semiconductor nanocrystals are sufficiently dispersed over a sample (separated by at least a few microns), it is possible to observe them individually. Various luminescence properties can be characterized, such as emission dynamics (decay curve), intensity fluctuations and correlations (possibly demonstrating single-photon emission), emission angular distribution (radiation pattern), spectrum, polarization etc.

This chapter will give a general introduction on colloidal nanocrystals and also present the home made fluorescence microscope which was installed at INSP as the beginning of this PhD work.

In the first section, we make a brief recall of the physical modelling of colloidal nanocrystals, and of the main physical mechanisms involved in the emission properties of nanocrystals such as confinement effect, Auger recombination etc... We will also present the main experimental emission properties of colloidal CdSe/CdS nanocrystals : absorption/emission spectra, decay curves, single photon emission properties etc...

In the second section, we will present the fluorescence microscope which was installed for this PhD with different detection possibilities. The method for measuring the angular-resolved

emission pattern (Fourier plane) will be discussed in detail as it will be used widely in the next chapters.

1.1 Optical properties of colloidal CdSe/CdS nanocrystals

1.1.1 Colloidal semiconductor nanocrystals

Colloidal semiconductor nanocrystals have raised widespread attention over the last 30 years. They present attractive optical properties such as a broad absorption continuum, room temperature emission, single-photon emission, tunable emission wavelength and good photostability, which can be used for applications like quantum computation, biological imaging, LEDs, micro and nanolasers as well as energy harvesting, photon detection...

The colloidal nanocrystal being used today are generally core/shell structures. The shell allows to protect the core of the nanocrystal from its environment and improve its emission intensity and photostability.

When the dimension of a semiconductor material is reduced to nanometer scale, the electronic and photonic properties of the material will be changed due to the confinement effects, as will be discussed below. The first colloidal semiconductor nanocrystals were reported during the same period by L. Brus [1] and A. Henglein [2]. In 1993, the first organometallic synthesis, which allows the material to reach nanometer scale with high control of the diameter dispersion, was reported by M. G. Bawendi [3]. Since then, different synthesis were reported to obtain different semiconductor nanocrystals shapes and materials among which CdSe is the most used for emission in the visible range. Figure 1.1 is a schematic representation from [4].

1.1.2 Theoretical description of colloidal nanocrystals energy levels

Bulk semiconductor band structure

Cadmium selenide (CdSe) is a direct semiconductor of which the band gap separates the conduction band (c) and valence band (v). The width of the band gap is $E_g = 1.74eV$ for CdSe in wurtzite crystallography at room temperature.

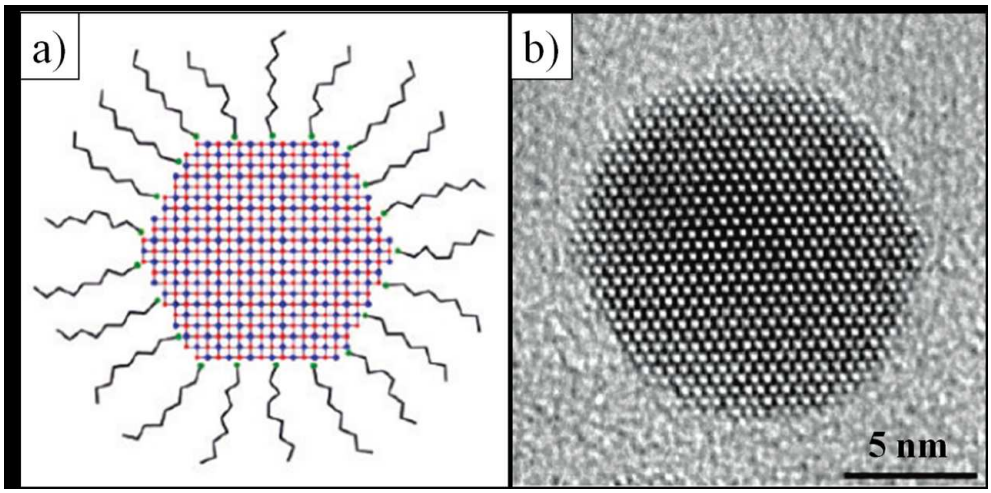

Figure 1.1: a) Schematic representation of a semiconductor nanocrystal with ligands. b) A TEM image of semiconductor nanocrystal (images from ref [4])

The bottom of the conduction band is essentially constituted by the S layer of the cadmium which has an orbital momentum $l_e = 0$ so that the structure of the bottom conduction band is simple and degenerated to two levels because of the spin of the electrons. However, the top of the valence band is principally constituted by the orbitals (P_x, P_y, P_z) of the selenium so that the valence band is degenerated to 6 different levels by the spin of the hole and its orbital momentum. We give below a detailed description of these band structures.

According to Bloch theory, the wave function of in a crystalline solid can be expressed [5] as a sum of the eigenvectors :

$$\Psi^{c,v}(\vec{r}) = u_k^{c,v}(\vec{r}) * \exp(i\vec{k}.\vec{r}) \tag{1.1}$$

of which $u_k^{c,v}(r)$ is the Bloch function, which has the periodicity of the crystalline structure, while the term $\exp(i\vec{k}.\vec{r})$describes the propagative aspect of the wave. For most semiconductor materials, the function $u_k^{c,v}(\vec{r})$ has a weak dependance on the $\vec{k}$ vector. For the purpose of describing semiconductor nanocrystals, we will study the band structure only around $\vec{k} = \vec{0}$.

For CdSe, at $\vec{k} = \vec{0}$, the valence band is degenerated in three bands : the heavy hole (hh) band, the light hole (lh) band, and a third band split-off (so) by the spin-orbit interactions. The coupling between the spin s of an electron and its orbital momentum l leads to introduce a new quantum number $J = s + l$. For the hole, this quantity J_h can take the value $J_h = \frac{3}{2}$ or $J_h = \frac{1}{2}$. The projection of J_h on the c axis for the wurtzite crystallographic structure is a

quantum number labelled M_{J_h} which takes values from $+J_h$ to $-J_h$. Because the eigen state of J_h should be the same as s_h and l_h, the interaction would then separate the band corresponds to the different values of J_h [6]. The bands corresponding to $J_h = \frac{3}{2}$ and $J_h = \frac{1}{2}$ will then be separated, and correspond respectively to the light/heavy hole bands and to the split-off band. For $k = 0$, for CdSe, the splitting between these bands is $\Delta_{so} = 0.413\,\text{meV}$. The heavy hole and light hole bands correspond respectively to $M_{J_h} = \pm\frac{3}{2}$ and $M_{J_h} = \pm\frac{1}{2}$. For the wurtzite crystalline structure, there is an energy difference between these two bands: $\Delta_{int} = 25meV$. The Bloch functions of these different bands can be written as follows:

- For the conduction band:

$$u^c_{1/2,-1/2} = S\uparrow \tag{1.2}$$

$$u^c_{1/2,+1/2} = S\downarrow \tag{1.3}$$

- For the heavy hole:

$$u^h_{3/2,+3/2} = \frac{1}{\sqrt{2}}(X + iY)\uparrow \tag{1.4}$$

$$u^h_{3/2,-3/2} = \frac{1}{\sqrt{2}}(X - iY)\downarrow \tag{1.5}$$

- For the light hole:

$$u^h_{3/2,+1/2} = \frac{i}{\sqrt{6}}[(X + iY)\downarrow -2Z\uparrow] \tag{1.6}$$

$$u^h_{3/2,-1/2} = \frac{1}{\sqrt{6}}[(X - iY)\downarrow +2Z\uparrow] \tag{1.7}$$

- and finally for the 'split-off' band

$$u^h_{1/2,+1/2} = \frac{1}{\sqrt{3}}[(X + iY)\downarrow +Z\uparrow] \tag{1.8}$$

$$u^h_{1/2,-1/2} = -\frac{1}{\sqrt{3}}[(X - iY)\downarrow -Z\downarrow] \tag{1.9}$$

The symbol $\uparrow$ and $\downarrow$ corresponds to the spin up $(+1/2)$ and spin down $(-1/2)$ of electrons and holes. To understand the Bloch function is the first step to understand the physical origin of certain emission properties from nanocrystals (emission polarisation, emission pattern, lifetime etc....) and also the mechanism of interband transitions of semiconductor colloidal nanocrystals.

Effective mass approximation

If we investigate only the part which is close to the minimum energy part of the conduction band and the maximum energy part of the valence band, we can use the effective mass [5] approximation to describe these bands as follows :

For the conduction band, the band structure relation $E(\vec{k})$ is approximated by a parabol (the curve is reduced to its lowest -second- order in k) which can be written as:

$$E^c(k) = E_g + \frac{\hbar^2 k^2}{2m_e^*} \tag{1.10}$$

so that an effective mass m_e^* is defined for the electron (and given by the curvature of the conduction band).

For the valence band, the equation for the holes can be written as:

$$E^{v_i}(k) = -\frac{\hbar^2 k^2}{2m_i^*} + E_0^{v_i} \tag{1.11}$$

where v_i describes which valence band is considered and m_i^* the effective mass of the hole.

At k = 0, $E_0^{v_i}$ is labelled as :

$$E^{v_i} = \begin{cases} 0 \quad \text{for } i = hh \\ -\Delta_{int} \quad \text{for } i = lh \\ -\Delta_{so} - \dfrac{\Delta_{int}}{2} \quad \text{for } i = so \end{cases} \tag{1.12}$$

For CdSe, $m_e^* = 0.14m_0$, $m_{hh}^* = 1.14m_0$, $m_{lh}^* = 0.32m_0$, $m_{so}^* = 0.45m_0$ [7] of which m_0 is the mass of a free electron.

Figure 1.2 plots the band structure of bulk CdSe. The left figure is the band structure with zinc-blende structure and the right figure is with wurtzite structure. Near $k = 0$, the valence band and the conduction band can be described by parabols of which the curvature corresponds to different effective masses. E_g is the energy gap of the stop band of CdSe. By the spin-orbit coupling, the *so* band is degenerate about $\Delta_{so} = 0.413$ eV with respect to the light and heavy hole bands. For the wurtzite structure, the hh and lh are separated by around $\Delta_{int} = 26meV$ (while for the zinc-blende structure $\Delta_{int} = 0$).

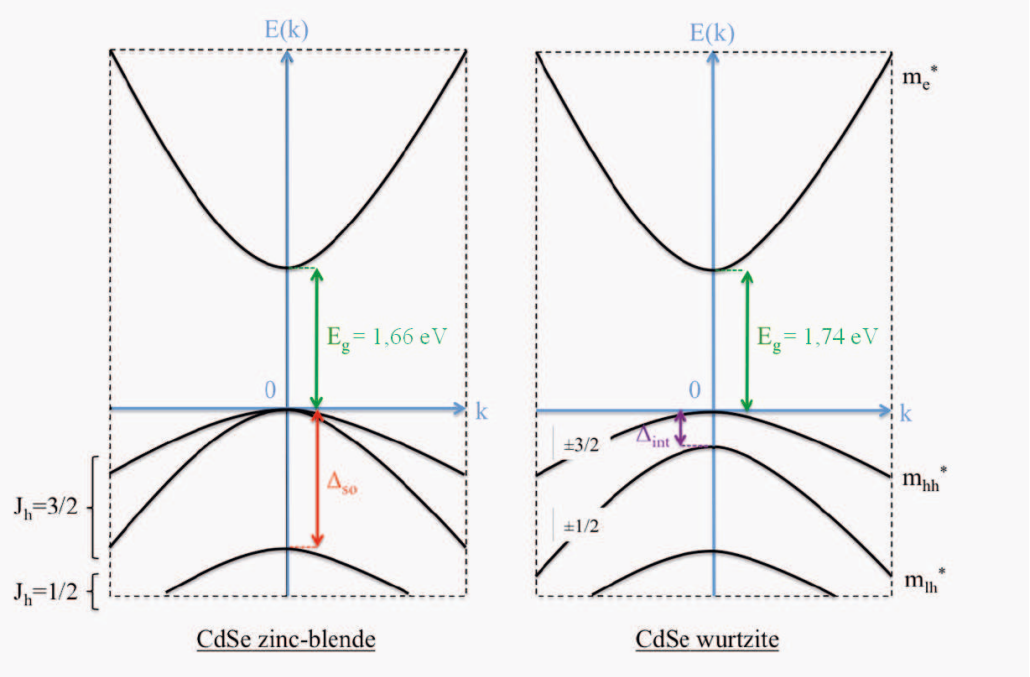

Figure 1.2: Band structure of bulk CdSe for different crystallographic structures [8]

Exciton in the bulk semiconductor materials

Absorbing a photon with energy $h\nu$ higher than E_g would allow an electron to go from the valence band to the conduction band which is empty when the material is not excited. This absorption will then create an electron-hole pair with an electron in the conduction band and a hole at the valence band. Within the effective mass approximation, the electron and hole constitute two quasi-particles of respective masses m_e^* and m_h^* and charges $-e$ and $+e$, interacting by Coulomb forces. This electron-hole pair, bound by coulombian interaction, is called an exciton. The distance between the electron and the hole is the exciton Bohr radius which is around 5.6 nm for CdSe [9], and it can be expressed by :

$$a_B = \varepsilon_r \frac{m_0}{m^*} a_0 \tag{1.13}$$

with :

ε_r: dielectric constant of the material

m_0 : mass of a free electron

$m^* = \dfrac{m_e^* m_h^*}{m_e^* + m_h^*}$ is the reduced mass of the exciton

a_0: the Bohr radius of a hydrogen atom

Quantum confinement in semiconductor nanocrystals

The exciton (electron-hole pair) will move freely in space, with an electron-hole distance defined by the Bohr radius. By reducing the size of the material below the thermal de Broglie wavelength of the particles, quantum confinement effects will take place. If the size of the material is smaller than the Bohr radius of the material, the strong confinement effect occurs. In this limit, each charge is treated as a separate confined particle, and the electron-hole interaction is treated later as a perturbation (the term "exciton" is thus not rigourously appropriate in confined 0D systems, although it is often used for convenience). Let us describe, for instance, the confinement in the nanocrystal by a spherical infinite potential (this is a good description of a simple spherical core but might not be appropriate for a core-shell structure as penetration of the charges wave functions into the shell might occur) :

$$V(r) = \begin{cases} 0 & \text{for } r < R \\ \infty & \text{for } r > R \end{cases} \tag{1.14}$$

We will describe the confinement effects for the electron (in the conduction band). The conduction band is then degenerated only by the spin effects as mentioned above. The hole confinement is similar but complicated by the heavy-light hole degeneracy (the full calculation can be found in [8]). By using the effective mass approximation and the Schrdinger equations, we write :

$$[\frac{\hbar^2}{2m_e^*} \bigtriangledown^2 + V(r)]\Phi_e(r) = E_e\Phi_e(r) \tag{1.15}$$

where the wave function has been assumed to write :

$$\Psi_e = u^c(r)\Phi_e(r) \tag{1.16}$$

where $\Phi_e(r)$ is an enveloppe function and contains the confinement effects, and $u^c(r)$ is the same Bloch function as in equation 1.2 and 1.9.

The solution, given the spherical symmetry, will be given by Bessel functions (as expressed in [10, 11]), involving n_e the radial quantum number and l_e the azimuthal quantum number for the enveloppe function. The energy is given by :

$$E^e_{n_e,l_e} = \frac{\hbar^2 k^2_{n_e,l_e}}{2m^*_e} + E_g \tag{1.17}$$

where $1/k_{n_e,l_e}$ is a characteristic length of the Bessel wave function which depends on n_e, l_e and R (R is the radius of the nanocrystal). For example, for the first excited state (called $1S_e$), the factor k_{n_e,l_e} is π/R . So the energy of this level can be written as:

$$E_{1S_e} = \frac{\hbar^2 \pi^2}{2m^*_e R^2} + E_g \tag{1.18}$$

From equation 1.18 we can see that the energy of this state depends strongly on the radius of the nanocrystal (R), which give the reason why the nanocrystal emission wavelength is tunable with the size of the nanocrystal. And the emission energy would decrease as $(1/R^2)$.

1.1.3 Optical properties of CdSe/CdS colloidal nanocrystals

Let us now describe, from an experimental perspective, the optical properties of typical CdSe/CdS nanocrystals. This section will be illustrated with experimental characterizations performed as part of our collaboration with B. Dubertret's group in ESPCI. Our setup for single-emitter characterization will be described later in this chapter.

Absorption and emission spectrum

Figure 1.3 shows typical absorption and emission spectra from CdSe/CdS nanocrystals measured at room temperature in solution. These nanocrystals present a continuous absorption spectrum which covers the entire UV, blue and green part. Some discrete absorption peaks (corresponding to different energy levels) can be seen but not clearly because of the inhomogeneous broadening. The emission peak is centered around 640 nm with a bandwidth of around 40 nm.

As mentioned above, the energy level is strongly influenced by the size of the nanocrystal. Figure 1.4 (a) shows the absorption spectrum of samples of CdSe/CdS nanocrystals with different sizes. As the size of the nanocrystals increases, the absorption peaks are red shifted.

Figure 1.4 (b) shows the dependance of emission spectrum of CdSe/CdS with its size. The emission spectrum is red shifted when the nanocrystals size increases. This behavior is in

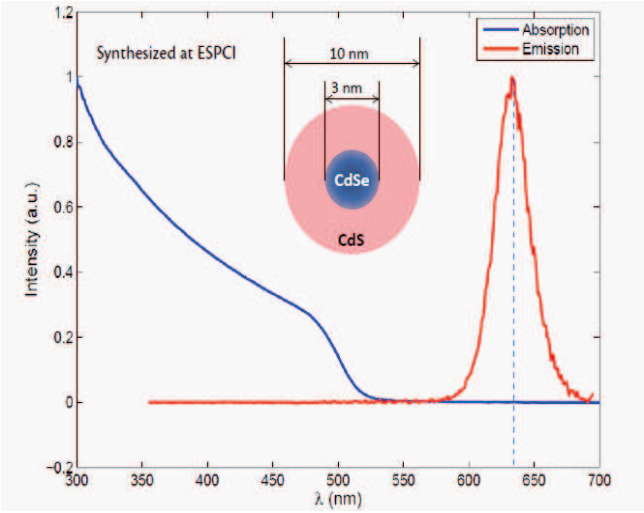

Figure 1.3: Absorption and emission spectrum from core/shell CdSe/CdS nanocrystals(figure from Benoit Dubertret ESPCI).

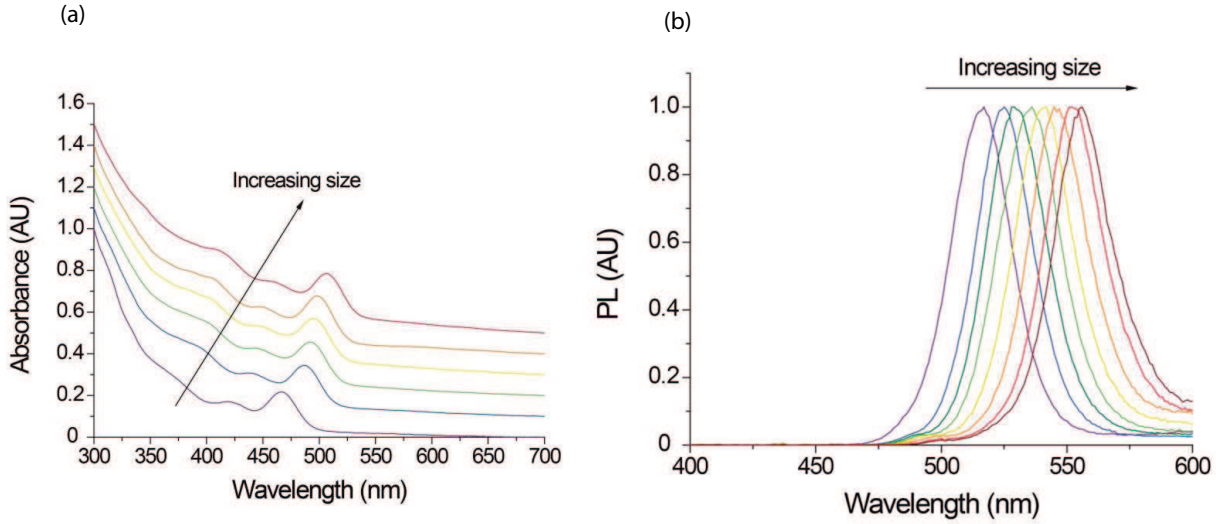

Figure 1.4: (a) Absorption spectrum from core/shell CdSe/CdS nanocrystals [8] for different sizes. (b) Emission spectrum from core/shell CdSe/CdS nanocrystals [8] for different sizes (from 2 nm to 3 nm with 0.2 nm as interval)

qualitative agreement with equation 1.18 : as the nanocrystal radius R increases, the energy of the first excited (emitting) state decreases.

Emission mechanism and emission dynamics

In order to understand the other emission properties (emission dynamics, single photon emission properties), further description of the emission mechanism is given below.

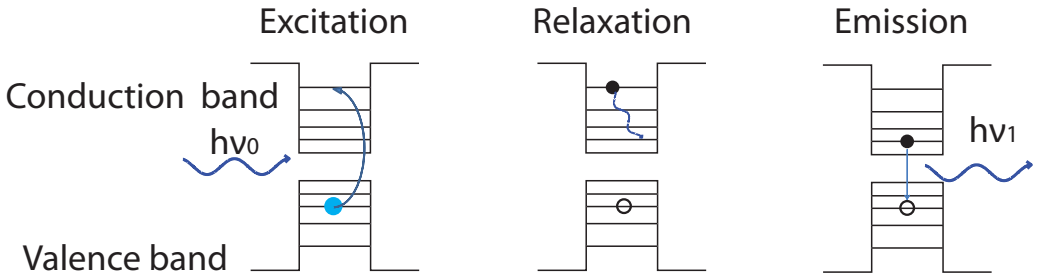

Figure 1.5: Schematic representation of the emission mechanism from a single CdSe/CdS nanocrystal.

Figure 1.5 is a schematic representation of the emission mechanism of a nanocrystal, excited off-resonance. The emitter can be excited by different methods, by light absorption for most studies (fluorescence), but also by an electric current (electroluminescence [12, 13]), by temperature (thermoluminescence [14]) or by an electron beam (cathodoluminescence [15, 16]). An electron-hole pair will then be formed inside the nanocrystal as an electron is promoted from the valence band to the conduction band. For off-resonant excitation, as the excitation energy is higher than the emission energy ($h\nu_0 > h\nu_1$), the created electron-hole pair will first relax to the lowest excited state through the coupling with the phonons. This process is generally very fast (picosecond scale) and without photon emission.

After this relaxation process, there are two possibilities of recombination of the exciton : recombination with photon emission (radiative decay) or recombination without photon emission (non-radiative decay). The radiative recombination is shown in Figure 1.5, and the non-radiative recombination can be due to defects, surface sites or other reasons. Under the assumption that no other state is involved in the recombination process, each recombination can be attributed a characteristic time : we can define γ_R for the radiative decay rate and γ_{NR} for the non-radiative decay rate. In the pulsed excitation regime, between the excitation pulses the population equation of the excited state can then be written as :

$$\frac{dN_e}{dt} = -\gamma_R N_e - \gamma_{NR} N_e \tag{1.19}$$

where N_e is an average number of excited emitters for a collective study, and a probability to be excited for a single-emitter study. By solving this differential equation, the dynamics of the excited state population can be expressed as :

$$N_e(t) = N_e(0)e^{-\gamma t} = N_e(0)e^{-\frac{t}{\tau}} \tag{1.20}$$

of which, $N_e(0)$ is the population at excited state initially, and $\gamma = \gamma_R + \gamma_{NR}$. Equation 1.20 shows that, once the emitter is excited, the population on the excited state will decrease exponentially with a constant $\tau = 1/\gamma = 1/(\gamma_R + \gamma_{NR})$ (exciton lifetime). Let us note that, although the radiative decay is the only one which leads to light detection, the measured decay rate is the sum of the radiative and non-radiative contributions. The experimental emission decay curve will be obtained (for a single emitter) as the histogram of the delays between excitation pulse and photon detection (for instance in fig. 1.8). Under this model, this curve should be an exponential with a characteristic time τ.

Auger recombination

When more than two charges are excited, another decay mechanism appears, the Auger decay, which will play an important role for single-photon emission. Auger decay is a coulombian interaction mechanism between more than two charges, by which an electron-hole pair will recombine non-radiatively by giving its energy to the other charge(s) present in the system. This process in enhanced by the confinement of the charges together in a small volume and, in the case of typical 3-4 nm nanocrystals, is usually much faster than radiative recombination.

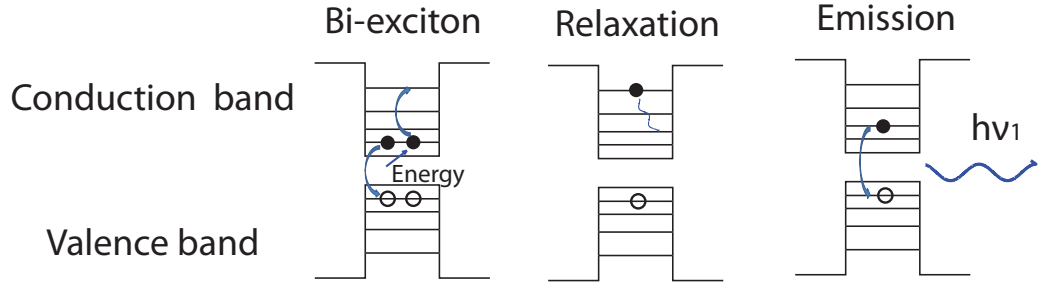

Figure 1.6: Schematic representation of Auger recombination for a nanocrystal.

A first situation involving the Auger effect is described on fig. 1.6. Under high excitation power, more than one electron-hole pair can be excited, creating a multi-exciton (fig. 1.6 shows, for instance, the case of a biexciton). It should then, for a biexciton, be possible to have two simultaneous radiative decays, leading to two photons emitted at the same time. However, as the Auger effect is much faster than radiative recombination, one electron-hole pair will recombine and transfer its energy to the other electron-hole pair. This remaining electron-hole pair will then first loose this received energy by thermalizing to its lowest state, then recombine radiatively (or not), so that (at most) one photon is emitted. Thus, even when the excitation power is high so that more than one electron - hole pair may be excited, eventually only one photon will be emitted at a time. This property is referred to as single-photon emission.

The Auger effect is also in some cases responsible for emission unstabilities : the nanocrystal may be ionized (receive a permanent charge, positive or negative), due to charge exchanges with neighboring traps. When an electron-hole pair is excited in the nanocrystal, the presence of this third permanent charge will induce some Auger effect, by which the electron-hole pair will recombine non-radiatively and give its energy to the third charge. As long as the nanocrystal remains ionized, light emission is thus prevented. By this mechanism, the occasionnal switching between ionized and neutral states is believed to be responsible for the random switching between emitting and non-emitting periods (blinking) which has been observed for many nanocrystals samples.

1.1.4 Emission from CdSe/CdS nanocrystal

In this section, we present some typical emission properties from single CdSe/CdS nanocrystals. The nanocrystals were diluted 10000 times from the mother solution in hexane. 60 μl of the solution were then spin-coated onto a glass surface. A 60-nm layer of PMMA is added (also by spin-coating) on top of the emitters to protect the emitters from being oxidized.

The sample is observed with a fluorescence microscope. The sample is excited by a pulsed laser at 470 nm with a power of 700 nW. The objective of the microscope has a magnification of 60 and a numerical aperture of 0.7.

Figure 1.7 shows some fluctuations for the emission intensity. However, the nanocrystal remains constantly in an emitting state : there is no "off" (non-emitting) period. The fluctu-

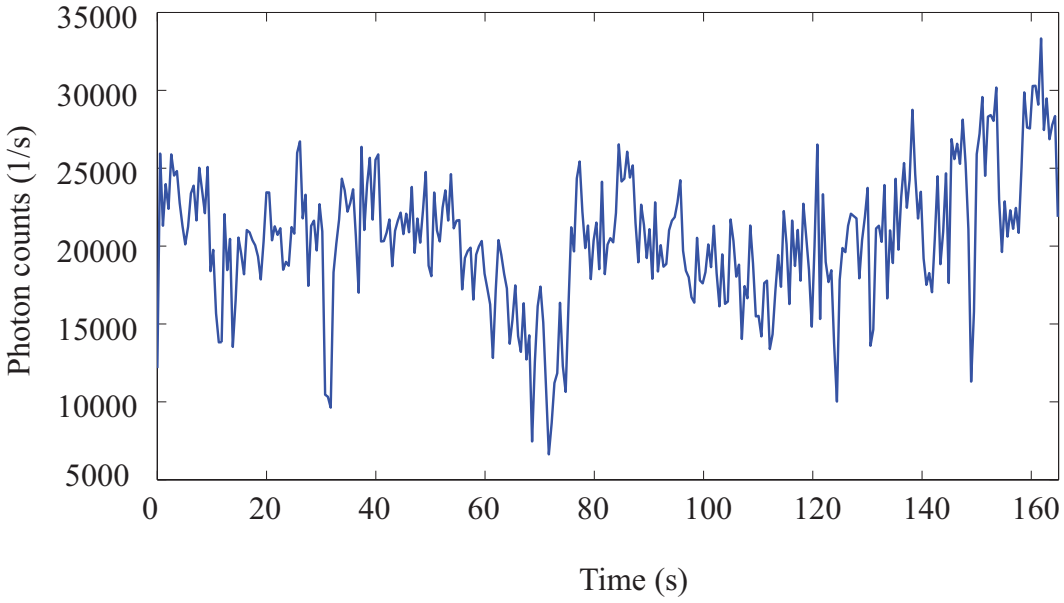

Figure 1.7: Emission intensity (in photon counts per second) from a CdSe/CdS nanocrystal as a function of time.

ations of emission intensity are most likely related to fluctuations of the non-radiative decay component [17].

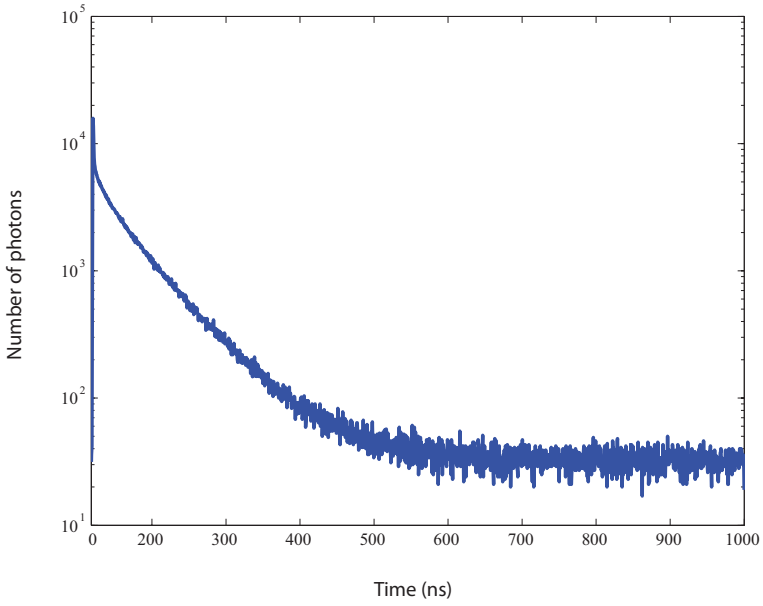

Figure 1.8: Decay time curve for a single CdSe/CdS nanocrystal.

Figure 1.8 shows the emission decay curve of the same single nanocrystal. It presents two components: a very fast decay component (decay time $< 1ns$, faster than the measurement resolution) and a slow exponential decay component (decay time around 30 ns). The faster

component originates probably from some substrate luminescence (and possibly to a weak biexcitonic contribution). The slower emission component can be attributed to the nanocrystal (excitonic) decay and constitutes most of the emission signal.

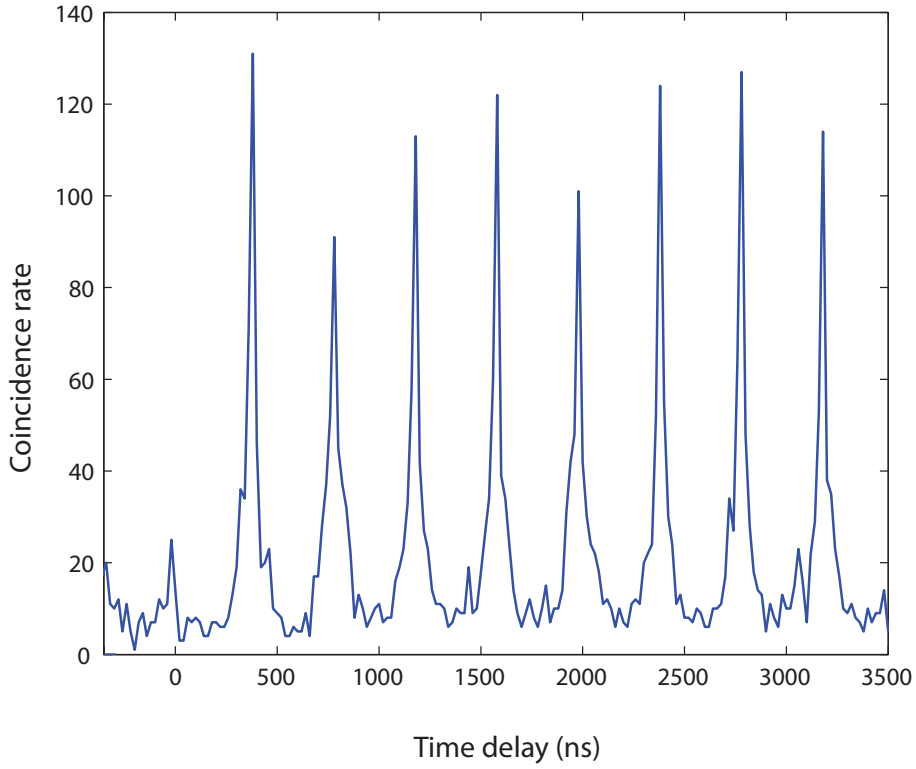

Figure 1.9: Emission intensity correlations from a CdSe/CdS nanocrystal.

Finally, figure 1.9 shows the emission intensity correlation measurement (histogram of the delays between successive photon detections). The figure shows that the coincidence rate at zero delay ($\tau_{delay} = 0$) is very low, meaning that two photons are almost never emitted simultaneously : the CdSe/CdS core/shell nanocrystal is a good single-photon source.

1.2 Design of the set-up

During the thesis, I installed a new set-up based on a home-made fluorescence microscope with different detection systems. Figure 1.10 shows a schematic presentation of the general experimental set-up.

The sample holder can be adapted to samples at room temperature and at cryogenic temperature (inside a helium-flux cryostat). An objective with a numerical aperture of 0.7 and 60

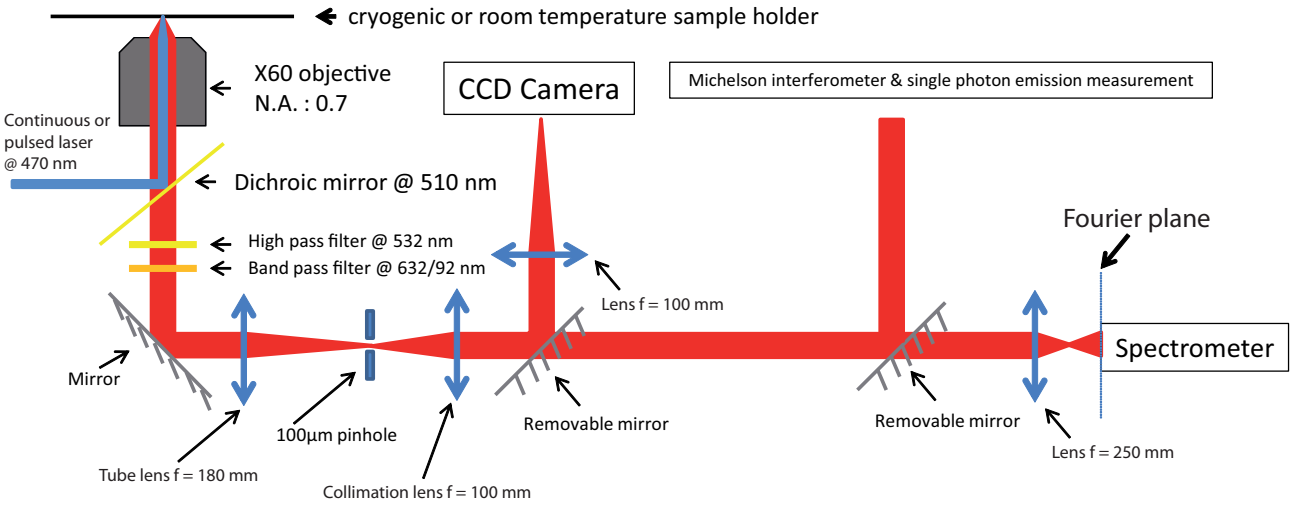

Figure 1.10: Schematic presentation of the set-up

as magnification is installed on two piezo-electric stages (XY and Z). A rough positionning of the sample with respect to the objective can be achieved by adjusting the manual linear translation stages on the sample holder (with a precision of 1 μm). The piezo-electric stages allow a more precise positionning (with a precision of around 2 nm). Blue excitation light (either from a mercury lamp with a filter centered at 450 nm with a bandwidth of 70 nm or a diode laser at 470 nm with both pulsed and continuous modes) is reflected by a dichroic mirror with a cut wavelength at 510 nm. The beam is then focused by the objective onto the sample. Emission from the sample is collected by the same objective and filtered by the dichroic. An intermediate image plane is then formed on which a pinhole can be placed to perform a spatial selection. The beam is then collimated by the collimation lens and sent to the detection systems.

There are three different detection systems :

1. Direct imaging with the help of a charge coupled device (CCD) camera

2. Combination of Hanbury-Brown and Twiss (HBT) set-up together with a Michelson interferometer

3. Fourier plane measurement system with different possible configurations

In the following sections, we first present briefly the first two detection possibilities. We then discuss more precisely the measurements with Fourier plane, which will be used in the third chapter of this manuscript.

1.2.1 CCD camera imaging

As shown in Figure 1.10, for direct imaging of the fluorescence pattern from the sample, the collimated beam is refocused onto a CCD camera. The CCD camera has 1392 x 1040 pixels, the size of each pixel is 4.65 μm x 4.65 μm. The imaging field of view is typically 20x20 μm^2.

The CCD system can be used to image the sample and for dynamic studies in the ms range.

1.2.2 Hanbury-Brown and Twiss set-up and Michelson interferometer

A second detection system was a combination of Hanbury - Brown and Twiss (HBT) set-up and Michelson interferometer. This system, with detection by avalanche photodiodes, gives the possibility to study the emission dynamics from emitters with nanosecond resolution.

Figure 1.11 is a representation of the detection configuration. The incoming beam is separated by the 50/50 non-polarizing beam splitter cube. The two separated beams are then reflected by two retro-reflectors of which one is on a motorized linear translation stage that creates a delay between the two beams. The two beams are then recombined by the 50/50 cube beam splitter and focused by lenses onto two avalanche photodiodes. The two photodiodes are coupled with an electronic start/stop acquisition system which is synchronized with the pulsed laser controller, and it records the arrival time of each photon and the diode by which the photon is detected. The system also records the time delay between a photon and the previous laser pulse.

This detection system provides the following informations :

- The decay curve (fig. 1.8) is obtained as the histogram of the delays between a photon detection and the previous laser pulse.
- The interferogram (plot of the intensity on one photodiode as a function of the interferometer path difference) provides the coherence time of the emitted photons.
- The antibunching curve is obtained as the histogram of the delays τ between two successive photons. This curve corresponds to the emitted electric field second-order correlation function $g^2(\tau)$ (or intensity correlation). A single-photon beam is defined by $g^2(0) = 0$

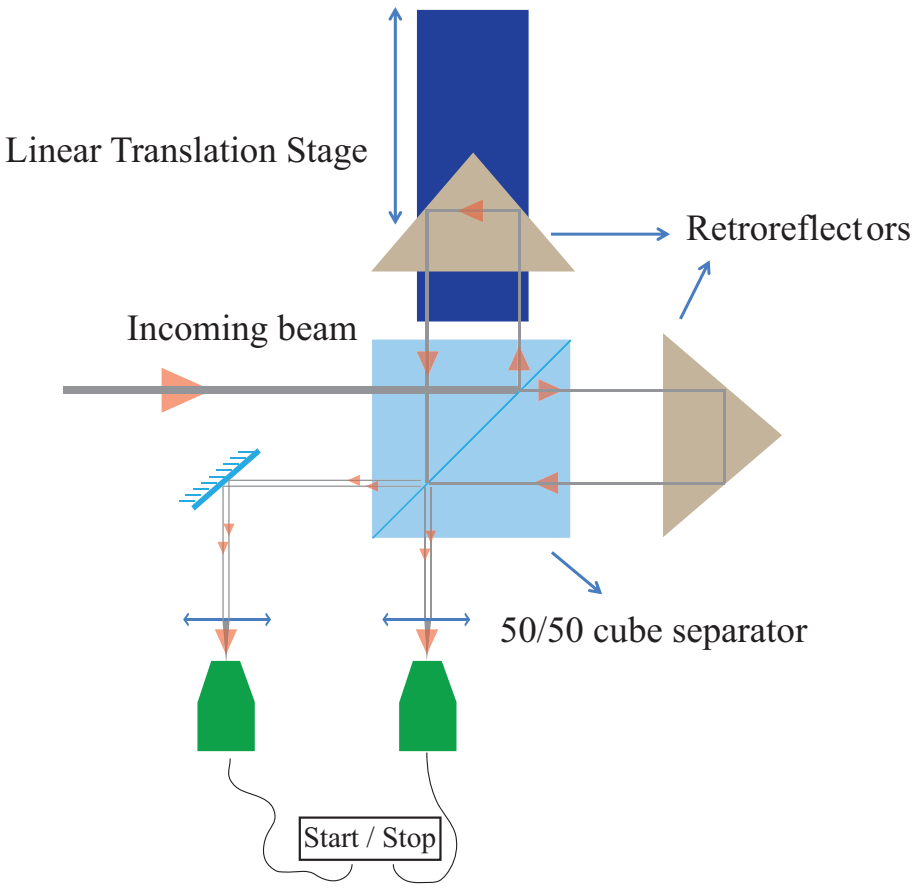

Figure 1.11: Schematic presentation of the time resolved detection system

(which is nearly reached on fig. 1.9), meaning that two photons will never be detected exactly at the same time (with $\tau = 0$). This is a purely quantum property as a classical light beam would be characterized by $g^2(0) \geq 1$.

1.2.3 Fourier analysis and emission pattern

We describe here the measurement of the angular dependence of light emission (emission pattern). For macroscopic studies, the goniometer is a convenient tool for analysis of the emission pattern. For microscopy studies, rotating a microscope objective around the microscopic emitting point is usually unpractical and provides low angular and spatial resolution. In order to study the emission pattern in a microscopy configuration, it is more appropriate to collect all emission angles with the objective and then make an image of the Fourier plane, where the field is the Fourier transform (k-space distribution) of the field in the object plane.

Distribution in k-space and emission pattern

Let us now give a short formal description of the problem, following [18]. In order to describe the radiation pattern from an emitting structure located in plane $z = 0$, one needs to know the field in plane $z = 0$. The electric field in the plane $z = 0$ can be written as a function of its Fourier transform $\hat{\vec{E}}$: by definition

$$\vec{E}(x, y; z = 0) = \iint_{-\infty}^{+\infty} \hat{\vec{E}}(k_x, k_y; z = 0) e^{i[k_x x + k_y y]} dk_x dk_y \tag{1.21}$$

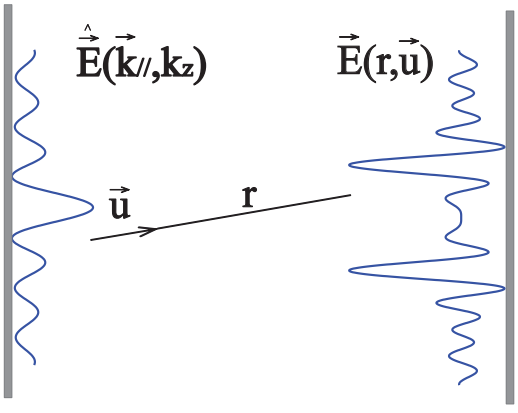

Figure 1.12: Emission from the object plane $z = 0$.

The emission pattern is given by the field radiated along a direction of unit vector $\vec{u}$, at a distance $r \gg \lambda$ (far-field emission). We define the wave vector $\vec{k} = k\vec{u} = \frac{2\pi}{\lambda}\vec{u}$ and call $\vec{k_\parallel}$ its (x,y) component and k_z its z-component. The radiated far-field can be written as demonstrated in [18] :

$$\vec{E}(\vec{r} = r\vec{u}) = -2\pi i k_z \hat{\vec{E}}(\vec{k_\parallel})\frac{e^{ikr}}{r} \tag{1.22}$$

The $\frac{e^{ikr}}{r}$ depdendence is characteristic of a spherical wave, while the emission angular distribution is mainly carried by the $\hat{E}(\vec{k_\parallel})$ term. This equation shows us that, the radiation pattern in far field along the direction of $\vec{k}$ is entirely defined by the Fourier spectrum $\hat{\vec{E}}(\vec{k_\parallel})$ of the field distribution at $z = 0$.

Measuring the Fourier transform of the electric-field in the plane $z = 0$ is thus equivalent to measuring the system radiation pattern (proportionnal to $||\vec{E}(r\vec{u})||^2$). In other words, the radiation pattern provides the Fourier distribution of the electric field in the plane $z = 0$ (for $\| \vec{k_\parallel} \| \leq \frac{2\pi}{\lambda}$ components only, as the other k components are evanescent and not radiated to far-field).

Imaging by an objective

The objective lens is the most important optical unit of an optical microscope and determines its basic performance/function. Recent microscopes use so-called "infinity-corrected objectives", which means that the image is formed at infinity after the objective. One then needs a tube lens to form an image (fig. 1.13).

The objective and microscope system are characterized by the following parameters :

- f, the focal length of the equivalent objective thin lens;
- F the focal length of the tube lens;
- $N.A.$ the numerical aperture of the objective, given by :

$$N.A = n_1 * sin(\theta_{max}) \tag{1.23}$$

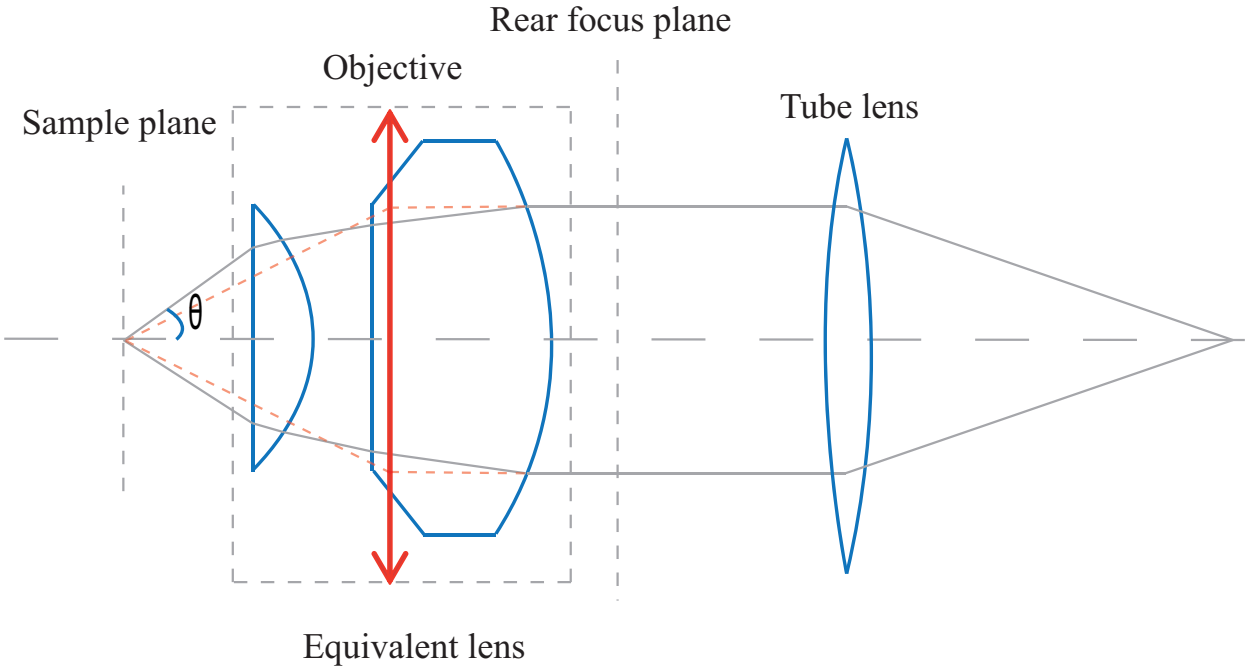

Figure 1.13: Schematic presentation of the microscope optics : the objective is an assembly of several lenses, behaving as an equivalent lens (red arrow). The sample must be positioned at the object focal plane of this lens. The Fourier plane of the objective is located at its rear focal plane. Light from the sample is collimated by the objective and must be re-focused by a second lens (tube lens).

with n_1 the refractive index of the incidence medium (1 for air objective, 1.45 for objective with oil immersion), and θ_{max} the maximal collection angle (which depends on the objective focal length and lateral dimension).

- The microscope magnification is then given by:

$$M = \frac{F}{f} \tag{1.24}$$

The Fourier transform of the electric field at sample level is made by the objective directly and it is located at the rear focus plane of the objective. The size of the light beam in the Fourier plane is given by :

$$D = 2 * f * N.A \tag{1.25}$$

Our set-up will then be designed to detect emission in a plane conjugated to the objective rear focus plane. We will discuss more in detail in the following section with ABCD matrix method.

Analysis of the Fourier plane and apodisation term

We now present how to analyse the Fourier plane image, assuming that a camera is located in the Fourier plane of the sample.

Generally, if we want to study an optical system within the geometric optics approximation, we need to apply the paraxial condition for all beams : all beams have small angles $\theta = \sin(\theta) = \tan(\theta)$ with respect to the optical axis. However the microscope objective is designed to collect emission from angles which are not always small ; for instance a numerical aperture of 0.7 (for air objective) corresponds to a collection angle of 45°. However for propagation after the objective, the angles will be sufficiently small due to the angular magnification introduced by system, so that we can apply geometric optics laws for the rest of the optical set-up (tube lens and other lenses).

As shown in Figure 1.14(a), the objective is designed, in order to reduce aberration, to fulfill Abbe's sine condition [19] :

$$h = f \sin(\theta) \tag{1.26}$$

between the emission angle θ and the distance h of the light beam to the optical axis after passing through the objective. Note that geometric optics considerations in the paraxial condition would lead to $h = f\tan(\theta)$.

The detected image can be expressed as :

$$I_{camera} = \frac{dP_{camera}}{dS} \tag{1.27}$$

of which dS is the surface of one pixel and dP_{camera} is the power that one pixel receives. On the other hand, the emission pattern is defined as :

$$R(\theta, \phi) = \frac{dP}{d\Omega} \tag{1.28}$$

where dP is the power emitted into the solid angle element $d\Omega$.

$R(\theta, \phi)$ can be obtained from the measured data I_{camera}, as represented on figure 1.14(b) : the light power passing by surface dA_1 should be equal to the power passing by surface dA_2 (energy conservation) : $dP_{camera} = dP$. Since $dS = dA_2 = \cos\theta dA_1 = f^2 \cos\theta d\Omega$, we find :

$$I_{camera} = \frac{R}{f^2 \cos\theta} \tag{1.29}$$

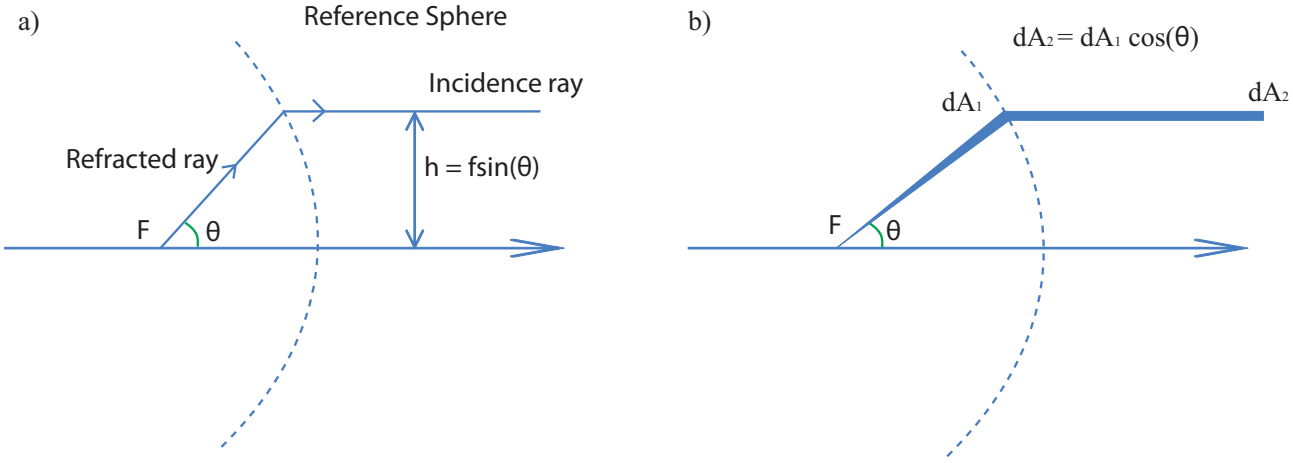

Figure 1.14: a) The sine condition of geometrical optics. b) The apodization factor due to energy conservation.

In conclusion, the emission pattern $R(\theta, \phi)$ can be obtained from the image in the Fourier plane ($I_{camera}(h, \phi)$ in polar coordinates) by :

1. Changing the coordinates from h to θ by $h = f \sin\theta$;
2. Applying the apodisation therm $R = I_{cam} \times f^2 cos(\theta)$.

ABCD matrix formalism

As described above, the objective will give us the Fourier plane of the sample at the rear focal plane of the objective. In order to measure the Fourier plane image, the Fourier plane should be conjugated to a detection system (a CCD camera for example). In order to find the appropriate configuration, we use ABCD matrices calculations.

The ABCD matrix formalism describes light propagation between an input and an output plane. A beam enters the system by crossing an input plane 1 at position x_1 with an angle θ_1. After the optical system, the beam will cross an output plane 2 at position x_2 with an angle θ_2 as shown in figure 1.15.

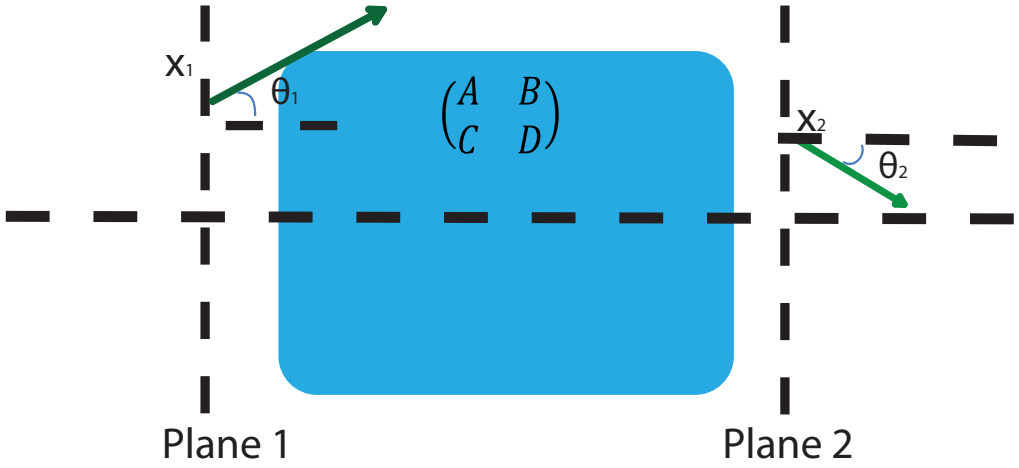

Figure 1.15: Principle of the ABCD matrix formalism

Within the paraxial approximation, the linear relation between x_1, θ_1, x_2, θ_2 can be expressed by an "ABCD" matrix as follows:

$$\begin{pmatrix} x_2 \\ \theta_2 \end{pmatrix} = \begin{pmatrix} A & B \\ C & D \end{pmatrix} * \begin{pmatrix} x_1 \\ \theta_1 \end{pmatrix} \tag{1.30}$$

The ABCD matrices for certain optical elements are as follows:

For a thin lens with a focal length f :

$$\begin{pmatrix} 1 & 0 \\ -\frac{1}{f} & 1 \end{pmatrix} \tag{1.31}$$

For propagation in free space over a distance L :

$$\begin{pmatrix} 1 & L \\ 0 & 1 \end{pmatrix} \tag{1.32}$$

The case B = 0 corresponds to :

$$\begin{cases} x_2 = Ax_1 \\ \theta_2 = Cx_1 + D\theta_1 \end{cases} \tag{1.33}$$

so that a beam which crosses plane 1 at position x_1 will cross the output plane 2 at a given position $x_2 = Ax_1$, whatever the incidence angle θ_1. This means that plane 1 and plane 2 are conjugated planes in this situation, with A the magnification of the optical system.

For the case B $\neq$ 0, if we know the electric field distribution at plane 1 $\vec{E_1}(\vec{r_1})$ and the ABCD matrix between plane 1 to plane 2, the electric field distribution at plane 2 $\vec{E_2}(\vec{r_2})$ can be written as [20] :

$$\vec{E_2}(\vec{r_2}) = -e^{ik(z_2-z_1)}\frac{i}{B\lambda}\iint d^2\vec{r_1}\vec{E_1}(\vec{r_1})\, exp\left[-i\frac{\pi}{B\lambda}\left(A\vec{r_1}^2 - 2\vec{r_1}\vec{r_2} + D\vec{r_2}^2\right)\right] \tag{1.34}$$

with z_1 and z_2 the z-coordinates of plane 1 and plane 2 respectively, and $\vec{r_1}$, $\vec{r_2}$ vectors parallel to the planes 1 and 2 as shown in figure 1.16.

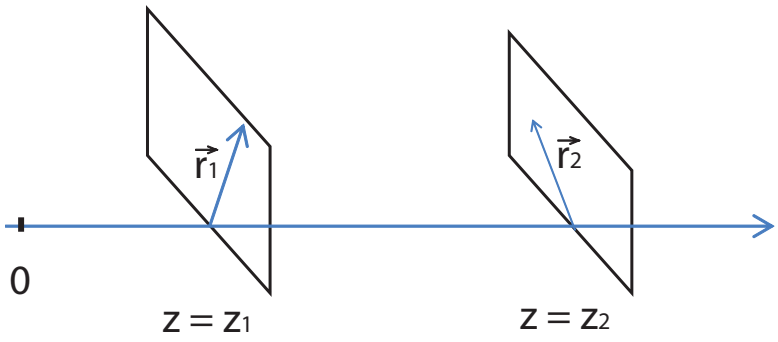

Figure 1.16: Definition of z_1, z_2, $\vec{r_1}$, $\vec{r_2}$ in ABCD matrix calculation

Equation 1.34 shows that, for an optical system for which the ABCD matrix gives $A = D = 0$, the field distribution at plane 2 will be:

$$\vec{E_2}(\vec{r_2}) = -e^{ik(z_2-z_1)}\frac{i}{B\lambda}\iint d^2\vec{r_1}\vec{E_1}(\vec{r_1})\,exp\left[i\frac{\pi}{B\lambda}(2\vec{r_1}\vec{r_2})\right] = -e^{ik(z_2-z_1)}\frac{i}{B\lambda}\hat{\vec{E}}_1(\frac{2\pi}{B\lambda}\vec{r_2}) \quad (1.35)$$

which is a Fourier transform of the field distribution at plane 1 with $\vec{k} = \frac{2\pi}{B\lambda}\vec{r_2}$. If $A = 0$ but $B, C, D \neq 0$, this system will give a Fourier transform with a supplementary phase term (which will make no difference as the camera will only measure $||\vec{E_2}||^2$) :

$$\vec{E_2}(\vec{r_2}) = -e^{ik(z_2-z_1)}\frac{i}{B\lambda}\iint d^2\vec{r_1}\vec{E_1}(\vec{r_1})\,exp\left[-i\frac{\pi}{B\lambda}\left(-2\vec{r_1}\vec{r_2} + D\vec{r_2}^2\right)\right] = -e^{ik(z_2-z_1)}\frac{i}{B\lambda}\hat{\vec{E}}_1 e^{-\frac{i\pi D}{B\lambda}{r_2}^2} \quad (1.36)$$

As an example, let us consider the case of a thin lens in $f - f$ configuration as shown in figure 1.17.

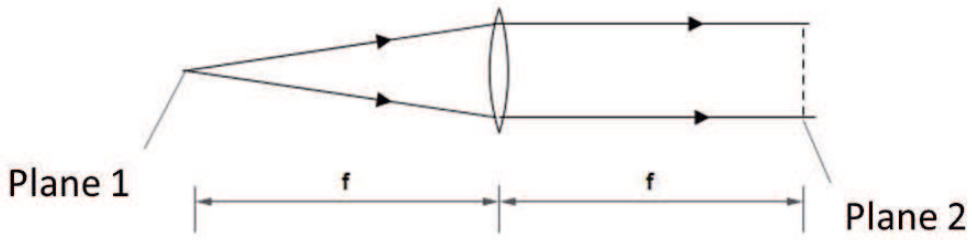

Figure 1.17: A thin lens in $f - f$ configuration.

The ABCD matrix from plane 1 to plane 2 is then :

$$\begin{pmatrix} 0 & f \\ -\frac{1}{f} & 0 \end{pmatrix} \quad (1.37)$$

We are thus in condition $A = D = 0$: in $f - f$ configuration, the plane 2 is a Fourier image of plane 1, with

$$\vec{k}_{\parallel} = \frac{2\pi}{f\lambda}\vec{r_2} \quad (1.38)$$

Note however that, in our setup, the Fourier transform is performed by the objective as described in the previous section, but the paraxial approximation is not valid.

ABCD matrix for measurement system

The optical schematic of our measurement system is presented in figure 1.18 :

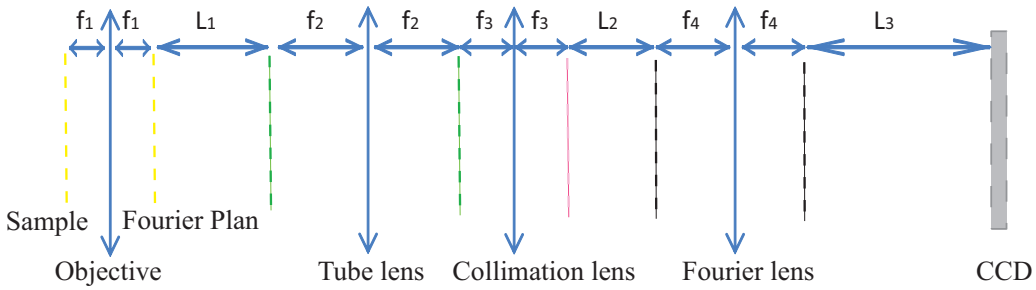

Figure 1.18: Optical schematic of the Fourier-plane setup.

As the tube lens and the collimation lens have been chosen previously and should not be moved to avoid perturbation on other detection systems, the aim is to add another lens (which we call Fourier lens on figure 1.18) to make the conjugation as mentioned above.

The objective cannot be described within the ABCD formalism as it is not a paraxial approximation, but the rest of the setup can. The ABCD matrix describing the portion of the setup from the rear focal plane of the objective until the CCD is :

$$\begin{pmatrix} A & B \\ C & D \end{pmatrix} = \begin{pmatrix} -\dfrac{f_3 L_3}{f_2 f_4} & \dfrac{\left(f_2^2 L_2 + f_3^2 L_1\right) L_3 - f_2^2 f_4^2}{f_2 f_3 f_4} \\ \dfrac{f_3}{f_2 f_4} & \dfrac{2^2 L_2 + f_3^2 L_1}{f_2 f_3 f_4} \end{pmatrix} \tag{1.39}$$

For our system, $f_1 = 3\,\text{mm}$, $f_2 = 180\,\text{mm}$, $f_3 = 100\,\text{mm}$, $L_1 = 50\,\text{mm}$; we choose for the Fourier lens $f_4 = 150\,\text{mm}$; the distance between the collimation lens and the CCD is fixed at around 1000 mm because of the space available on the table. We know that, from the objective Fourier plane to the CCD, the B element in the ABCD matrix should equal to zero, and in this case, the A term will give us the magnification of the system. We have then :

$$\begin{cases} (f_2^2 L_2 + f_3^2 L_1) L_3 - f_2^2 f_4^2 = 0 \\ \\ f_3 + L_2 + 2f_4 + L_3 = 750mm \end{cases} \tag{1.40}$$

From these two equations, we find that we should use the values $L_2 = 63mm, L_3 = 287mm$. The Fourier plane on the CCD is then an image of the objective rear focal plane, with a magnification $A = 1.06$.

Angular resolution of the Fourier plane measurement

The size of the Fourier image on the detection system will determine the angular resolution of the measurement : if it is too small, the angular resolution will be poor ; if it is too large, the emission will be dispersed over too many pixels and the signal-to-noise ratio will be low (and eventually the image will be larger than the detector).

We now take an example of an air objective with an equivalent focal length $f = 3\,\text{mm}$ and a numerical aperture of 0.7, with detection by an EMCCD camera with 512*512 pixels of size $p = 16\,\mu\text{m}$. The diameter of the sample Fourier image is 4.2 mm, as given by equation 1.28. The image diameter on the detection system (with $M = 1.06$ magnification of the Fourier plane) will than have a diameter of 4.45 mm, while the EMCCD size is 8.2 mm.

The angular resolution is then obtained from figure 1.14, by relating the pixel size p to the angular resolution :

$$p = Mdh = Mf \cos\theta d\theta \tag{1.41}$$

so that, since angles θ from 0 to 44° are collected, the angular resolution ranges between 0.3 and 0.4° and is well sufficient for our experiments.

Two detection possibilities based on Fourier plan measurements

The Fourier lens position is set following the calculations above, and adjusted with the help of a He-Ne laser : we send the collimated laser into the objective from the sample side, so that the laser will be focused on the Fourier plane. We adjust the position of the Fourier lens to make the laser spot on the detector as small as possible.

We installed two different possibilities to measure the Fourier plane.

In a **first configuration** we image the Fourier plane with an EMCCD camera. In this way we have a direct image of the entire Fourier plane, with θ and ϕ resolutions. Figure 1.19 shows the Fourier plane image of the emission from a point-like emitter (a silica bead (around 200 nm) containing fluorescent molecules commercialized by ThermoFisher) deposited on a glass surface. The sample is imaged with an oil immersion objective with a numerical aperture of 1.4 and equivalent focal length of 1.8 mm.

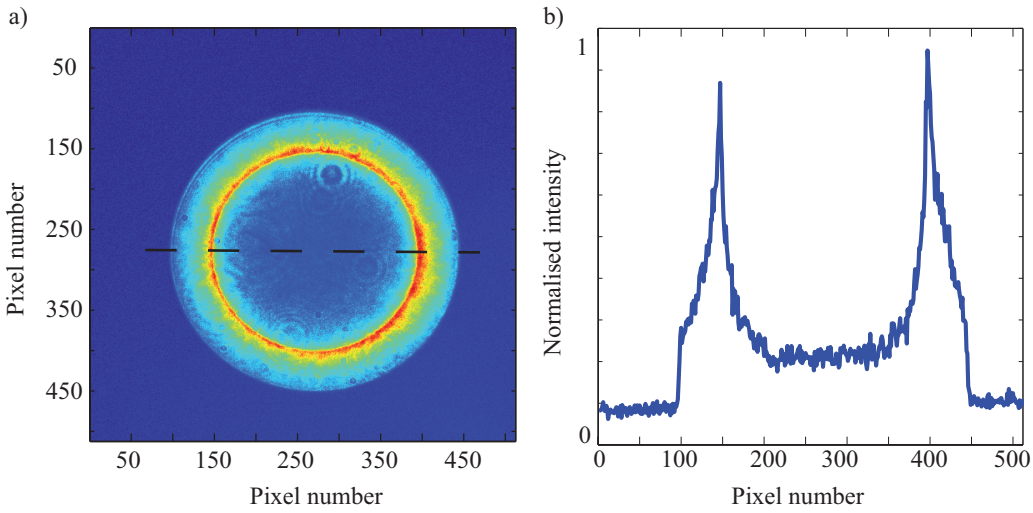

Figure 1.19: a) Image of the Fourier plane on an EMCCD camera of from a point-like emitter (a silica bead (around 200 nm) containing fluorescent molecules commercialized by ThermoFisher) deposited on glass surface and detected with an objective with oil immersion b) Profile of the Fourier image along the black dashed line.

The Fourier plane image covers around 348 pixels = 5.6 mm, corresponding to 5.3 mm on the objective rear focal plane. We expect a diameter of the Fourier plane image of $2f \times NA$ = 5 mm, in agreement with the measurement. For the analysis of the Fourier image, we will always plot its profile (fig. 1.19(b)) and associate the limits of the Fourier plane (pixels 100 and 440 here) to the angles $-\theta_{max}$ and $+\theta_{max}$, which calibrates the linear correspondence between pixels and $\sin\theta$.

The two peaks on figure 1.19(b) correspond to the coupling between evanescent wave in the low index material (air) with propagative wave in the high index material (glass substrate) which appears at the critical angle $asin(n_{air}/n_{silica})$. From the experimental Fourier plane, with the calibration explained above, the critical angle is 42°, which is exactly equal to the

theoretical value, validating the measurement setup and its alignment.

In the **second configuration** we superpose the center of the Fourier plane with the entrance slit of a spectrometer as shown in the Figure 1.20. As the spectrometer we use is an imaging spectrometer, the image on the entrance slit is conjugated to the CCD sensor with a magnification of 1. The Y axis on the CCD sensor gives us the information of emission angle. And as the photons will be dispersed by the optical grating inside the spectrometer along the X direction, the X axis on the CCD sensor can then give us information about the emission wavelength. To conclude, on the CCD sensor of the spectrometer, we can have information of the emission angle, or k-vector (Y axis) and on the emission wavelengh (X axis) at the same time : this yields the dispersion relation of the emission. Note that the width of the entrance slit should be much smaller than the diameter of the Fourier plane pattern in order to choose only one azimuthal direction ϕ. We chose a slit width of 0.1 mm which is much smaller than the Fourier pattern diameter 4.2 mm.

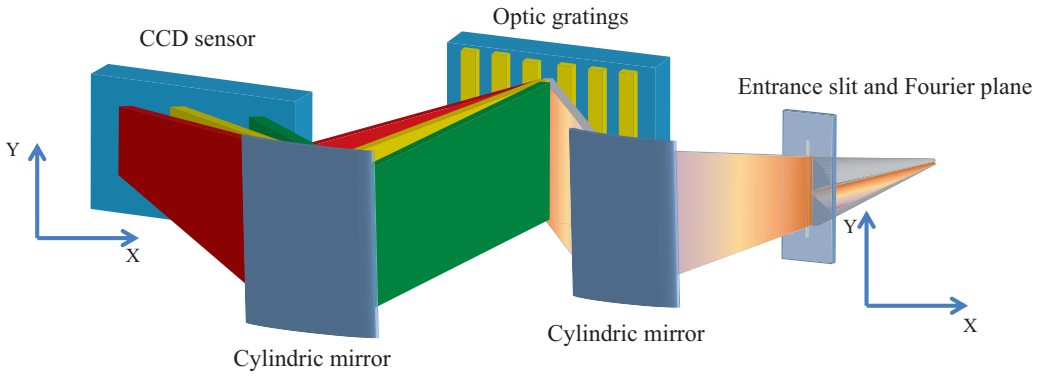

Figure 1.20: Setup for spectrally-resolved Fourier plane measurement.

Figure 1.21 shows some spectrally-resolved Fourier plane images (dispersion relations) measured with an air objective with a numerical aperture of 0.7.

Figure 1.21 (a) corresponds to the emission from a layer of silica beads containing fluorophores. It shows that the emission spectrum of these emitters is centered around 618 nm. On axis Y, the number of illuminated pixels corresponds to the diameter of the Fourier plane at the entrance slit of the spectrometer. We can see the clear cut in emission for pixel numbers below 99 and above 448, corresponding to the numerical aperture of the objective. The emission is broadly distributed into all directions.

Figure 1.21 (b) shows the same spectrally-resolved Fourier imaging for nanocrystal emitters

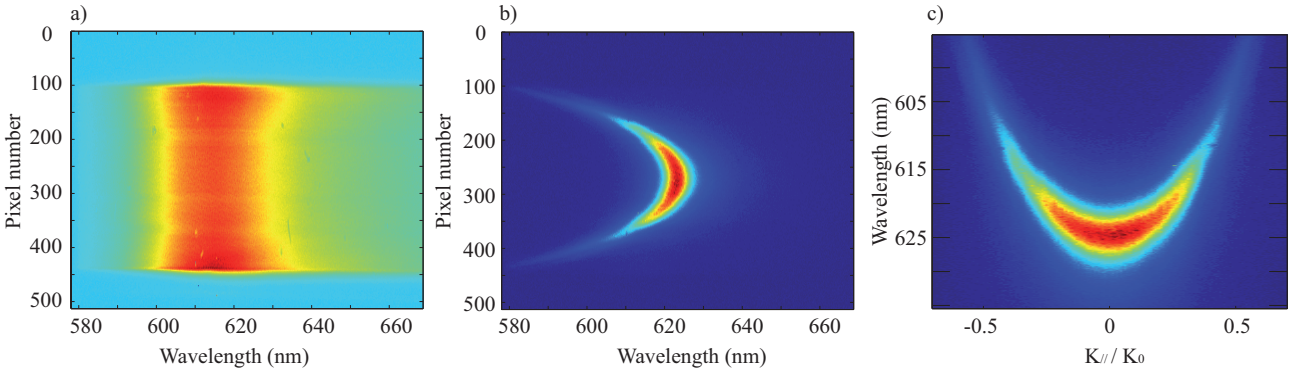

Figure 1.21: a) Spectrally-resolved Fourier image (CCD image) of a layer of emitters on a glass surface. b) Spectrally-resolved Fourier image (CCD image) of a layer of nanocrystals in a 2D-Tamm sample. c) The dispersion relation of the 2D-Tamm structure, extracted from (b).

inside a 2D Tamm structure (as will be introduced in the last chapter of this thesis). The 2D-Tamm mode corresponds to wavelength 625 nm for $\theta = 0$, and the emission angle increases when the emission wavelength decreases. By calibrating the pixel-angle correspondence with the use of figure 1.21(a) (pixels 99 and 448 are associated respectively to $\sin\theta = -0.7$ and 0.7), we can extract from fig. 1.21(b) the dispersion relation of the 2D-Tamm sample emission. The curve shows that the 2D-Tamm structure has a parabolic dispersion relation, which will be discussed in detail in the last chapter on Tamm structures.

1.3 Conclusion

In this chapiter, we have made a brief recall of theoretical modeling of semiconductor colloidal nanocrystal energy structure. It is shown that, the nanocrystal absorption and emission spectrum blue shift when the size of nanocrystal descrease due to quantum confinements. The nanocrystal emission dynamics (exciton lifetime) depends on both radiative and non-radiative characteristic times.

The optical properties (emission dynamics, single photon emission, emission spectrum) from colloidal semiconductor nanocrystals have been demonstrated experimentally. It is shown that the emission from a single nanocrystal shows antibunching which proves that a single nanocrystal is a single photon emitter. The emission intensity from a nanocrystal is stable under the excitation of laser, no clear dark state is shown.

It has also been explained how a new home made fluorescence microscope with divers detection possibilities was installed for experiment measurements. The emission coherence can be studied with the Michelson interferometer. The emission pattern can be measured with an EMCCD coupled with the Fourier plane of the sample. Also, the emission spectrum is measurable with the spectrometer. The Fourier plane of the sample is also coupled to the entrance slit of the spectrometer which raises the possibility to measure the emission dispersion relation.

In the following chapters, we will use this fluorescence microscope to characterize 3D confined optical Tamm modes.

Bibliography

[1] L. E. Brus. Electron-electron and electron-hole interactions in small semiconductor crystallites: The size dependence of the lowest excited electronic state. *The Journal of chemcal physics*, 80(9):4403–4409, 1984.

[2] Z. Alfassi, D. Bahnemann, and A. Heinglein. Photochemistry of colloidal metal sulfides. 3. photoelectron emission from CdS and CdS-ZnS co-colloids. *Journal of chemcal physics*, 86(24):4656–4657, 1982.

[3] C. B. Murray, D. J. Norris, and M. G. Bawendi. Synthesis and characterization of nearly monodisperse CdE (E = sulfur, selenium, tellurium) semiconductor nanocrystallites. *Journal of American Chemical Society*, 115(19):8706–8715, 1993.

[4] A. Smith and S Nie. Semiconductor nanocrystals: structure, properties, and band gap engineering. *Accounts of chemical research*, 43(2):190–200, 2010.

[5] N. W. Ashcroft and N. D. Mermin. Physique des solides. *Saunders College Publishing*, 2002.

[6] A. L. Efros. Luminescence polarisation of CdSe microcrystals. *Physical Review B*, 46(12):7448–7458, 1992.

[7] D. J. Norris and M. G. Bawendi. Measurement and assignment of the size-dependent optical spectrum in CdSe quantum dots. *Physical Review B*, 53(24):338–346, 1996.

[8] Cassette Elsa. Nanocristaux de semi-conducteurs II-VI et I-III-VI :controle des proprietes optiques de structures. *PhD thesis*, page 36, 2012.

[9] A. Ekimov, F. Hache, and M. Schanne-Klein. Absorption and intensity dependent photoluminescence measurement on CdSe quantum dots: assignment of the first electronic transitions. *Journal of Optical Socitety of America*, 10(1):100–107, 1993.

[10] Efros. A. L. and Rosen. M. The electronic structure of semiconductor nanocrystal 1. *Annual review of materials science*, 30(5):475–521, 2000.

[11] Klimov. V. I. Nanocrystal quantum dots. *Boca Raton 2nd ed*, 2010.

[12] Anikeeva. P. O., Halpert. J. E., Bawendi. M.G, and Bulovic. V. Quantum dot light-emitting devices with electroluminescence tunable over the entire visile spectrum. *Nanolett*, (9):2532–2536, 2013.

[13] Sergio Brovelli, Wan Ki Bae, Christophe Galland, Umberto Giovanella, Francesco Meinardi, and Victor I. Klimov. Dual-color electroluminescence from dot-in-bulk nanocrystals. *Nanolett*, 14(2):486–494, 2014.

[14] Dekanozishvili. G., Driaev. D., Kalabegishvili. T., and Kvatchadze. V. Thermoluminescence and absorpion spectra of CdSe quantum dot-doped glass irradiated by X-rays. *J. Lumin*, 129(129):1154–1157, 2009.

[15] J. Rodriguez-Viejo, K. F. Jensen, H. Mattoussi, J. Michel, B. O. Dabbousi, and M. G. Bawendi. Cathodoluminescence and photoluminescence of highly luminescent CdSe/ZnS quantum dot composites. *Appl. Phys. Lett*, 70(16):2132–2134, 1997.

[16] Zackaria Mahfoud, Arjen T. Dijksman, Javaux Clmentine, Bassoul Pierre, Baudrion Anne-Laure, Plain Jerome, Dubertret Benoit, and Kociak Mathieu. Cathodoluminescence in a scanning transmission elctron microscope: a nanometer-scale counterpart of photoluminescence for the study of II-VI quantum dots. *J. Phys. Chem. Lett*, 4(23):4090–4094, 2013.

[17] BELACEL Cherif. Emission de nanocristaux semi-conducteurs dans une antenne patch plasmonique. *PhD thesis*, 2013.

[18] L. Novotny and B. Hecht. Principles of nano-optics. *Cambridge University Press*, 2006.

[19] Joseph J. M. Braat. Abbe sine condition and related imaging conditions in geometrical optics. *Proc. SPIE*, 3190:59–64, 1997.

[20] M. Nisoli S.Stagira G.Cerullo, S.Longhi and O. Svelto. Problems in laser physics. *Kluwer Academic / Plenum Publishers*, 2001.

Chapter 2

Spatially-resolved analysis of 0D-Tamm structures radiation pattern

Introduction

Manipulating light emission and propagation inside nanophotonics structures requires a fine understanding of the characteristics of their electromagnetic modes, such as their spectral properties, their spatial distribution, or the far-field angular radiation pattern, which is related to the electric-field k-vector distribution. However, combining these measurements can raise difficulties, for instance the photonic modes spatial distribution and k-vector distribution are Fourier-conjugated quantities and cannot be probed simultaneously with unlimited precision.

In this chapter, we present a study on the emission properties of colloidal nanocrystals coupled with optical Tamm structures. The optical Tamm mode is an electromagnetic mode confined between a Bragg mirror and a metallic layer. Lateral confinement of the mode can be obtained by changing the metallic layer to a metallic disk. It has been shown recently that this structure has potential in various applications such as single photon sources or solid state lasers.

The first section will present theoretical description and state of the art on optical Tamm states.

The second section will explain the choice of the Tamm structure parameters, based on transfer-matrix simulations of these structures.

The third section describes the sample fabrication procedure.

In section 4, we show how the experimental nanocrystals luminescence demonstrates their coupling with Tamm structures.

In section 5, we present spectroscopic analysis of the electromagnetic modes of the optical Tamm mode, with both spatial and k-vector resolutions. The agreement between measurement and simulation shows that the spatial and k-vector precisions are limited only, as expected, by diffraction. This experiment provides a probe of the phase distribution of the cavity modes complex electric field (while standard imaging provides only the electric field norm).

In section 6, we excite nanocrystals at various positions inside the Tamm structure and show how the emitter's position can tune the emission direction.

2.1 Optical Tamm states

2.1.1 Theoretical modeling of optical Tamm modes

Tamm states were first proposed by Igor Tamm in 1932 as electronic states confined at the surface of crystalline solids. Kaliteevski et al. proposed in 2007 an optical analogue where the cristalline electron potential is replaced by a periodic optical structure [1]. He showed that an electromagnetic mode could be confined at the interface between a Bragg mirror and a metallic layer (Figure 2.1 (b)) and called this mode "Tamm plasmon". Since then, different kinds of Tamm modes have been discussed. For example, D. Ritwick et al. discussed theoretically a mode at the interface between two Bragg mirror (Figure 2.1 (a)) [2]. He called this mode "optical Tamm mode" in order to distinguish it from the former metallic-Bragg mirror structures. Although these two denominations are commonly used and distinguished in the literature [3], we choose in this manuscript to refer to our metal-Bragg structures only by the term "optical Tamm state" ; we avoid the term "plasmon" in order to avoid any confusion with the more common surface-plasmon states located at a metal-dielectric interface.

For the Tamm mode confined between a Bragg mirror and a metallic layer, the vertical confinement is obtained on one side from the stop-band of the Bragg mirror and the other side by the negative dielectric index of the metal as shown in Figure 2.2. The electromagnetic waves are confined at the interface between the Bragg mirror and the metallic layer.

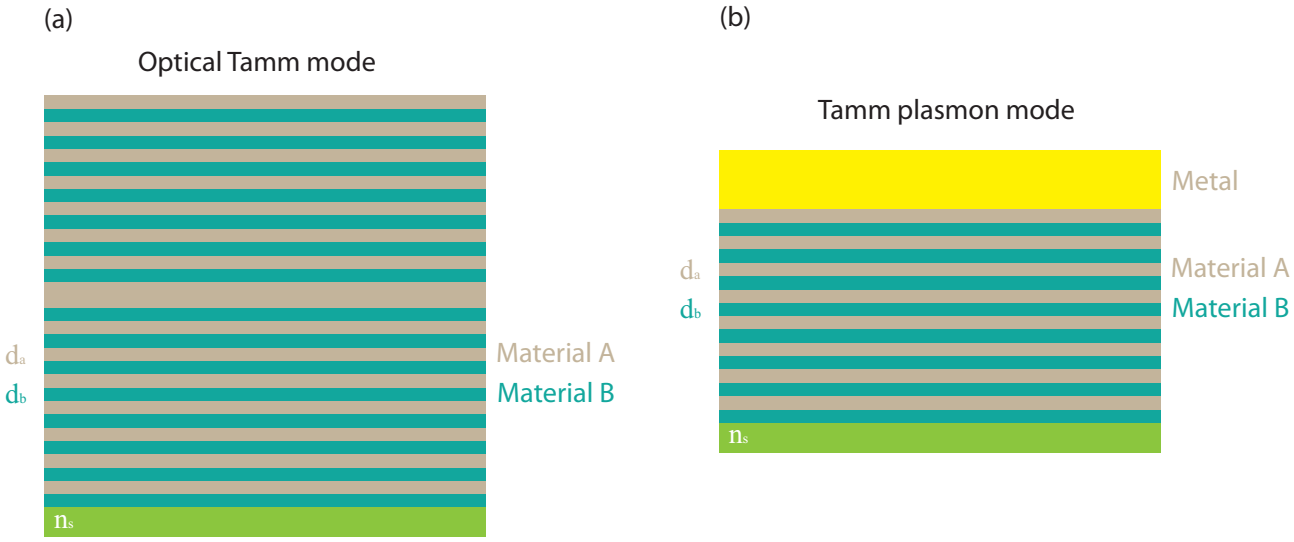

Figure 2.1: Schematics of 2 different Tamm modes : (a) Optical Tamm mode, the electromagnetic wave is confined between the two Bragg mirrors, (b) Tamm plasmon mode, the electromagnetic wave is confined between a Bragg mirror and a layer of metal.

In order to describe theoretically this situation, we first introduce briefly in the following parts the reflectivities of these surfaces.

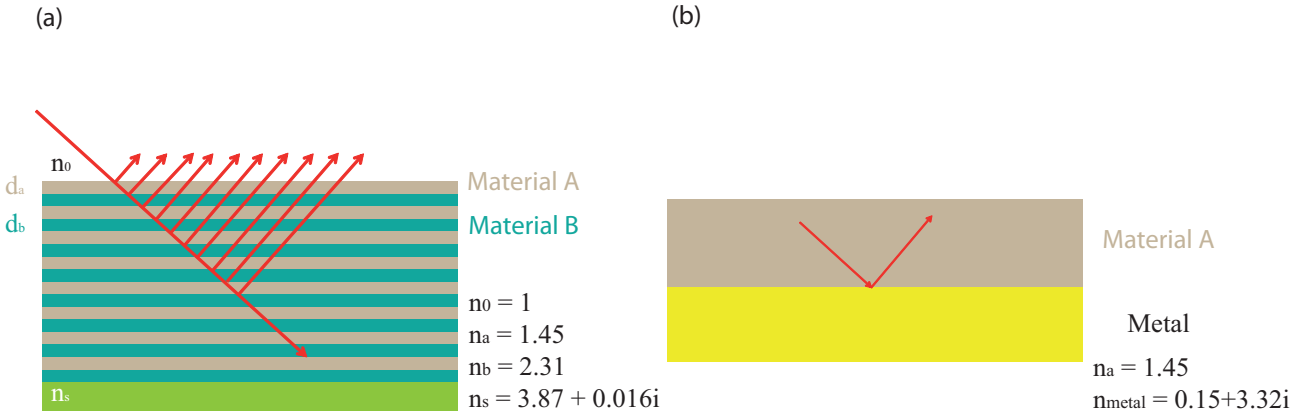

Figure 2.2: Schematics of 2 reflection configurations : (a) on a Bragg mirror, (b) on a metallic surface.

Reflection by a Bragg mirror

A Bragg mirror (also called distributed Bragg reflector) is a 1D photonic crystal formed from multiple periodic layers (as shown in Figure 2.1) of two different dielectric materials with different refractive indices n_a and n_b and thicknesses d_a and d_b with $n_a d_a = n_b d_b$. Each interface

causes a partial reflection of the incident optical wave. When the wavelength is sufficiently close to the Bragg resonance condition $\lambda/4 = n_a d_a = n_b d_b$, these reflections interfere constructively and the layers act as a high-quality reflector. The range of wavelengths that are reflected is called the photonic stop band. Within this range of wavelengths, light is "forbidden" to propagate in the structure. The reflectivity of a Bragg mirror at the resonant frequency (labelled ω_0) and at normal incidence can be expressed as [4] :

$$R_{BM} = \left[\frac{n_0(n_b)^{2N} - n_s(n_a)^{2N}}{n_0(n_b)^{2N} + n_s(n_a)^{2N}}\right]^2 \tag{2.1}$$

where n_0 is the reflective index of the incidence medium, n_s the substrate index and N the number of (a, b) layers pairs of the Bragg mirror. Equation 2.1 shows that the reflectivity of a Bragg mirror increases with the number of layers and with the index contrast $(n_a - n_b)$.

The width of the stop band of a Bragg mirror (full width at half maximum of the intensity reflectivity) is given in the limit of high N by :

$$\frac{\Delta\omega_0}{\omega_0} = \frac{4}{\pi} arcsin\left(\frac{|n_a - n_b|}{n_a + n_b}\right) \tag{2.2}$$

Equation 2.2 shows that the stop-band of a Bragg mirror will be broader if the index contrast is higher.

Reflection on a metal surface

Unlike dielectric media, metals present a complex optical index and negative dielectric constant. The imaginary part of the optical index describes the absorption of light when it propagates inside the metal. Generally, the real part of the metal opticalal index is much smaller than unity, and the optical index contrast gives the strong reflection on metal surface.

The reflection coefficient at a dielectric-metal interface at normal incidence can be expressed by Fresnel's equations :

$$r_M = \frac{n_a - n_{metal}}{n_a + n_{metal}} \tag{2.3}$$

with n_a the optical index of the material in contact with the metal (in our case it will be SiO_2) and n_{metal} the index of the metal. With Drude's model [5], the optical index of a metal

can be expressed as :

$$n_{metal}^2 = \varepsilon_r(1 - \frac{\omega_p^2}{\omega(\omega + i\gamma)}) \tag{2.4}$$

with γ the collision rate of the metal of study, ω_p its plasma angular frequency and ε_r its relative permittivity. We will choose for our structures silver, which is widely used for nanophotonics structures in the visible range because it presents relatively few losses. The plasma frequency of silver is expressed by the following equation :

$$\omega_p = \sqrt{\frac{n_e e^2}{m^* \varepsilon_0}} \tag{2.5}$$

with n_e the density of electrons in the metal, e the electron charge, m^* the effective mass of the electron, and ε_0 the permittivity of free space. By applying the numerical values $n_e = 10^{28}/m^3$, $e = 1.6 * 10^{-19}C$, $m^* = 0.99m_e$ and $\varepsilon_0 = -14.037 + i * 1.043$ into equation 2.5, we find that the wavelength corresponding to the plasma frequency of silver is around 120 nm (9.6 eV). As the studied wavelength is around 600 nm (2 eV), we can use the approximation $\omega \ll \omega_p$ for equation 2.4. Equation 2.4 can then be expressed as:

$$r_M \approx -1 - \frac{2in_a\omega}{\sqrt{\varepsilon_r}\omega_p} \approx -exp(\frac{2in_a\omega}{\sqrt{\varepsilon_r}\omega_p}) = exp[i(\pi + \frac{2n_a\omega}{\sqrt{\varepsilon_r}\omega_p})] \tag{2.6}$$

Equation 2.6 shows that when the angular frequency of the photon is much smaller then the plasma frequency of the metal, incidence light is reflected on a silver surface with an amplitude close to unity (nearly total reflection) and a phase around π.

Vertical confinement of optical Tamm mode introduced by Bragg mirror and metallic layer

We now describe the electromagnetic field confinement inside a Tamm structure with a Bragg mirror and a metallic layer. Following the framework of Kaliteevski et al. [1], the structure can be described as a two mirror system as shown in figure 2.3.

Assuming that these structures present weak losses, their resonance condition at normal incidence can be given by :

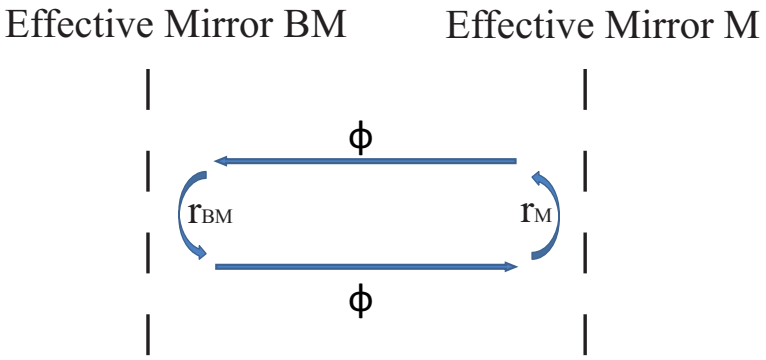

Figure 2.3: Effective mirror description for the optical Tamm structure : r_{BM} is the reflectivity of the Bragg mirror, r_M is the reflectivity of the metallic surface and Φ is the phase introduced by the light propagation between these two effective mirrors.

$$r_{BM} r_M exp(2i\Phi) \approx 1 \tag{2.7}$$

which can also write as :

$$\phi_{Metal} + \phi_{BraggMirror} + \phi_{propagation} = 2\pi l \tag{2.8}$$

where l is an integer.

In the original paper of M. Kaliteevski et al [1], a Tamm state with zero propagation phase ($\Phi = 0$) is defined : the Bragg mirror and the metal layer are in direct contact. The resonance condition is then $r_M r_{BM} \approx 1$. It can be fulfilled because both the metallic layer and the Bragg mirror present a negative ≈ -1 reflectivity : the former comes from eq. 2.6, and the latter is true provided that, in the Bragg mirror, the medium of higher index is the one in contact with the metal ($n_a > n_b$). This structure can thus be seen as an optical cavity of null thickness ($\Phi = 0$), which means practically that the electromagnetic field will be confined over a small thickness localized at the Bragg-metal interface. Let us mention that, in our case, for fabrication reasons, the material in contact with the silver will be the lower-index material of the Bragg mirror ($n_a < n_b$). The resonance condition will then be achieved by introducing a thin layer of silica between the metal and the Bragg mirror, so that a minor increase of the mode confinement thickness will be introduced (as discussed later in this chapter).

As mentioned above, $|r_{BM}|$ can be close to 1 for high number of layers. The phase of the

reflection coefficient varies then linearly as a function of ω in the stop band [4] :

$$r_{BM} = \text{sign}(n_b - n_a) exp(i\beta \frac{\omega - \omega_0}{\omega_0}) \tag{2.9}$$

with

$$\beta = \frac{\pi n_a}{|n_a - n_b|} \tag{2.10}$$

Finally by applying equation 2.6 and equation 2.9, the resonance condition writes :

$$2\Phi + (\sigma\pi + \beta \frac{\omega - \omega_0}{\omega_0}) + (\pi + \frac{2n_a\omega}{\sqrt{\varepsilon_r}\omega_p}) = 2\pi l \tag{2.11}$$

with σ equal to 1 when $n_a > n_b$ and to 0 otherwise.

2.1.2 State-of-art of 2D Tamm structure

Motivated by these proposals and by the demonstration in 2011 that Tamm states could be confined in three dimensions (see next section), various authors have considered Tamm structures.

J. Lakowicz et al [3, 6] have published a series of studies on the fluorescence of a layer of molecules inserted inside a Bragg-metal Tamm structure. Emission of the molecules into the optical Tamm states was evidenced from the emission patterns. The coupling showed a dependence on the emitter position with respect to the structure electric field distribution : if the emitters were positioned between the metallic layer and the Bragg mirror, the Tamm mode was excited efficiently, while if the emitters were on top of the metallic layer, they excited more efficiently the surface-plasmon polariton (SPP) states at the upper interface between the metal and the air.

The strong coupling between the Tamm and SPP states has also been demonstrated as an anticrossing between their dispersion relations [7, 8]. We can illustrate this effect by calculating (fig. 2.4) the reflectivity spectrum of our Tamm structures (on a glass substrate) for various incidence angles (inside the glass substrate). The Tamm and SPP modes appear as dips in the reflectivity spectra corresponding to excitation of these modes. They anticross at 550 nm, indicating strong coupling between these modes. Although the Tamm and SPP modes are

localized at different positions (respectively between the metallic layer and the Bragg mirror and at the surface of the metallic layer), there is still an overlap between these modes, which is responsible for this coupling. It can be shown that the coupling decreases (the anticrossing energy decreases) as a function of the metal thickness. For our study, as we focus on the spectral part which is close to the fundamental mode (close to 650 nm) in figure 2.4, we can neglect SPP-coupling effects.

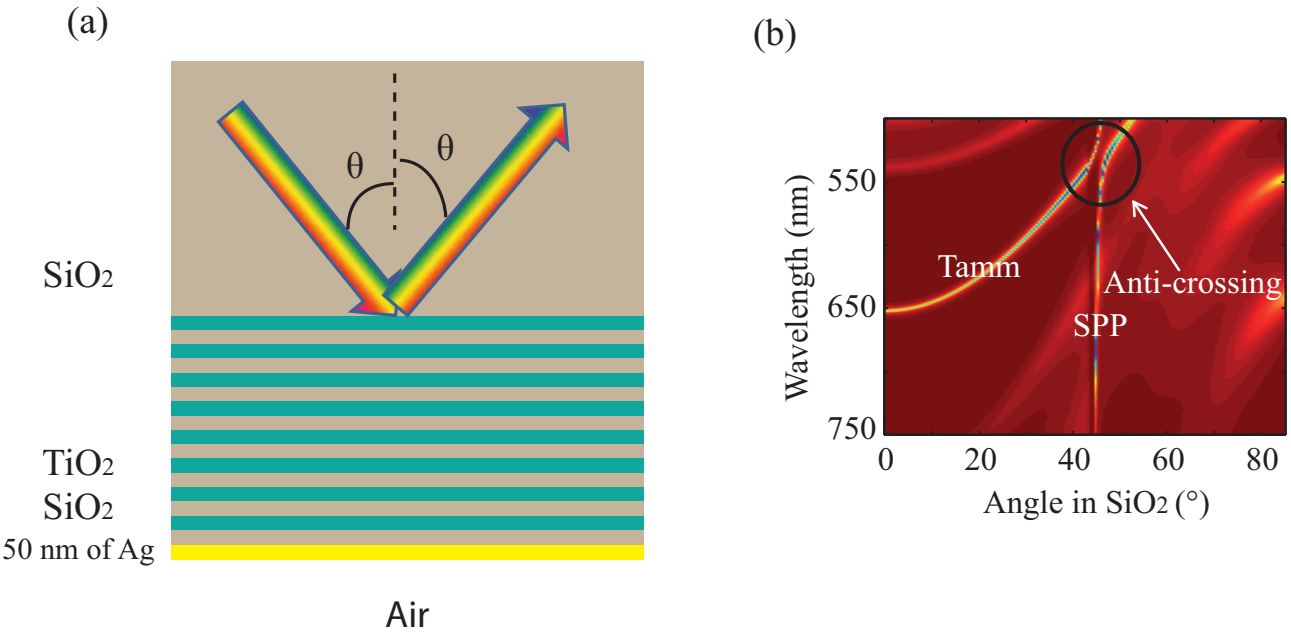

Figure 2.4: Simulated angular resolved reflectivity spectrum for a Tamm structure: (a) Schematic representation of the simulated Tamm structure, the Bragg mirror is composed by 6 pairs of TiO_2/SiO_2 at $\lambda/4$ + 105 nm of SiO_2 and the metal is made by 45 nm of silver. The substrate is SiO_2 with infinity thickness to simulate the Kretschmann configuration; (b)Simulated angular resolved reflectivity spectrum, the Tamm mode resonance is located at around 650nm when $\theta = 0°$, the surface plasmon line is located at $\theta = 45°$. At 540nm, there is an anti-crossing between the Tamm mode line and the surface plasmon line which demonstrate the strong coupling between them

2.1.3 State-of-art of 0D Tamm structure

By replacing the metallic layer by a disk of same thickness and micrometer radius, the Tamm state can be confined vertically near the Bragg-metal interface plane but also laterally under

the metallic disk. We will refer to these states as "0D Tamm states" as they are localized in three dimensions, and call the states described in the previous sections "2D Tamm states".

0D Tamm states were first demonstrated in 2011 by P. Senellart et al. at the Laboratoire de Photonique et Nanostructures (LPN) in Marcoussis [9,10] : a layer of epitaxial quantum dots are embedded inside the Tamm structure, and a metallic disk was deposited by optical lithography. The lateral confinement was evidenced in the near-infrared region by measuring the emission dispersion relation from different disks with different diameters. Instead of coupling a layer of epitaxial quantum dots, individual quantum dots were also coupled to this structure by using the in-situ optical far-field lithography technique [11] which allows to position the disk centered on a quantum dot (see section 3.6.1). A Purcell factor of 2.5 for resonant emission was recorded.

Coupling of single quantum dots to 0D Tamm structures was also studied by Braun. T et al [12], demonstrating enhancement of fluorescence. The influence of temperature on the sample luminescence has also been studied experimentally.

Emission of a quantum well inside a 0D Tamm structure was studied by J. Bellessa, C. Symonds et al. at the Institut Lumière-Matière (ILM) in Lyon. Laser emission into the Tamm modes has been demonstrated [13]. By changing the geometry of the top metal disk (replacing it with a rectangle disk for example), the laser polarization could also be manipulated [14].

In the context of nanophotonics and coupling to fluorescent emitters, Tamm states thus offer the possibility to confine electromagnetic modes in three dimensions to small volumes, leading to Purcell effects, lasing etc. The confinement is provided only by depositing a metallic pattern (disk, rectangle...) on a Bragg mirror, so that powerful and versatile deposition protocols (involving for instance in-situ lithography) can be used.

2.2 Choice of experimental Tamm structure

We now describe the choice of the experimental Tamm structure for this chapter : numerical simulations (transfer-matrix method) were used in order to optimize the 2D Tamm properties.

2.2.1 Position of the problem

We study the optical Tamm modes at room temperature and in the visible range by embedding a layer of colloidal nanocrystals inside the structure. In order to couple the emission from the nanocrystals to the optical Tamm mode, both spatial and spectral agreement are needed : the layer of nanocrystals must be positioned vertically at the maximum of the electric field, and the Tamm mode must be at resonance with the nanocrystals emission.

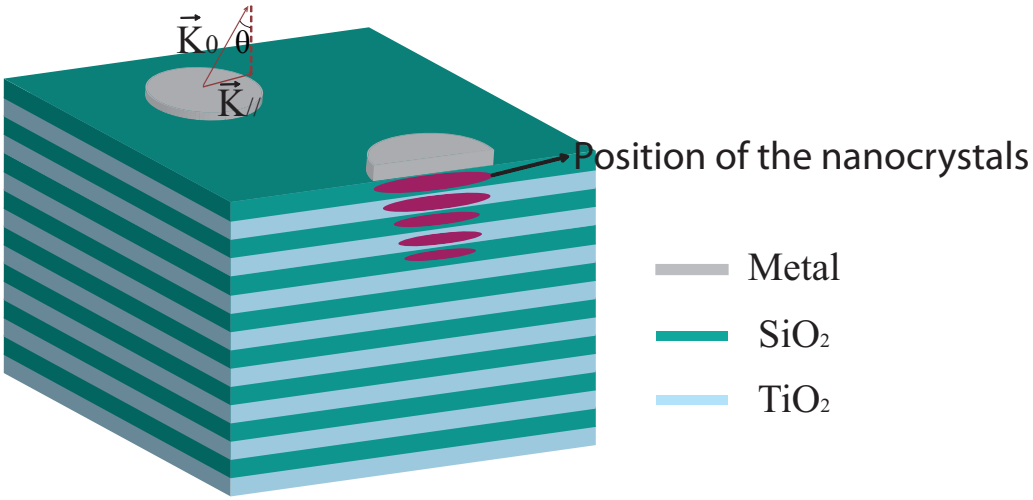

Figure 2.5: Schematic of the 0D Tamm structure. The nanocrystals should be embeded into the structure and located at the place where the electric field is maximum

We used extremely bright and stable CdSe/CdS nanocrystals provided by the group of B. Dubertret (see nanocrystals characterization in the first section) with an emission centered at 640 nm. We chose TiO_2 and SiO_2 as the dielectric materials for the Bragg mirror as they are widely used in the visible range for Bragg mirrors and other thin-layer structures and their deposition is well controlled ; TiO_2 provides a high optical index contrast with SiO_2 : $\Delta n = 0.85$. Figure 2.5 shows a schematic of the designed optical Tamm structure. The nanocrystals should be between the Bragg mirror and the metallic layer, where the electric field is maximum (the exact position will be calculated later). It cannot however be directly covered by the metal (or at less than 10 nm below the metal) as proximity with the metallic layer would induce very strong quenching of the luminescence. Evaporation of a material on top of colloidal nanocrystals is also able to damage their luminescence properties. We chose to cover the nanocrystals with silica, material for which we had most experience (and still some loss of fluorescence was found as discussed below). We are then in the case $n_a < n_b$, so that the

upper layer of silica must be tuned to create a dephasing Φ as described above, as compared to the situation ($n_a > n_b$) described by Kaliteevski. In spite of this additionnal silica thickness, the confinement depth of the electromagnetic field is not strongly modified, as shown by a comparison of the electric field distributions for the two structures (fig. 2.6).

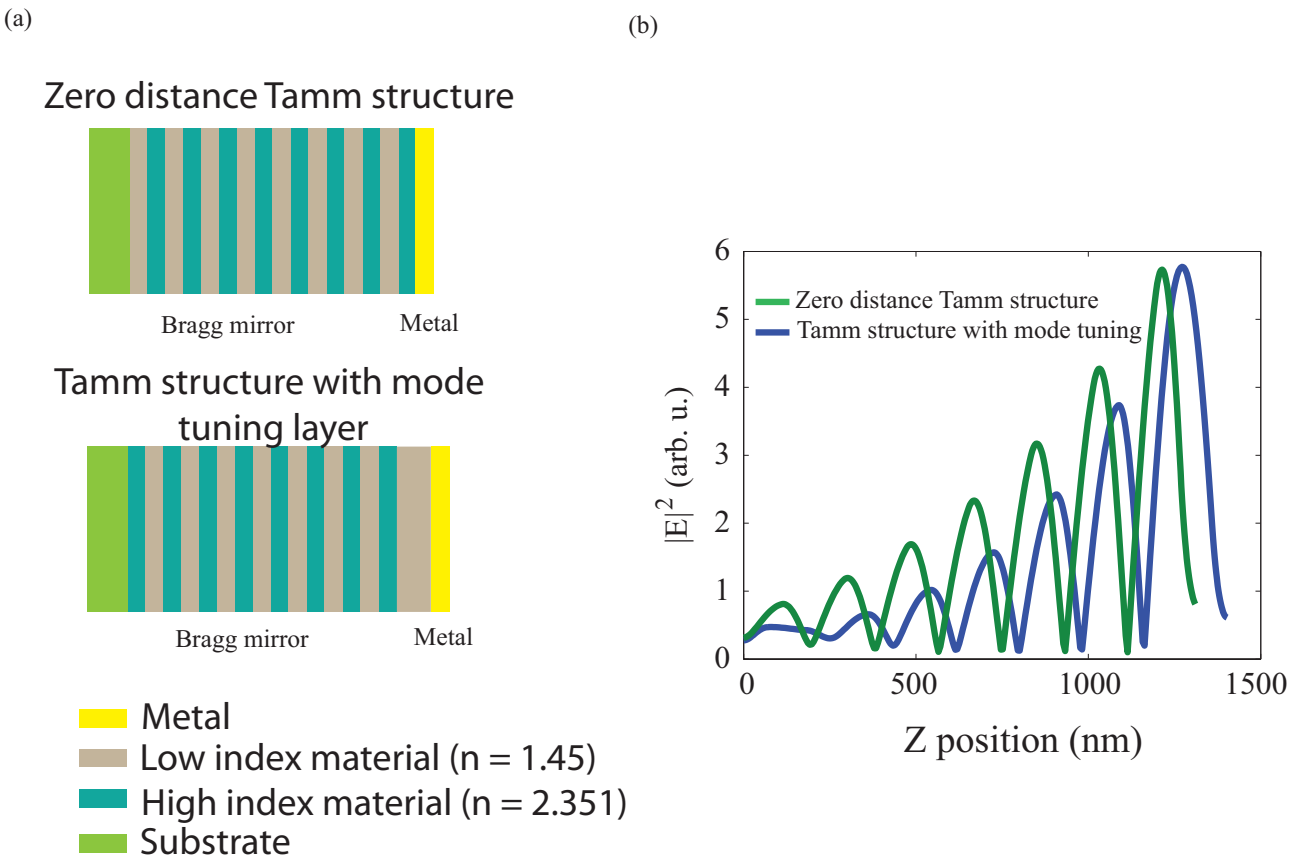

Figure 2.6: (a) Schematic of two different Tamm structures. Top : a Tamm structure with zero dephasing Φ. Bottom : the Tamm structure studied in this PhD : a layer of dielectric is added between the Bragg mirror and the metal layer to tune the resonance wavelength. (b) Electric field intensity $|E|^2$ distribution of the corresponding Tamm state along the z-axis of the structure (7 pairs of quater wave TiO_2 and $/SiO_2$ on Si substrate and 45 nm of silver on top).

2.2.2 Simulation method

In order to characterize the Tamm states, we calculate (as was done already in fig. 2.4) the reflectivity spectrum of the Tamm structure : the reflectivity is mostly close to unity due to

reflection by the metal layer, but it drops for specific values of ω and angle of incidence θ corresponding to absorption by the Tamm mode. This absorption is possible when the in-plane wave vector of the photon matches the wave vector $K_{\parallel}$ of the Tamm state :

$$K_0 sin(\theta) = K_{\parallel} \tag{2.12}$$

where $K_0 = \omega/c$ is the wave vector of the incident beam.

We have performed the simulation with Film-Wizard software which is based on the transfer-matrix method. The transfer matrix is an analytical method which can be used to describe multi-layer optical systems. The principle is that light propagation through each layer and interface can be described by a transfer matrix : this matrix will include dephasing effects and Fresnel reflection coefficients and eventually will depend on the optical index and the thickness of the layer and the incidence angle. Thus if the electric field is known at the beginning of the system, the electric field at the end of the system can be obtained by multiplying the incident electric field vector by the product of the transfer matrices of the different layers.

For the present simulations, the optical index was 2.351 for TiO_2 and 1.45 for SiO_2 (as given by ellipsometric measurements). As explained previously, we use silver as it has much less losses in the visible range (compared with gold which is widely used in the infrared range), and the optical index of silver is taken as $n = 0.05 + 4.25i$. The substrate was silicon.

2.2.3 Calculation for the Bragg Mirror

First, we calculate the reflectivity spectrum of a TiO_2/SiO_2 Bragg mirror (centered at $\lambda =$ 640 nm) with respect to its number N of SiO_2/TiO_2 pairs. It is important that the reflectivity is high so that the structure does not have a significant losses. Theoretically, a large N should be preferred. However, deposition of a very large number of layers can cause fabrication difficulties and risk of more sample defects (especially as it might require to open the deposition machine and load more source materials).

Figure 2.7 shows the reflectivity spectrum of a Bragg mirror for different values of N. As N is increased, the reflectivity of the stop band increases as given by eq. 2.1, while the stop band width tends towards the asymptotic value given by eq. 2.2. When the number of pairs is greater than $N = 7$, the increase of the reflectivity is no longer significant, and the reflectivity is

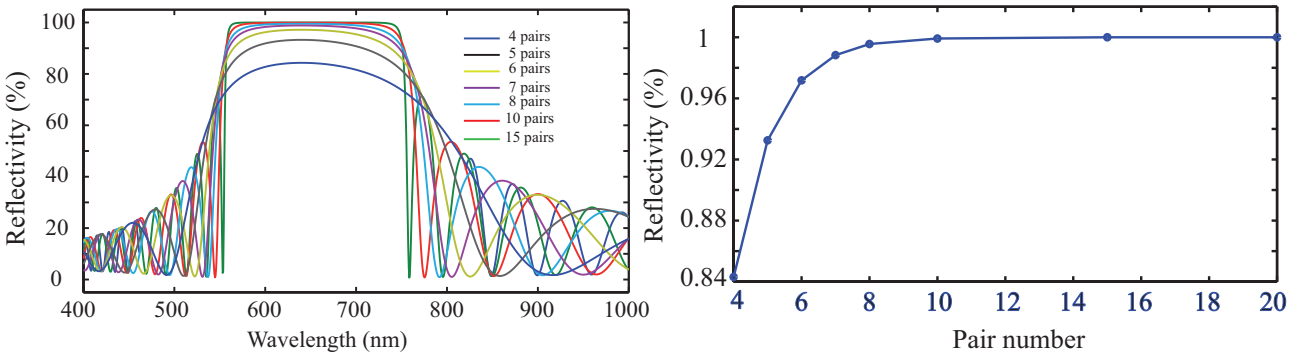

Figure 2.7: Left: simulated reflectivity spectra of a TiO_2/SiO_2 Bragg mirror (centered at 640 nm) for various values of the number of TiO_2/SiO_2 layers pairs. Right: reflectivity of this Bragg mirror at 640 nm as a function of the number of pairs.

more than 98% already (higher than the reflectivity(around 96%) of a SiO_2/45 nm Ag interface which is the top part of the Tamm structure). We thus will choose $N = 7$ pairs TiO_2/SiO_2 for the Bragg mirror of our Tamm structure.

2.2.4 Calculation for the spectral tuning layer

In order to provide the phase term Φ and match the Tamm frequency to the nanocrystals emission, an intermediate layer of SiO_2 can be added on top of the Bragg mirror, below the silver layer. Figure 2.8 shows the simulated reflectivity spectra of a 7 pairs TiO_2/SiO_2 with a $45nm$ silver layer on top and with different thicknesses of the mode tuning layer. Now, due to the addition of the silver layer, the Tamm mode appears as a strong absorption dip inside the stop band. The optical Tamm mode resonance wavelength can be tuned in the entire stop band of the Bragg mirror by changing the thickness of the intermediate silica layer. The roughly linear dependance of ω on the SiO_2 thickness (which itself is proportional to Φ) is in agreement with the resonance condition expressed by eq. 2.11.

We choose to tune the Tamm mode at the center of the Bragg stop band in order to minimize the effects of fabrication uncertainties (such as an error on the thickness of this silica tuning layer). Expecting that the lateral confinement effect for the Tamm 0D structure will blue shift the resonance wavelength by about 10 nm [9], we tune the 2D Tamm state to 650 nm in order to obtain a 0D Tamm state at 640 nm. We then need to include 94 nm more of SiO_2 between the Bragg mirror and the silver layer.

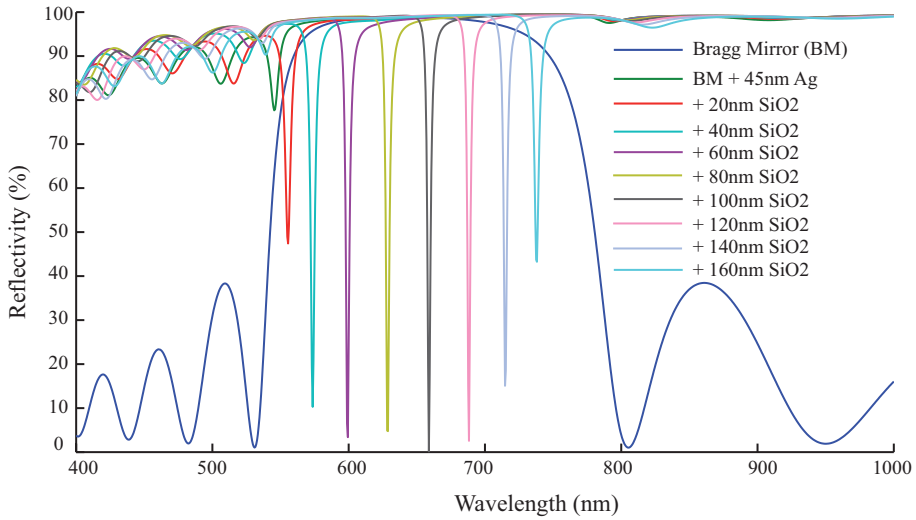

Figure 2.8: Simulated reflectivity spectrum of a Tamm structure with a TiO_2/SiO_2 Bragg mirror centered at 640 nm, a 45-nm silver layer and various thicknesses of the intermediate spectral-tuning silica layer at normal incidence.

2.2.5 Calculation for the metallic layer

Finally, we plot on figure 2.9 the reflectivity spectrum of a Tamm structure with 7 pairs of TiO_2/SiO_2, covered by a supplementary 94-nm layer of SiO_2,and a layer of silver with different thicknesses. The Tamm mode wavelength is not strongly shifted as a function of the silver thickness : the reflection coefficient r_M of the silver layer is not strongly modified by the layer thickness as long as it remains (slightly) larger than the electromagnetic field penetration depth inside silver (note that r_M in eq. 2.6 was expressed only for infinite silver layer thickness).

Figure 2.9 also shows that by increasing the thickness of silver layer, the quality factor of Tamm structure (defined as the ratio between the mode frequency and full width at half maximum) can be increased. This can be explained by the increased reflectivity of the silver layer. However, if the silver layer is thicker than 45 nm, the depth of the dip on the reflectivity spectrum decreases ; it means that the optical Tamm mode is less accessible : it is hard to extract photon from such structure because the silver layer is too thick. We chose to deposit a 45-nm layer of silver as a good trade-off.

Eventually, on this silver layer, a thin layer of polymer will be deposited to protect the silver from being oxidized. This layer will have little effect on the Tamm mode as this mode has very weak electric field in the region above the silver layer.

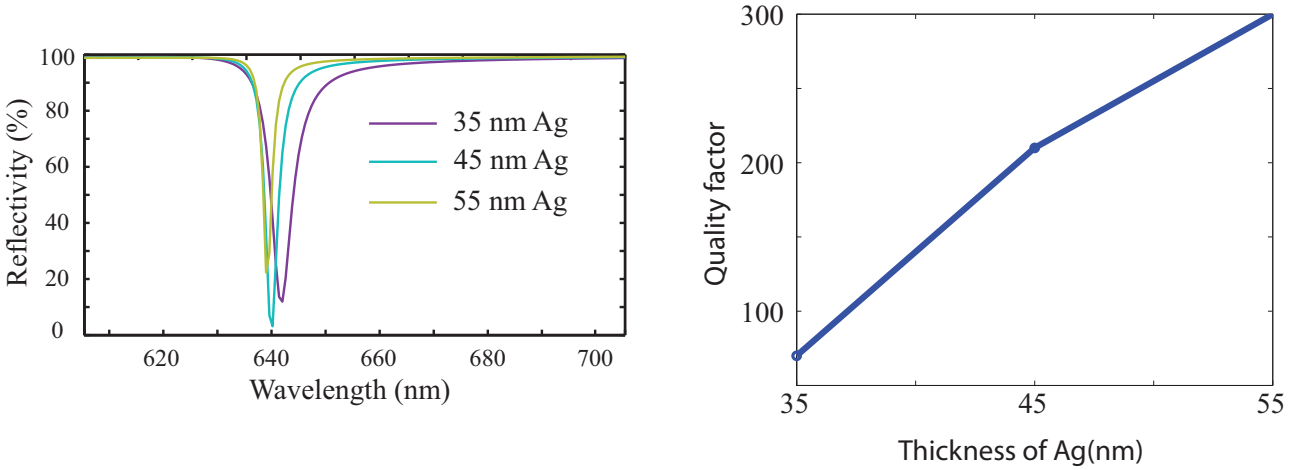

Figure 2.9: Left : simulated reflectivity spectra of the Tamm structure with different silver thicknesses. Right : quality factor of the Tamm structure as a function of the silver thickness. For both figures, the Bragg mirror is made of 7 pairs of TiO_2/SiO_2, centered at 640 nm, covered by a supplementary 94 nm of SiO_2 below the silver layer.

2.2.6 Conclusion on desired sample structure

Let us summarize the fabricated structure : on a silicon substrate, we will deposit 7 pairs of TiO_2/SiO_2, and on the top layer of SiO_2, we need put another 84 nm of SiO_2 to tune the mode position, and finally, on top, there is a 45-nm silver layer, covered by 50 nm of PMMA (which has around same index as silica).

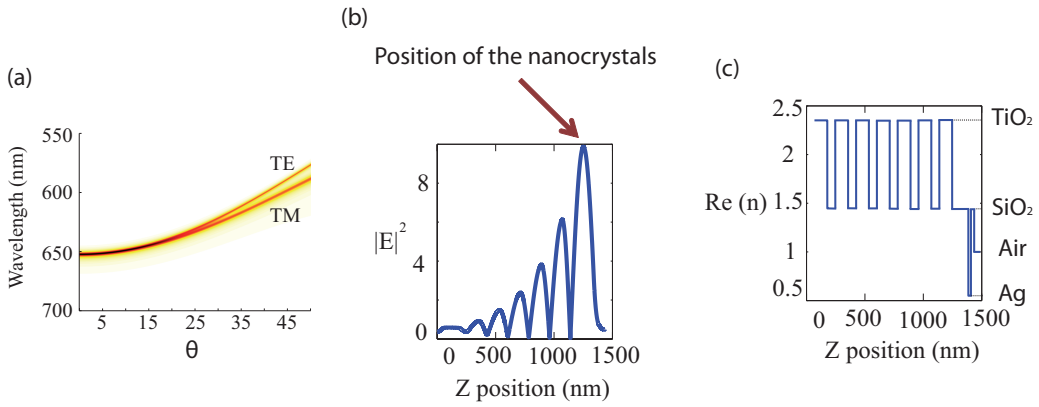

Figure 2.10: (a) Simulated angular resolved reflectivity spectrum of the Tamm structure mentioned above. (b) Intensity distribution $|E|^2$ along the optical axis of the 2D Tamm structure. The arrow indicates the maximum, where the emitters should be located for maximal coupling. (c) Distribution of the real part of the optical index inside the Tamm structure.

Figure 2.10(c) shows the corresponding index profile for this structure. Fig. 2.10(a) shows the simulated dispersion relation : the reflectivity curve presents a parabolic shape as a function of θ (the plasmon wave vector being given by $k_{\parallel} = (\omega/c)\sin\theta$), with an energy minimum ($\lambda = 650\,\text{nm}$) at $k_{\parallel} = 0$. The TE and TM modes are degenerate at this fundamental for symmetry reasons, and there is a lifting of degeneracy when $k_{\parallel}$ increases.

Figure 2.10(b) shows the electric field distribution inside the 2D Tamm structure. In order to optimize the coupling between the nanocrystals and the optical Tamm structure, the nanocrystal should be placed at the position where the electric field norm is maximal, which is 105 nm below the silver layer.

2.3 Sample fabrication

The fabrication of the Tamm structures was performed as follows : 6 pairs of quarter wave (TiO_2/SiO_2) layers (centered on 640 nm) were deposited by molecular beam epitaxy on a silicon substrate. Another layer of quarter wave of TiO_2 and $80nm$ of SiO_2 were then deposited (fabrication at the LPN by Xavier Lafosse as part of our collaboration with Pascale Senellart). The measured and simulated reflectivity spectra are shown in figure 2.11. The measured reflectivity shows a maximum value at around 92% and the reflectivity is higher than 90% between $600nm - 702nm$. On the simulation, the maximum reflectivity can raises up to 99.6% and the reflectivity is higher than 90% between $557nm - 737.2nm$. This indicates some fabrication imperfections (also clear from the shape of the fringes outside the stop-band) which were due to technical problems (the in-situ ellipsometer which should have monitored the layers thickness was not working) during the sample fabrication. We will see below that this sample is however sufficient to obtain a good coupling of nanocrystals to Tamm modes.

A layer of CdSe/CdS nanocrystals was then spin coated on the surface at 4000 turns/s during 40 s. The nanocrystal concentration led to an estimated density of 6000 nanocrystals/μm^2. A 60-nm layer of PMMA was then spin coated on top of the nanocrystals immediately to avoid the nanocrystas from being damaged by oxidation and also from being damaged for the following fabrication steps. We had found, indeed, that nanocrystals were severely damaged when a silica layer was deposited directly on top of them (protocol developped during the thesis of Dhawan Amit Raj). Another 55-nm layer of SiO2 was then deposited by thermal evaporation with an

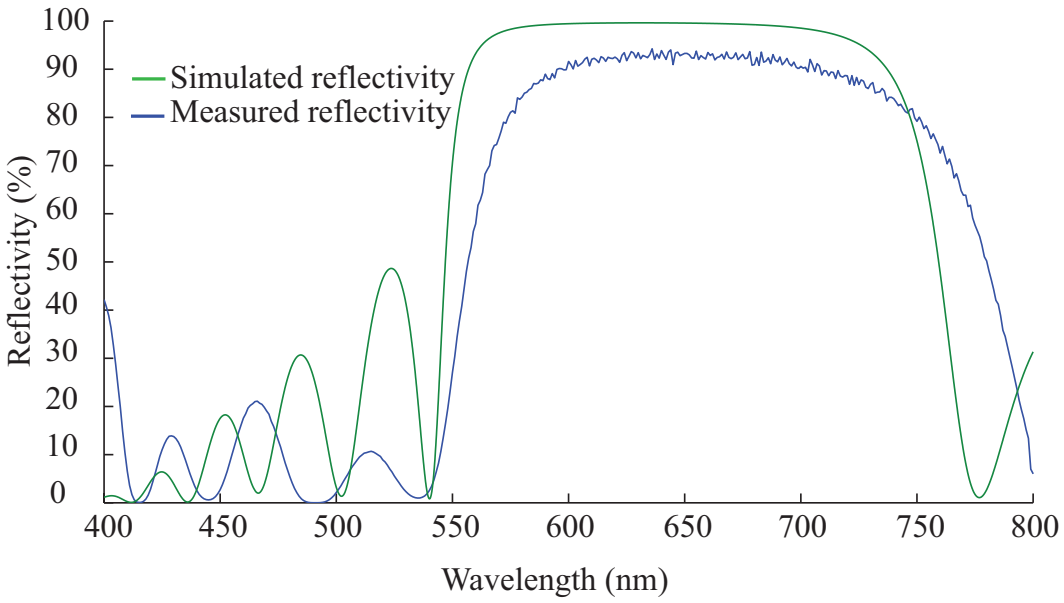

Figure 2.11: Simulated and measured reflection spectra of the fabricated Bragg Mirror.

electron gun as we found it was the only method to deposit silica on top of nanocrystals without damaging the nanocrystals.

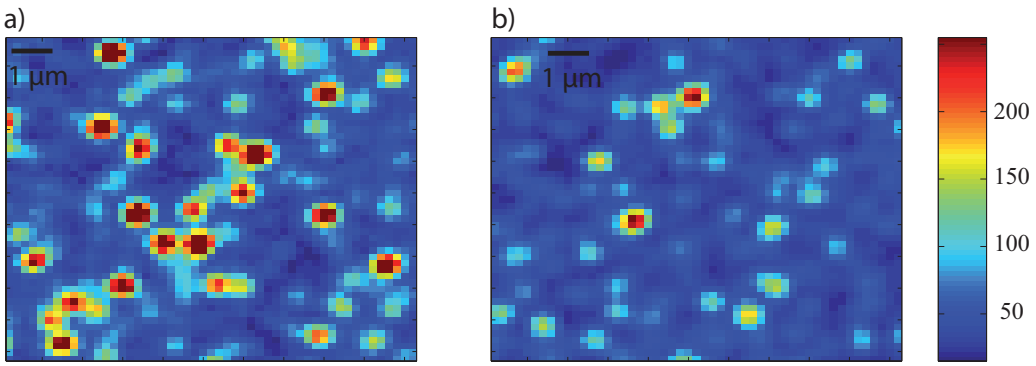

Figure 2.12: (a) Fluorescence image of the sample before SiO_2 deposition. (b) Fluorescence image of the sample after SiO_2 deposition (the color bar is valid for both measurements, which were recorded with same acquisition parameters).

Figure 2.12 shows the fluorescence image of the sample before and after the SiO_2 deposition under the illumination of the same lampe and detected with same microscopy system and parameters. On fig.2.12(a), the emission occurs everywhere on the sample (note that the intensity is not zero for the blue color ; moreover we could see a continuous red background when looking into the microscope eyepiece). This indicates that the nanocrystal distribution is somehow continuous on the sample surface. Above this layer of continuous nanocrystal layer,

some big clusters are observed (the red points). Figure 2.12(b) shows that the intensity of the emission from the continuous nanocrystal layer is not strongly modified (although some of the big clusters might have been degraded in spite of the first coverage by a protective PMMA layer). The nanocrystals emission is thus (mostly) not lost by this coverage method. The sample is then cut into two pieces ; on top of one piece we deposit directly 45 nm of silver and spin coat it by 50 nm of PMMA. By this way, a 2D Tamm structure is fabricated.

On the other piece of the sample, disks from $1\mu m$ to $10\mu m$ diameter were deposited by optical lithography. No lift-off was performed in order to facilitate the observation of the disk emission : if the surrounding silver layer was removed, luminescence from outside the disk would be much higher and hide the luminescence from the disk itself. After the deposition of silver, a 50-nm layer of PMMA is spin coated on the sample for protecting the silver from being oxidized. Figure 2.13 shows the entire fabrication procedure.

2.4 Coupling of the nanocrystals to the optical Tamm structure

2.4.1 2D Tamm structures

We first characterized the 2D Tamm structure. The reflection spectrum was measured at various incidence angles with a goniometer as shown on fig. 2.14. The illumination fiber and the detection fiber were placed at the same angle. A white collimated source (generated by a supercontinuum laser and a collimator) illuminated the sample surface, and the reflected beam at the same angle was collected by a detection fiber and sent to a spectrometer. The detection was made for angles between 20^o to 70^o, the measured spectra were normalized by the source spectrum, measured with the two fibers facing each other.

Figure 2.15(a) shows the measured reflectivity spectra of the fabricated 2D Tamm structure at various incidence angles. For each angle, there is a dip in the reflection curve which is due to the absorption of light by the 2D Tamm mode. The mode is blue-shifted when the incidence angle increases, in agreement with theory. The degeneracy lifting of the TE and TM modes at high incidence angle is also observed. The measured quality factor on these spectra is around 80. This is less than the simulated value (200), probably because of the Bragg mirror fabrication

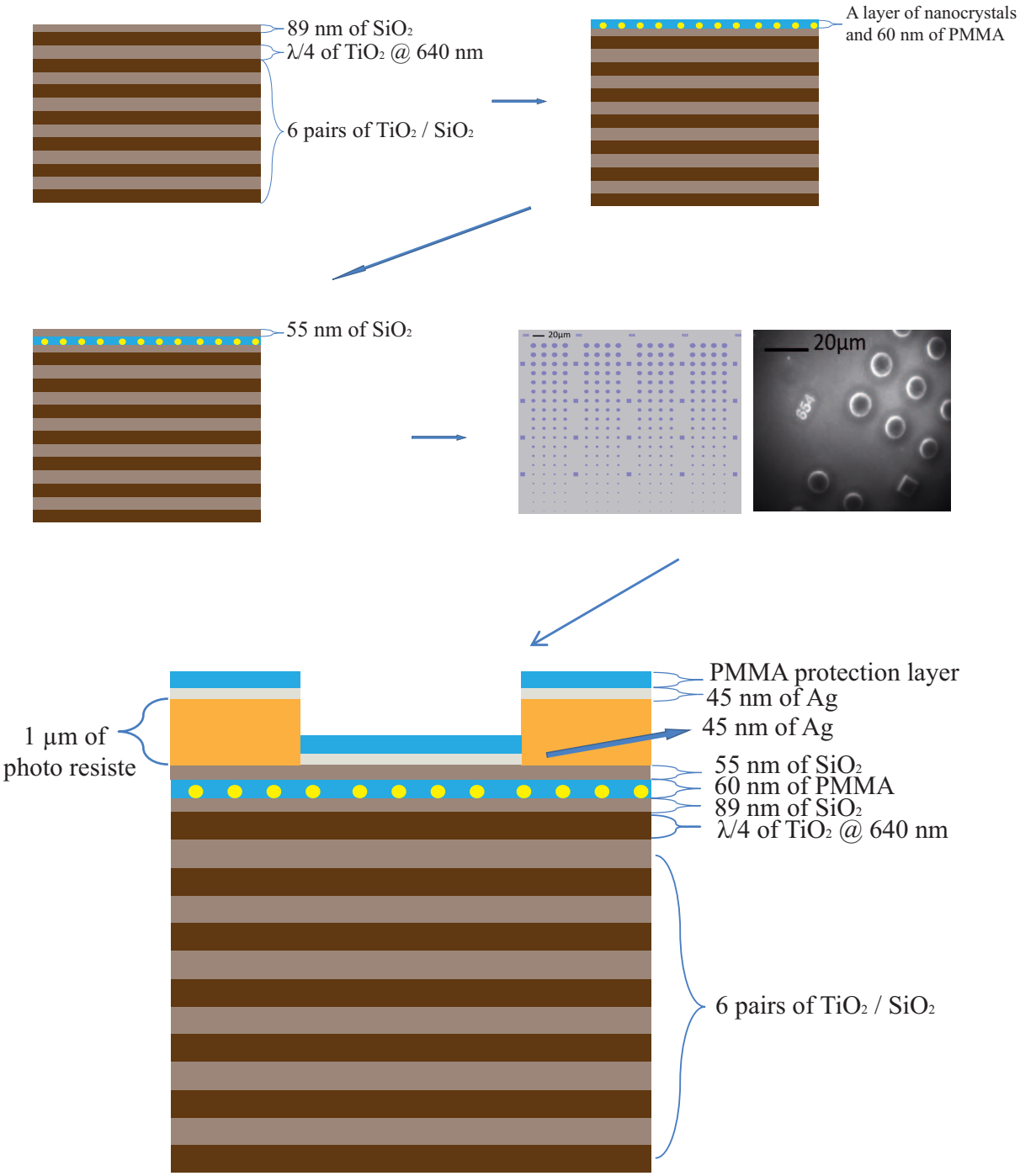

Figure 2.13: Sample fabrication procedure

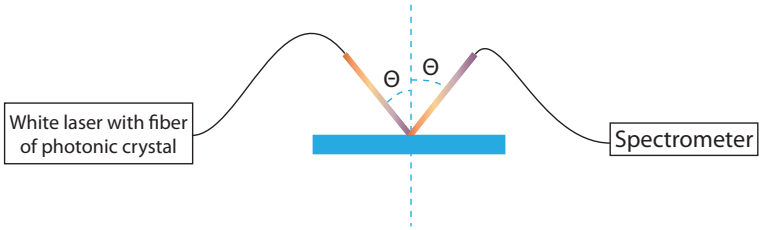

Figure 2.14: Schematic presentation of the goniometer.

imperfections which were mentioned before. When comparing quantitatively the experimental 2D Tamm dispersion relation with the simulated one (fig. 2.15(b)), we find that the measured dependance on θ is the same as simulated but with a blueshift of 0.07 eV, most likely due to the imperfect control of the thickness of the PMMA layer which covers the nanocrystals, and possibly also because of Bragg mirror imperfections (a small perturbation in the periodicity of the structure will introduce significant phase change on the reflection). The Tamm mode will however remain in the emission range of the nanocrystals.

We now consider the emission from the nanocrystals embedded inside the Tamm structure. A continuous laser at 470nm with power of $3.3\mu W$ is used to excite the emitters. The laser beam is reflected by a dichroic mirror with a cut-off wavelength of 510 nm and then focused by an air objective with 0.7 numerical aperture. The emission is collected by the same objective and filtered by the dichroic mirror and a long pass filter with a cutting wavelength at 532 nm and a band pass filter with a central wavelength of 632 nm and bandwidth of 92 nm. The Fourier plane of the sample is conjugated onto the entrance slit of the spectrometer as detailed in the first chapter.

The measured data is shown on fig. 2.16, which plots the emission wavelength as a function of its direction $\sin\theta = K_{\parallel}/K_0$, an image which we will refer to as dispersion relation. The nanocrystal emission is mainly into the parabol-shaped dispersion relation of the optical Tamm modes, with no detectable direct emission. The Tamm mode emission dispersion relation is in good agreement with the measured reflectivity spectrum (indicated by green dots), with a quality factor of the order of 100. The degenerescence of the TE and TM modes at high emission angles is also observed.

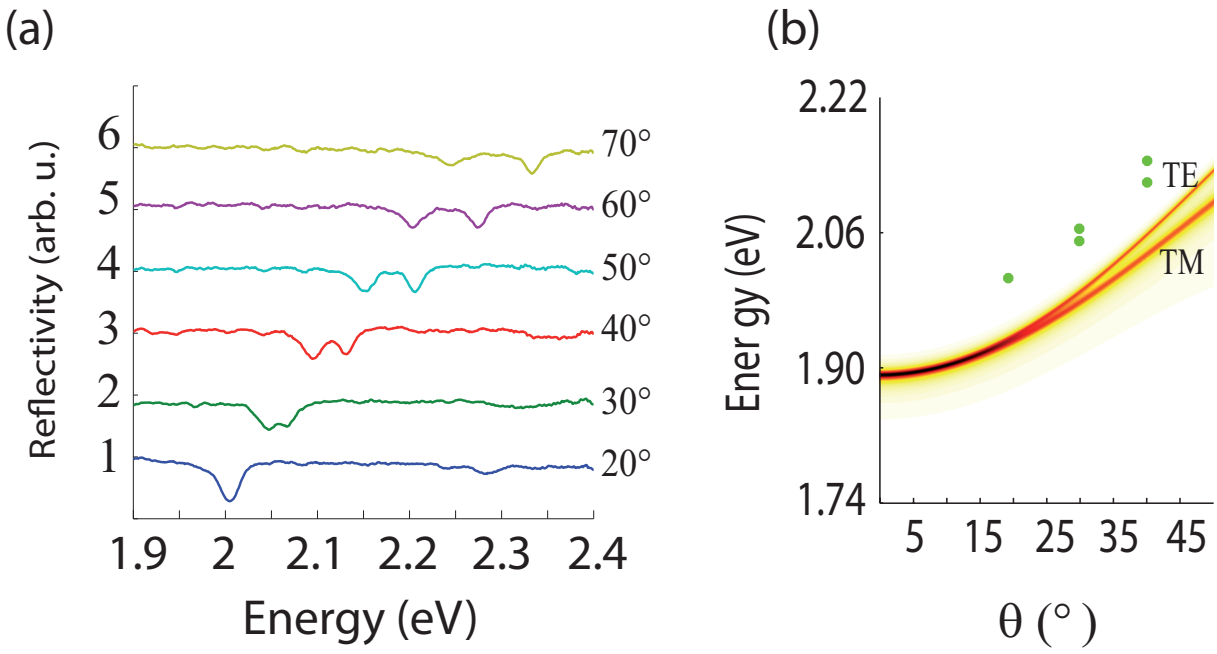

Figure 2.15: (a) Specular reflectometry spectra (arb. un., shifted for clarity) of the 2D Tamm sample measured at several incidence angles. (b) Theoretical dispersion relation E(θ) of the 2D Tamm structure (transfer-matrix calculation), with refractive indices 1.45 for SiO2 and PMMA (given by ellipsometry measurements), 2.351 for TiO2 (given by ellipsometry measurements), 0.05+4.25*i for silver. Green dots : experimental dispersion relation $E(\theta)$ obtained from the dips of the reflectivity spectra.

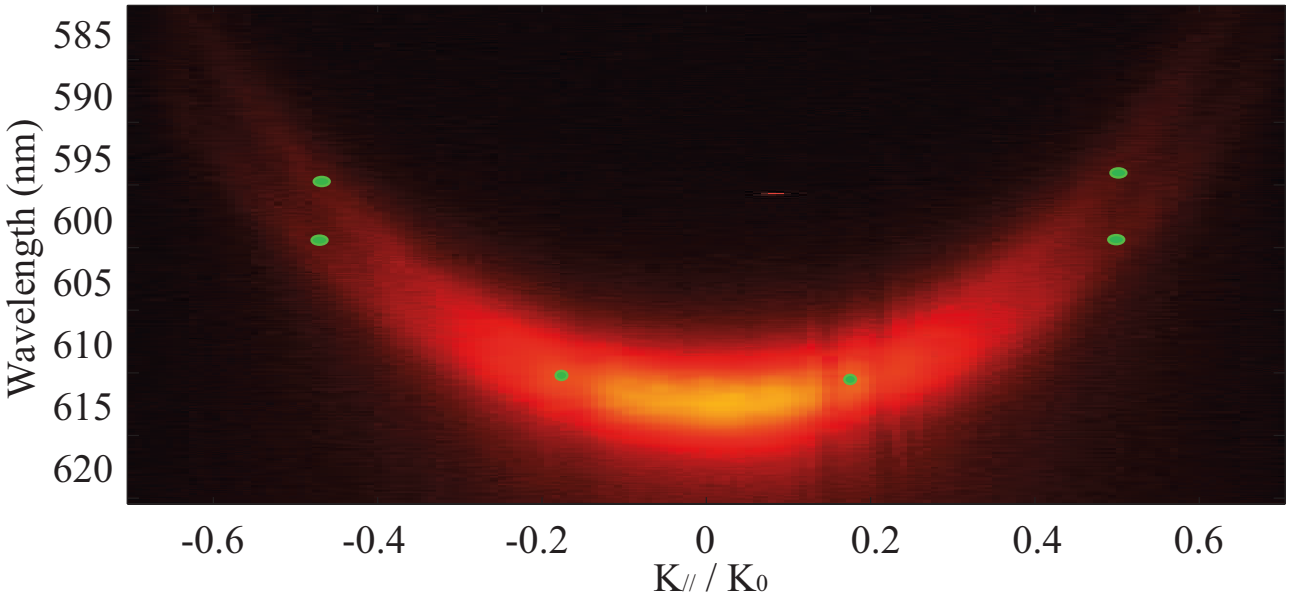

Figure 2.16: Photoluminescence from the 2D-Tamm sample analyzed as a function of wavelength and emission angle $\sin\theta = k_{\parallel}/k_0$. The green dots indicate the 2D-Tamm dispersion relation obtained from the reflection spectra.

2.4.2 Confinement effect of 0D Tamm structure

In order to study the lateral confinement effects, the dispersion relations of 0D Tamm structures with different disk diameters have been measured. The nanocrystals were excited by a continuous laser (470 nm, 3.3μW) at the center of the disk and the Fourier plane of the sample was again imaged onto the entrance slit of the spectrometer.

We see from figure 2.17 that emission from a 10 μm disk is the same as emission from a 2D sample : this disk is too large to observe confinement effects. When the disk diameter is smaller than $6\mu m$, the higher energy modes become less intense due to the confinement effect. It should be noted that, beside the Tamm mode emission, there are two other weaker parabolic curves : one at higher wavelength (above 630 nm) and the other at lower wavelength (below 600 nm) : this emission originates from the photoresist around the disk and follows the dispersion relation of the electromagnetic modes confined between the Bragg mirror and the outside silver layer. As the disk diameter becomes smaller, the emission from the photoresist becomes more important and is very strong for the 2 μm disk. As for the Tamm mode, the effect of confinement appears from the 6 μm disk as a reduction of the emission at higher energy. For the 4 μm disk, the dispersion relation consists mostly in a single discreete state

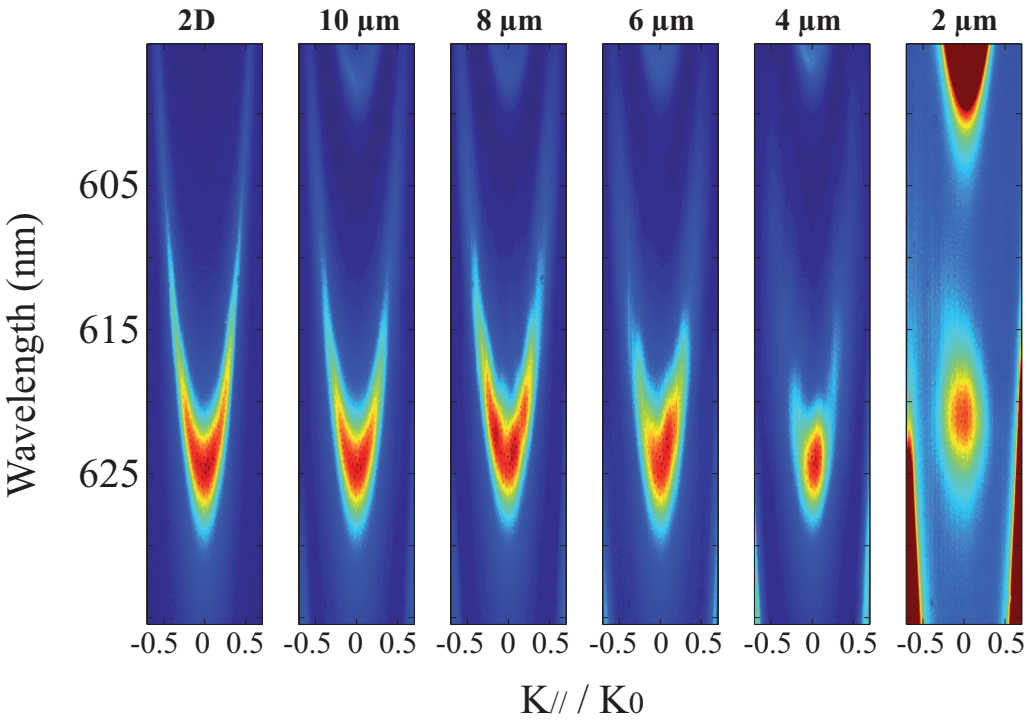

Figure 2.17: Dispersion relation of 0D Tamm structures for different disk diameters

at 624 nm. When the disk diameter reduces to $2\mu m$, the energy of the fundamental mode is blue shifted about 4 nm with respect to the 4-μm disk mode. As expected, confinment of the electromagnetic state leads to a discretization of the dispersion relation, with a shift to higher energy as the size on the photonic structure is reduced.

2.4.3 Theoretical simulations of the confinement effects

We have interpreted the behavior of the 0D Tamm structures by using finite-elements method as described below.

Introduction for finite elements simulations

The finite elements method is a numerical method for finding approximate solutions to boundary value problems for partial differential equations. It uses subdivision of a whole problem domain into simpler parts, called finite elements, and variational methods from the calculus of variations to solve the problem by minimizing an associated error function.

The perfectly-matched layers (PML) are a key element in these simulations : they are arti-

ficial absorbing layer for wave equations. They are often applied at the edges of the simulated structure to replace the boundary conditions and can efficiently absorb the incoming electromagnetic waves so that these waves can not go back into the simulated structure to pertubate the simulations. The configuration of the PMLs can have high influence on the performance of the PMLs. In order to create a PML which works properly, one needs to define the PML material and PML type (cartesian or cylindrical) depending on the simulation geometries.

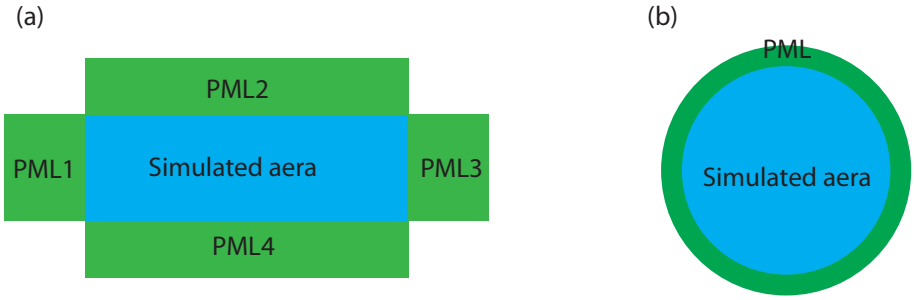

Figure 2.18: Schematic representation of different configuration of PMLs

Figure 2.18 shows two typical simulation geometries for PML configuration. For example, in Figure 2.18 (a), the PML should be defined as cartesian PML as the interface between the simulated aera and the PML is a line, and the four different zones should be defined seperataly. And for the configuration showing in Figure 2.18 (b), the PML should be defined as cylindrical PML as the interface is a circle. The material of the PML should be chosen as the same of the material in contact of the PML.

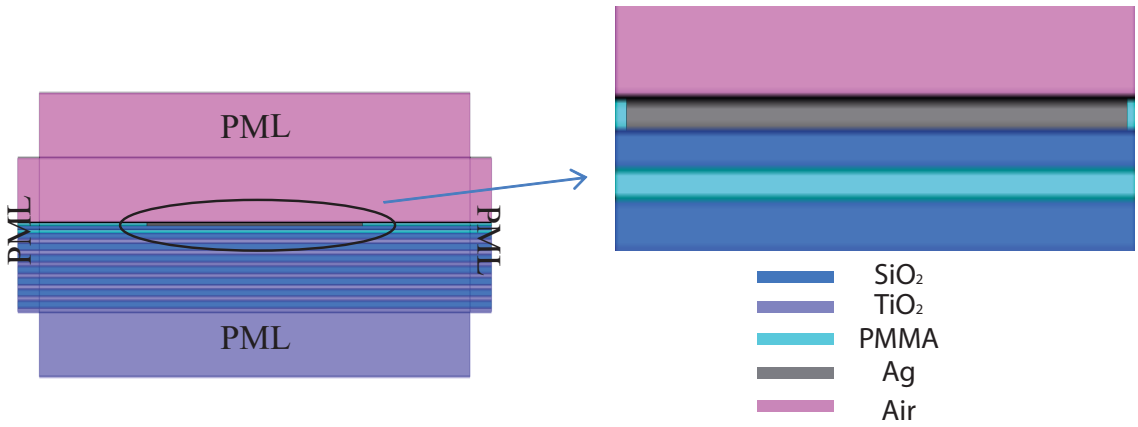

Figure 2.19: Schematic representation of the simulated structure

Figure 2.19 is an example of a schematic representation of a simulated structure. Different thicknesses and materials (optical index) can be defined for each layer. The PMLs are added

around the entire structure. It should be pointed out that the simulations were only 2D simulations as 3D simulations would be excessively long : the simulated structure is here a stripe of silver with translation invariance along the normal direction instead of a silver disk. The simulations are provided as a guide to qualitatively interpret the experiments but not as an accurate description of the system. However, they will prove quite efficient at describing our results.

Simulation results

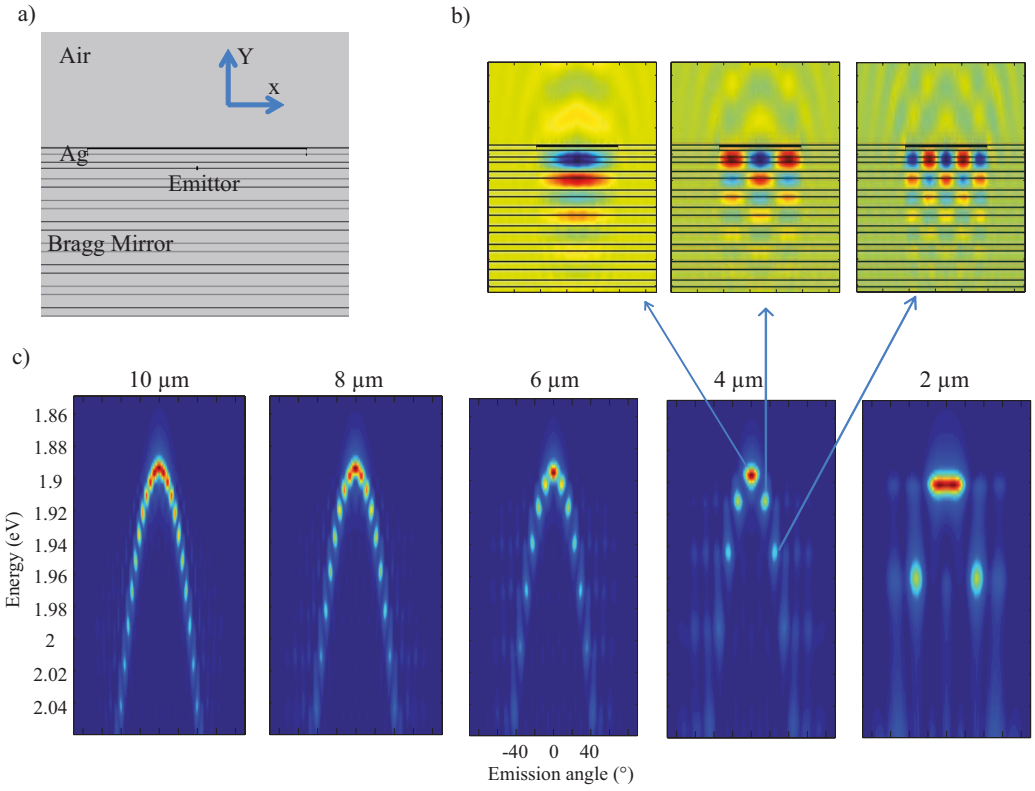

Figure 2.20: (a)Schematic representation of the simulated structure; (b) Simulated field E_x distribution inside the Tamm structure for certain wavelengths; (c) Simulated dispersion relation of the mode Tamm with different silver widths.

Figure 2.20 presents the simulations corresponding to the experimental results of the previous section. Figure 2.20(a) is a schematic representation of the simulated structure. A source horizontal dipole is introduced at the center of the structure and the radiation pattern is calculated for different excitation frequencies from 1.85 to 2.05 eV. Figure 2.20 (b) shows the simulated dispersion relation from the optical mode Tamm structure for different sizes. For

a 10 μm structure, discrete energy modes can be distinguished but their energy separations are very low. Discrete modes are not observed experimentally for the 10 μm disk, mostly due to the quite lower quality factor (note also that the most separated modes are the ones with higher energy, which would fall outside the emission range of the nanocrystals ; moreover, the 3D disk should present more modes than the simulated 2D structures, and the centered dipole in our simulation only excites the modes with even parity as the odd-parity modes have null electric field at the center). As the disk diameter decreases, the separation between the modes increases ; the fundamental mode experiences a continuous blue shift while the higher order mode becomes less intense and disappear. For the 2 μm size, only the first and the second modes are observed. Experimentally, a similar behavior is observed but only the fundamental mode can be distinguished. The calculated fundamental-mode blue-shift of 3.5 nm from the 4-μm to the 2-μm structure is close to the measured 4-nm shift measured on fig. 2.17. Figure 2.20 (b) shows the electric field distribution for some (even-parity) resonance wavelengths for a 4-μm size respectively 1, 3 and 5 lobes appear.

2.5 Spatially-resolved dispersion relation of the 0D-Tamm structure (10 μm disk)

2.5.1 Experimental configuration

As shown in the previous section, by conjugating the Fourier plane with the entrance slit of the spectrometer, one can measure emission with resolution on the photon energy (wavelength) and direction($K_{\parallel}/K_0$). However, the emission is summed over the entire structure. If spatial resolution is added on the measurement by selecting only the emission originating from a small sub-portion of the sample (located at position X), more local emission properties can be measured and further information is provided. However, spatial position X in the sample plane and emission direction $K_{\parallel}$ in the far-field are Fourier-related quantities as expressed in equation demonstrated in chapter of experimental set-up, which means that these two quantities can not be resolved simultaneously with infinite precision. This fundamental limit can be expressed as:

$$\Delta X * \Delta K_{\parallel} \geq 1 \tag{2.13}$$

The more the selection is precise (the size ΔX of the selected subportion decrease), the less the measurement on emission angle is precise (ΔK increases). In other words, the limit is given by diffraction : if we select only the emission from a subportion of the sample, the emission will be diffracted by this selection. The diffraction angle is given by 2.14 :

$$\Delta\theta = \frac{0.61\lambda}{R} = 0.45rad = 25.8^{\circ} \tag{2.14}$$

if we take $R = 0.85\,\mu$m the radius of the selected disk subportion of the sample, and 0.63 μ-m as λ.

The way to perform a spatial selection on the sample is to add a pinhole on the intermediate image plane as mentioned in the general presentation section. A short recall of the experimental configuration is shown in Figure 2.21.

As shown in Figure2.21, by adding a pinhole at the intermediate image plane, spatially resolved emission dispersion relation can be measured. The spatial resolution will be given by the size of the applied pinhole and so does the angular resolution due to the diffraction.

2.5.2 Measurements and results

As described above, a $100\mu m$ pinhole is added at intermediate image plane in order to select emission from $1.7\mu m$ disk of the sample surface. The pinhole is mounted on a motor in order to translate it along a direction x, which is oriented parallel to the spectrometer entrance slit (so that the measured wave vector is $K_{\parallel} = K_x$). The laser spot is around 1μm as dimension and kept at the center of the 10 μm disk. We label X the position which is probed by the pinhole. The emission dispersion relation for $X = 0, \pm\, 2\mu m$ is shown in Figure 2.22.

For all positions of the pinhole, the measured dispersion pattern is different from the case with no pinhole. When the pinhole is centered with respect to the silver disk, the emission pattern is symmetric and centered on $K_x/K_0 = 0$. When the pinhole is at $X = +2\mu m$, the emission pattern is no longer symmetric and most of the emission is to $K_x/K_0 > 0$. When the pinhole is at position $X = -2\mu m$, most of the emission is to $K_x/K_0 < 0$. The different portions of the 0D Tamm structure thus radiate light into different directions.

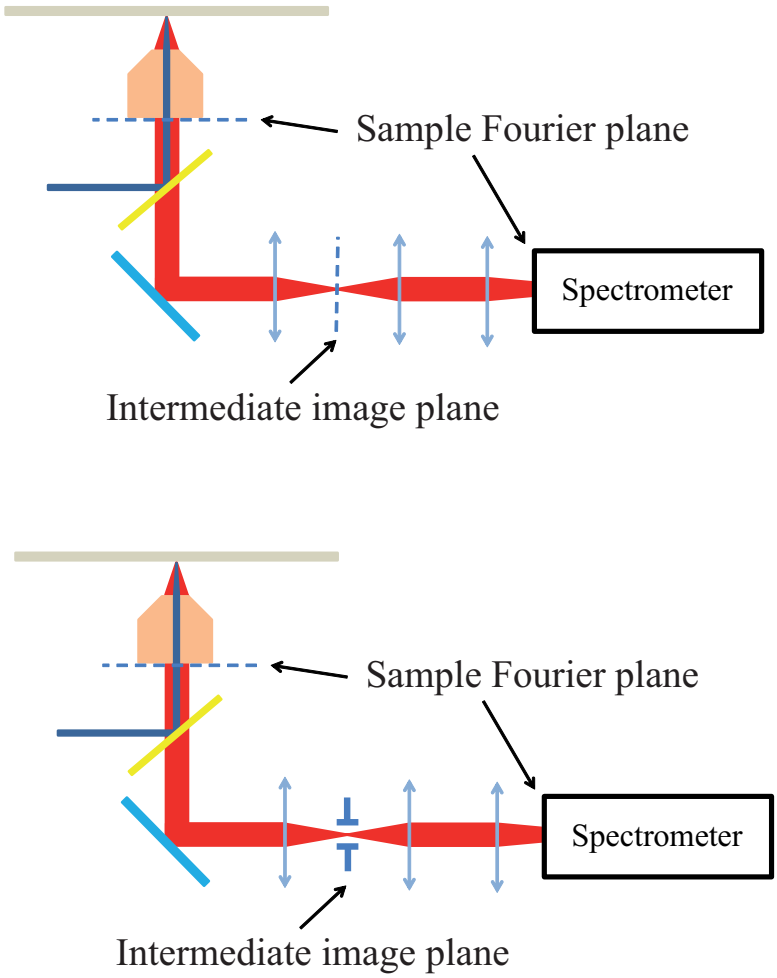

Figure 2.21: Top: Experimental configuration for measuring the emission dispersion relation from the entire sample. Bottom: Experimental configuration for measuring spatially resolved emission dispersion relation from the sample.

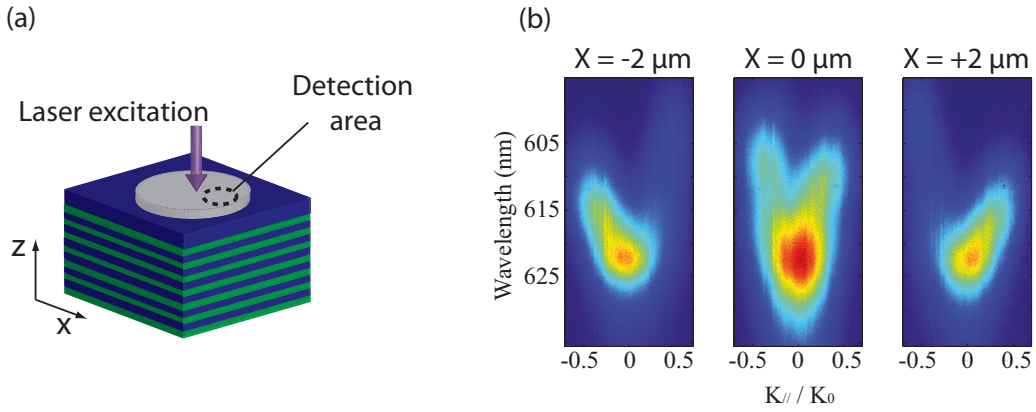

Figure 2.22: (a) Schematic of experimental principle, the laser excitation is centered with respect to the silver disk, the emission is spatially selected by the pinhole; (b) Measured emission dispersion relation from different portion of the disk.

2.5.3 Finite elements simulation

In order to explain qualitatively this observation, we perform numerical simulation of the electric field distribution (fig. 2.23). For the present problem, we use a 2D structure (as shown in Figure 2.23, no variance alone Z axis in the 2D structure simulations) in order to avoid massive calculation time. The simulated structure is as mentioned in the previous section. The 0D-Tamm structure is excited by the nanocrystals which were under laser excitation, at the center of the disk : they were described by 10 electric dipoles along the X axis in the Tamm structure between X = -500 nm and + 500 nm positions with their oscillation strength decreasing with $|X|$ as a Gaussian of standard deviation 1 μm (considering that the laser spot has a diameter of around $1\mu m$ and the spatial intensity distribution is approximated by a gaussian function). The entire structure is surrounded by PMLs to avoid the pertubation from reflection on the boundary. In order to take into account the spectral shift between experiment and simulation due to fabrication defects, we describe the emission frequency by the energy difference $\Delta E = E - E(K_x = 0)$, between the emission energy E and the fundamental $E(K_x = 0)$ which is 652 nm = 1.90 eV for the simulation and 625 nm = 1.98 eV for the experiment.

The figure shows the distribution of E_x. The confined mode is observed under the metallic disk, with one lobe for the $\Delta E = 0$ case and three lobes for the $\Delta E = 8$ meV case. The wavefront of the emitted propagating field is also observed above the disk. For $\Delta E = 0$, the emission is at 0°. For $\Delta E = 8$ meV, the emission from the center of the disk is at 0°, while the

Figure 2.23: Simulated wave front for Tamm mode at $\Delta E = 0$ and $\Delta E = 8\,\text{meV}$. The cell dimensions are $2\mu m$ for Y and $10.2\mu m$ for X.

emission from the right part of the disk goes to the right (positive K_x) and the emission from the left part of the disk goes to the left (negative K_x).

The simulated electric field emission wavefront is thus qualitatively in agreement with the experimental observation, with the right portion of the disk emitting to the right and the left portion emitting to the left.

2.5.4 Comparaison of results from simulation and measurement

For further quantitative analysis, figure 2.24 (a) shows the measured and simulated radiation patterns at ΔE = 8.5 meV and 25 meV, for different values of X. The simulated and measured patterns are in overall good agreement. For both cases, the intensity of emission is maximal when the detected area is at the center of the disk, and decreases as the detected area is moved away from the center, due to the finite extension of the Tamm state. As described previously, the emission from the center of the disk is directed at $K_x = 0$, whereas when the detected area is at position $X < 0$ (resp. $X > 0$), the emission pattern is centered on $K_x < 0$ (resp. $K_x > 0$). For $\Delta E = 25meV$, a smaller lobe is observed on the side of the $|X| = 2\mu m$ emission patterns and well reproduced by theory. This secondary side-lobe might be attributed to diffraction effects, as described by the Airy function for a diffracting slit. For the simulated main lobe, the width at half maximum is 22° and can be assigned mostly to the diffraction angle (as we calculated previously a value $\frac{0.61\lambda}{R} = 0.45rad$). The emission lobes are angularly broader for the experimental case, which we attribute to the lower quality factor of the experimental Tamm states.

Figure 2.16(b) plots the measured and simulated relation between the mode K_x wavevector (center of the emission lobe) and the detected area position X, for different emission energies.

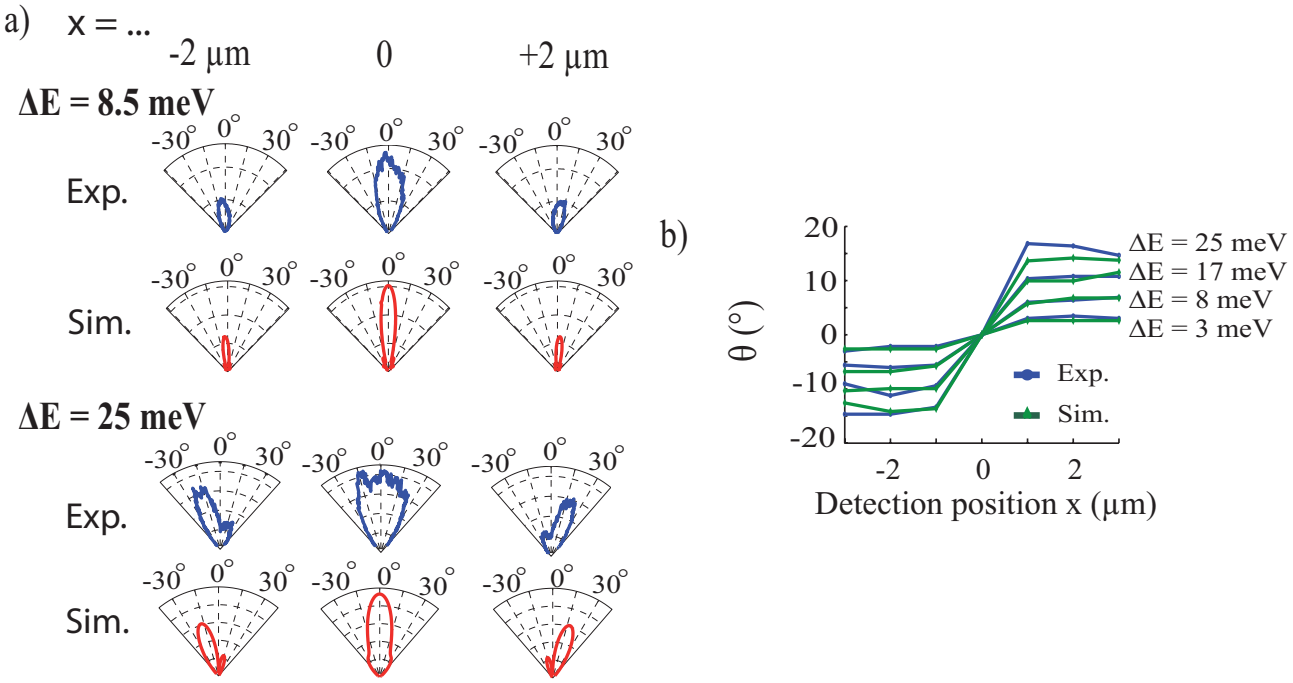

Figure 2.24: (a) Simulated and measured emission pattern of a Tamm 0D cavity($10\mu m$) disk with respect to different pinhole position and ΔE at two different resonance energies Δ E = 8.5 meV and Δ E = 25 meV (b) Simulated and measured emission angle(the angle to which most emission goes) for four different resonance energies Δ E = 3 meV, Δ E = 8 meV, Δ E = 17 meV and Δ E = 25 meV

The simulation and experiment are in excellent agreement. On each side of the disk center, the emission direction shows little dependence on the position : $|K_x|$ is a constant as a function of $|x|$ (for $|X| > 0$). The value of K_x changes as a function of ΔE, in a manner which is given by the 2D-Tamm dispersion relation $\Delta(K_x)$ and well reproduced by theory.

In order to further understand the present experiment, we also plot on figure 2.25 the distribution of the complex electric field modulus and phase $(image(E_x)/real(E_x))$. The modulus distribution shows how the 0D-Tamm state electric field is localized under the disk with some leakage (radiation) to the top. The phase distribution, on the other hand, shows the direction of propagation of the electromagnetic energy. From figure 2.25 (a) we see that, for $\Delta E = 0$, the wavefront is almost horizontal (K_x close to 0), while for $\Delta E = 8\,\text{meV}$ the wavefront shows the symmetric shape described before. Below the disk, where the 0D-Tamm is localized, there is a slight phase gradient : it is this phase gradient which is probed by our experiment.

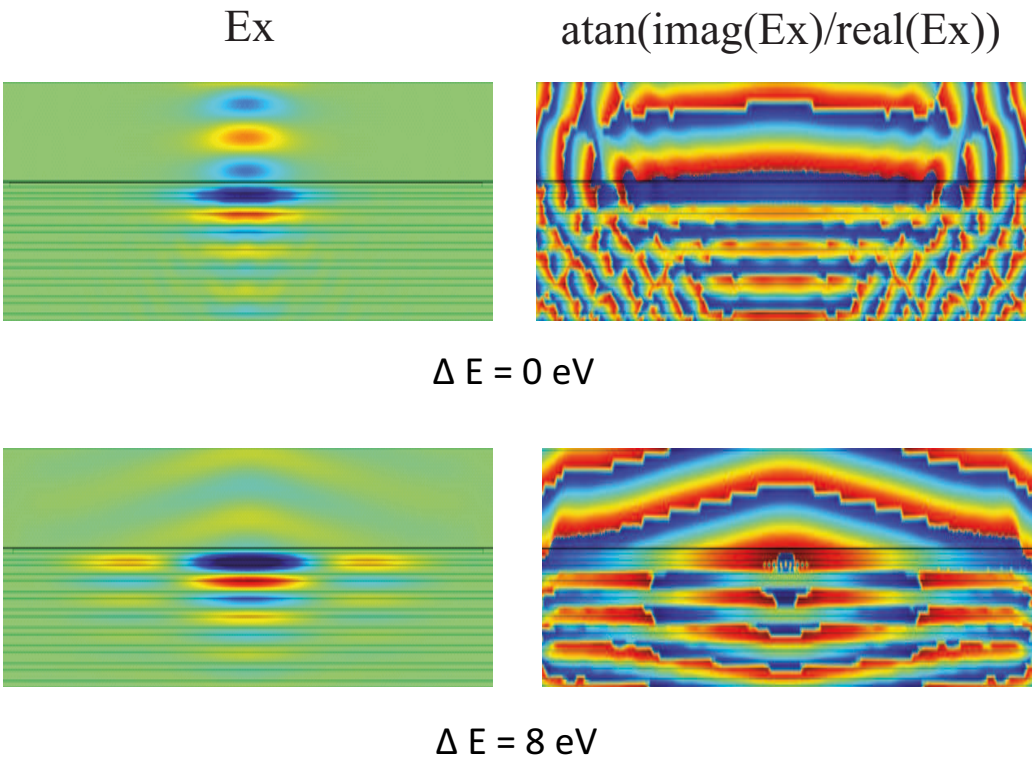

Figure 2.25: Left: electric-field E_x distribution of Tamm 0D cavity($10\mu m$) disk of resonance at $\Delta E = 0$ and $\Delta E = 8\,\text{meV}$. Right: Electric field phase atan(imag(E_x)/real(E_x)) distribution in the Tamm structure.

2.6 Emission radiation pattern as a function of the emitters position below the disk

In the previous section, we demonstrated that, the emission from a Tamm structure is not uniform (different portions of the structure, selected by a pinhole, give different emission patterns) when the excitation laser is centered with respect to the silver disk.

In this section, the emission radiation pattern of the *whole* structure (no pinhole) will be discussed experimentally and theoretically with respect to the emitters position inside the Tamm structure, suggesting the possibility of controlling the emission radiation direction by controlling the position of the emitter. The measured datas and simulated results show good qualitative agreements.

2.6.1 State of art on emission pattern control inside nanophotonic structures

Controlling the emission properties of nanoemitters by changing their optical environment is a widely discussed topic. The radiation pattern of one nanoemitter has been sucessfully concentrated into a cone of $\pm 20 - 30°$ around the optical axis by coupling the emitter to photonic crystal structures [15–18]. It has also been demonstrated that metallic plasmonic gratings [19] and plasmonic nano-antennas such as Yagi-Uda antenna [20] or patch antennas [21] and many other plasmonic antennas [22] [23] [24] are also candidates for controlling the emission pattern from nanoemitters. However, the position of the emitter has a strong influence on the radiation pattern, and its control can be challenging, especially in the case of nano-antennas which have very small mode volumes. For instance, the influence of the excitation position on the radiation has been demonstrated for 200-nm disk antennas, but they were excited by cathodoluminescence, which provided the necessary spatial resolution [25].

Recent breakthrough on nanofabrication technologies make it possible to couple the nanoemitters to nanophotonics structures with deterministic positionning. In particular, it was shown at LPN by A. Dousse, P. Senellart et al. [11] that the far field in-situ lithography technique allows to position a pillar microcavity centered on a quantum dot emitter with 50 nm precision. Our group developed in collaboration with P. Senellart different techniques to posi-

tion a single colloidal CdSe/CdS into a plasmonic patch-antenna (during the thesis of Cherif Belacel and Amit Raj Dhawan), the main idea of the technique is shown in Figure 2.26. By adapting this new developped technique, it would be possible to couple a colloidal CdSe/CdS nanoemitter to optical Tamm structure with different emitter position with respect to the silver disk.

For the following sections, we still consider a layer of CdSe/CdS nanocrystals inside an optical Tamm structure. By changing the laser excitation position on the silver disk, it is possible to excite different emitters at different positions inside the structure and to determine the effects introduced by the position of the emitter which excites the Tamm structure. Let us point out that, as we select by laser excitation some emitters among a layer of emitters, the spatial resolution of the excitation is limited by the laser spot size (which is limited by the diffraction). Later, by coupling a single emitter to different position in the structure, a sub-wavelength spatial response of the emission to excitation position could be investigated.

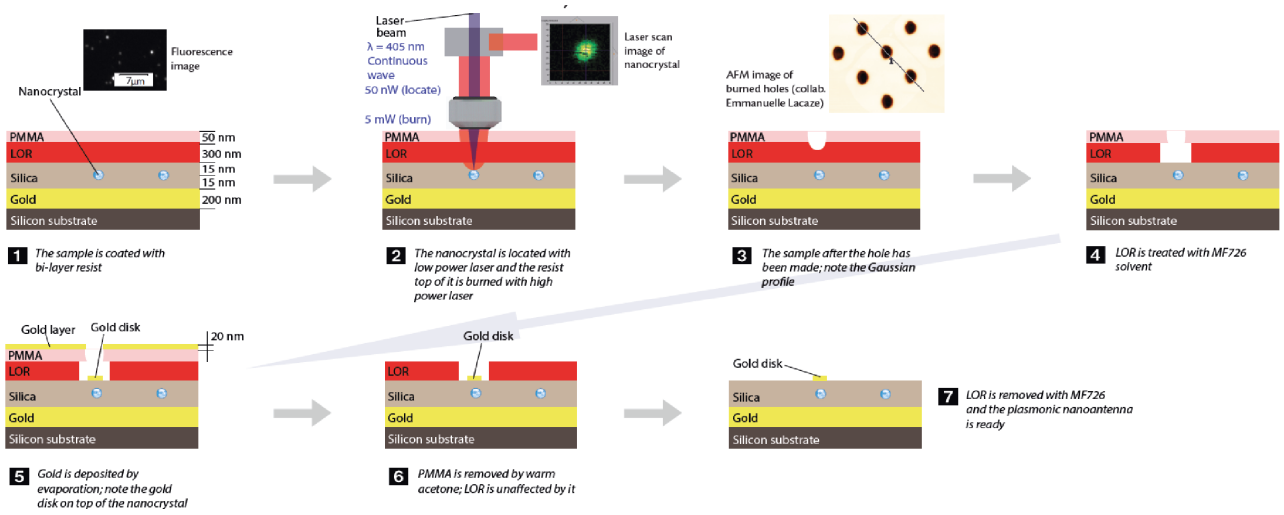

Figure 2.26: Schematic presentation of in situ lithography technique for colloidal nanocrystal at visible range (technique developped during the thesis of Cherif Belacel and Amit Raj Dhawan) [26]

2.6.2 Sample fabrication

For this chapter, a new sample of 0D-Tamm structures with similar parameters is fabricated. The Bragg Mirror is composed by TiO_2/SiO_2 (manufacturer : Kerdry), the estimated optical index for SiO_2 is 1.44, for TiO_2 is 2.25 and we consider that PMMA has the same optic index as

SiO_2. The structure and fabrication details are as follows: 6 pairs of TiO2/SiO2 are deposited on the Si substrate with the center wave length at 640 nm, the material in contact with the substrate is TiO_2, and the layer on top is SiO_2 with a thickness of 80 nm. Figure 2.27 a) shows the reflectivity spectrum of the obtained Bragg Mirror. The stop band of this Bragg mirror is between 580nm and 760nm. The maximum reflectivity is close to 98%. With this sample, the factor quality of the Tamm structure should be around 200 from the transfert matrix simulations.

A layer of colloidal nanocrystals CdSe/CdS is then deposited on this Bragg mirror with an estimated density of $6000/\mu m^2$. It is then necessary to spin coat a layer of PMMA on top of the nanocrystals to protect them. In order to determine precisely the thickness of the deposited PMMA, we proceed as follows. The sample is then cut into two pieces. We add 45 nm of silver on top of one piece and measure the reflectivity spectrum to estimate the thickness of PMMA added. We find λ_{Tamm} around 560 nm so the estimated thickness of PMMA is around 55 nm. Then on the second part of sample another layer of 60 nm of SiO_2 is added to match the cavity resonance wavelength with the emission wavelength of the nanocrystals. Standard optical lithography is then performed to make disks with diameters 2 to 10 μm. A layer of 45 nm silver is deposited on top and covered by around 50 nm of PMMA. As explained for the previous sample, the photo resist is left there (no lift-off is performed). Its thickness was around 300 - 400 nm. The simulated dispersion relation of a 2D Tamm structure with the materials and thicknesses mentioned above is shown in Figure 2.27 b).

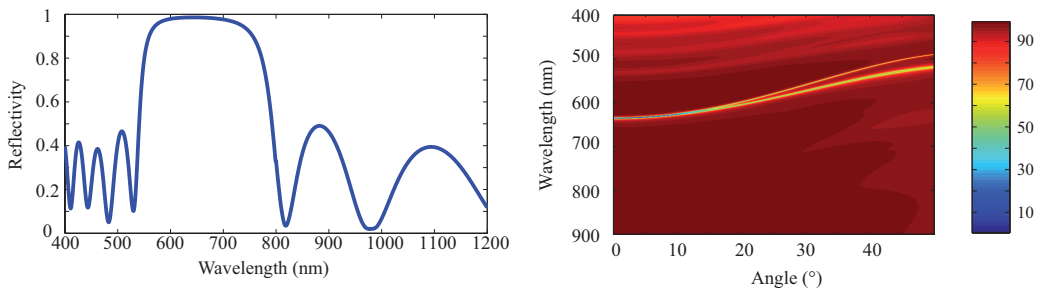

Figure 2.27: a) Measured reflectivity of the Bragg mirror used for this sample. b) Simulated dispersion relation of the fabricated 2D Tamm structure.

2.6.3 Finite elements simulations

Let us first give a theoretical description of the 0D-Tamm structures radiation pattern. We perform 2D simulations, as explained in the previous sections, as it will provide adequate qualitative modeling with limited calculation times. Figure 2.28 shows the simulated dispersion relation for different source dipole positions from 100 nm to 1 μm, in the case of a 4-μm width of the metallic structure (for which there is a clear separation of the discrete Tamm states). The colored dashed lines highlight the emission energies of the different modes. Some interesting points can be seen from these figures :

- Depending on the position of the emitter, different modes will be excited. For an emitter at the center, modes 1,3 and 5 are excited, while modes 2 and 4 are not excited for parity reasons. For an emitter located 500 nm from the axis, a mixture of mode 1 and 2 seems to be excited as well as mode 4. For an emitter at 900 nm, mode 5 can be excited.

- Once the emitter is not centered, the emission dispersion relation looses its symmetry. When the emitter is at X negative, most of the emission pattern is at positive angles.

Now we focus on the fundamental mode (the mode at 1.898 eV). The emission pattern at this energy with respect to the emitter position is shown in Figure 2.29 a) When the emitter gets further from the center, the emission pattern at 1.898eV goes off axis and to higher angles. The relation between the emitter position and the emission angle (angle at which intensity is maximum) is plotted at Figure 2.29 b). This curve shows a continuous increase of the emission angle up to 5.5°. Figure 2.29 c) shows the relation between emission angle and the emitter position for a 10 μm width. It shows a qualitatively similar but weaker behavior as with the 4 μm width.

When the excitation (emitter position in case of simulation) is not centered with respect to the Tamm structure, different modes can be excited more or less efficiently. The excited Tamm state is thus a sum of different modes with different ratios and phases between them, depending on the excitation position, leading to a different radiation pattern.

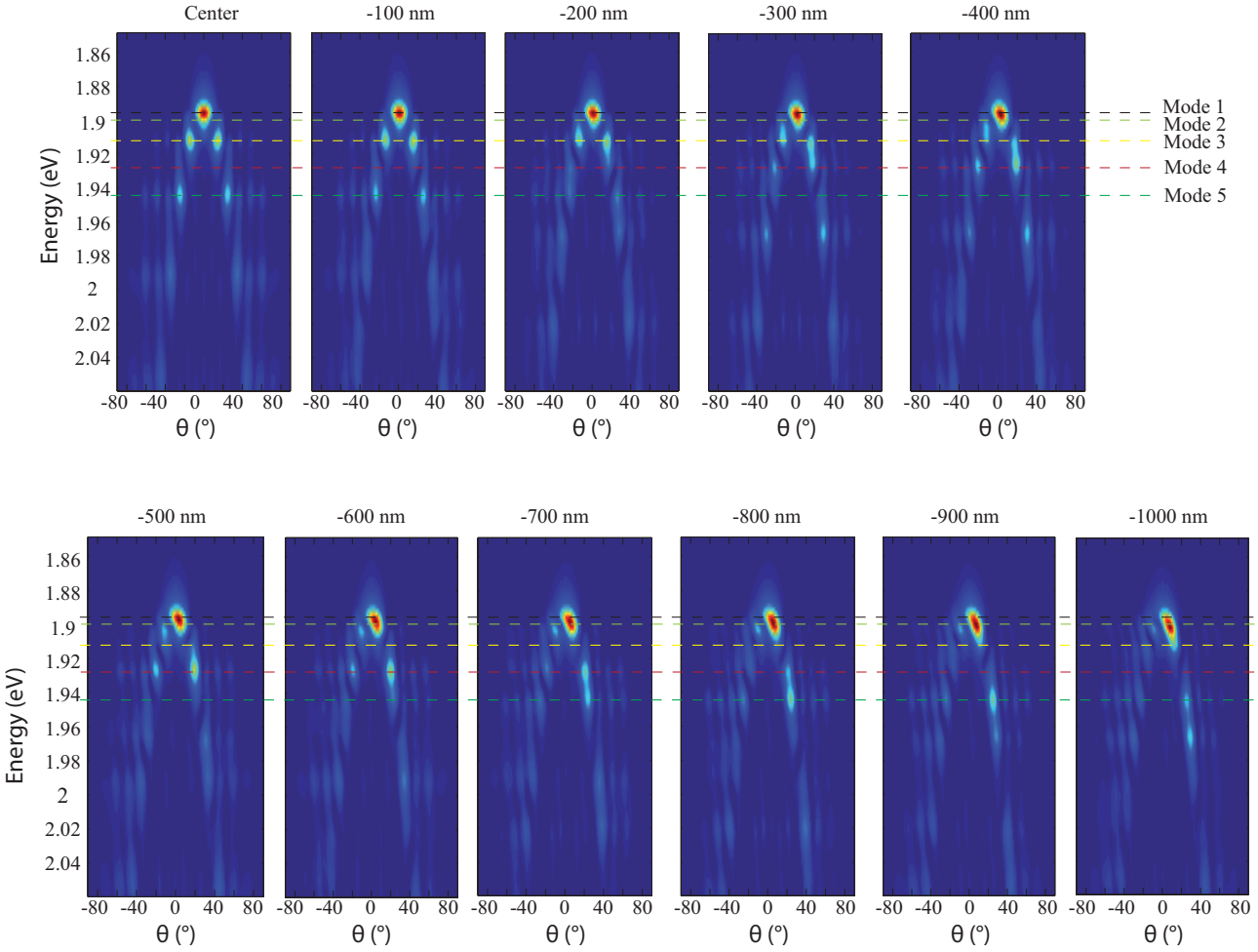

Figure 2.28: Dispersion relation of the emission of one dipole emitter oriented along x direction at different positions under the disk.

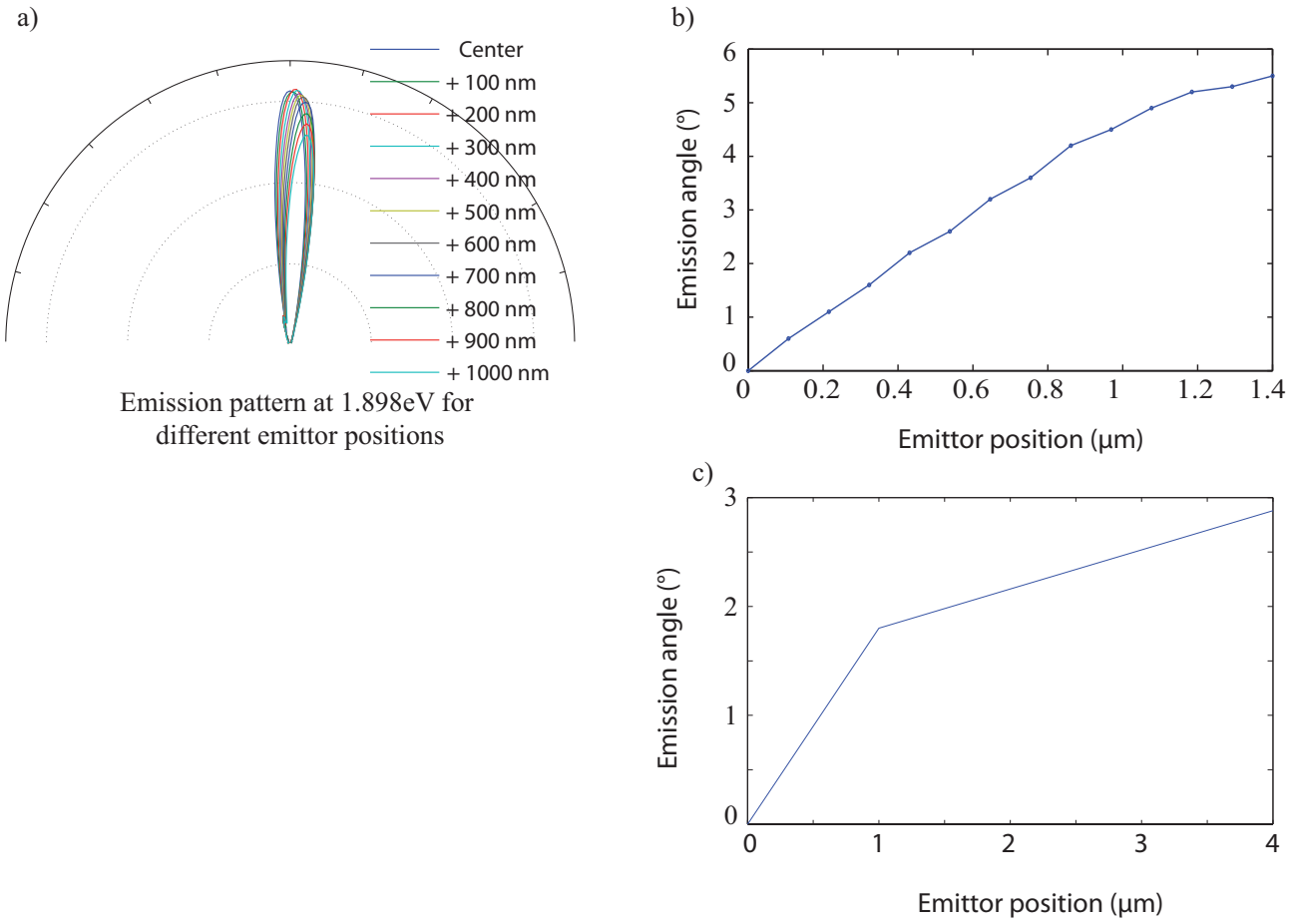

Figure 2.29: a) Emission pattern of the fundamental mode with a $4\mu m$ width of the metallic structure. b) Emission angle of the fundamental mode with respect to different emittor positions for the 4-μm width, and (c) for the 10-μm width.

2.6.4 Experimental measurement

We move the laser spot with respect to the disk, and collect the emission from the entire disk (no pinhole) to analyze the Fourier plane image together with the spectral behavior (like shown in Figure 2.30). Note that the laser spot does not have an infinitely small size, so what we excite an incoherent sum of single dipoles spread over an extension of around 1μm (estimated laser spot size).

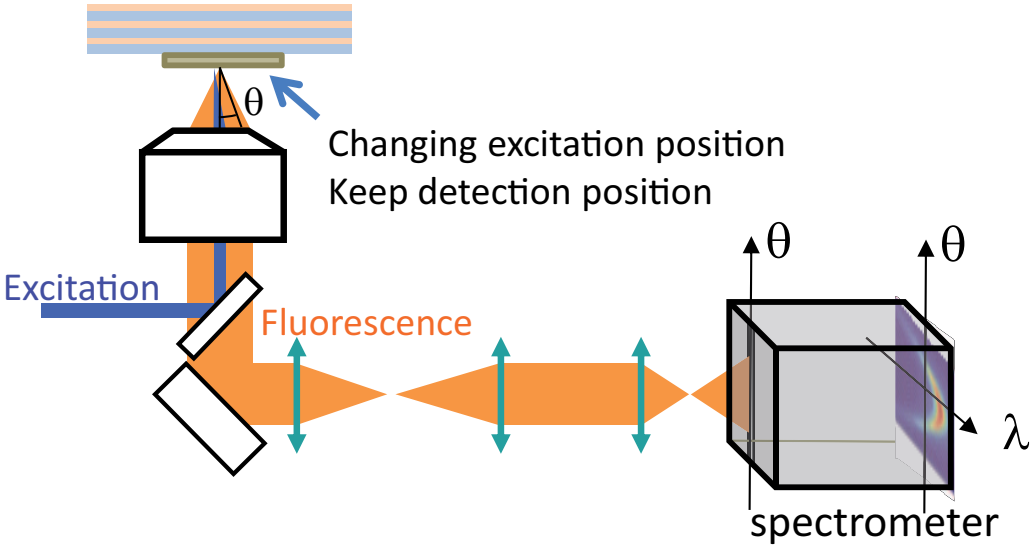

Figure 2.30: Experiment configuration for measuring the emission dispersion relation from Tamm structure with respect of laser excitation poisition

Figure 2.31, corresponding to the 10-μm disk, shows the same behavior as the simulation : when the excitation point moves towards $X > 0$, the emission pattern has more components at $K_x < 0$; when the excitation point move towards $X < 0$, the emission pattern has more components at $K_x > 0$. When the excitation is at $+2\ \mu m$ or $+3\ \mu m$, different modes are excited. Note that we can evidence a quantization of the $10\mu m$ cavity modes, which was not visible from the $X = 0$ case. The separation between discrete modes is however not as clear as in the simulation, due to the larger size of the experimental excitation spot.

Figure 2.32 shows the case **when the disk is 4 μm as diameter**. We limit ourselves to off-axis shifts of 0.5 and 1 μm as getting closer to the disk limit would increase the (already strong) photoresist contribution. The qualitative behavior is the same as in the previous experimental and simulated results, with some differences between the $+X$ and $-X$ measured patterns because of position imperfections, slight sample drifts or inhomogeneities of the dense

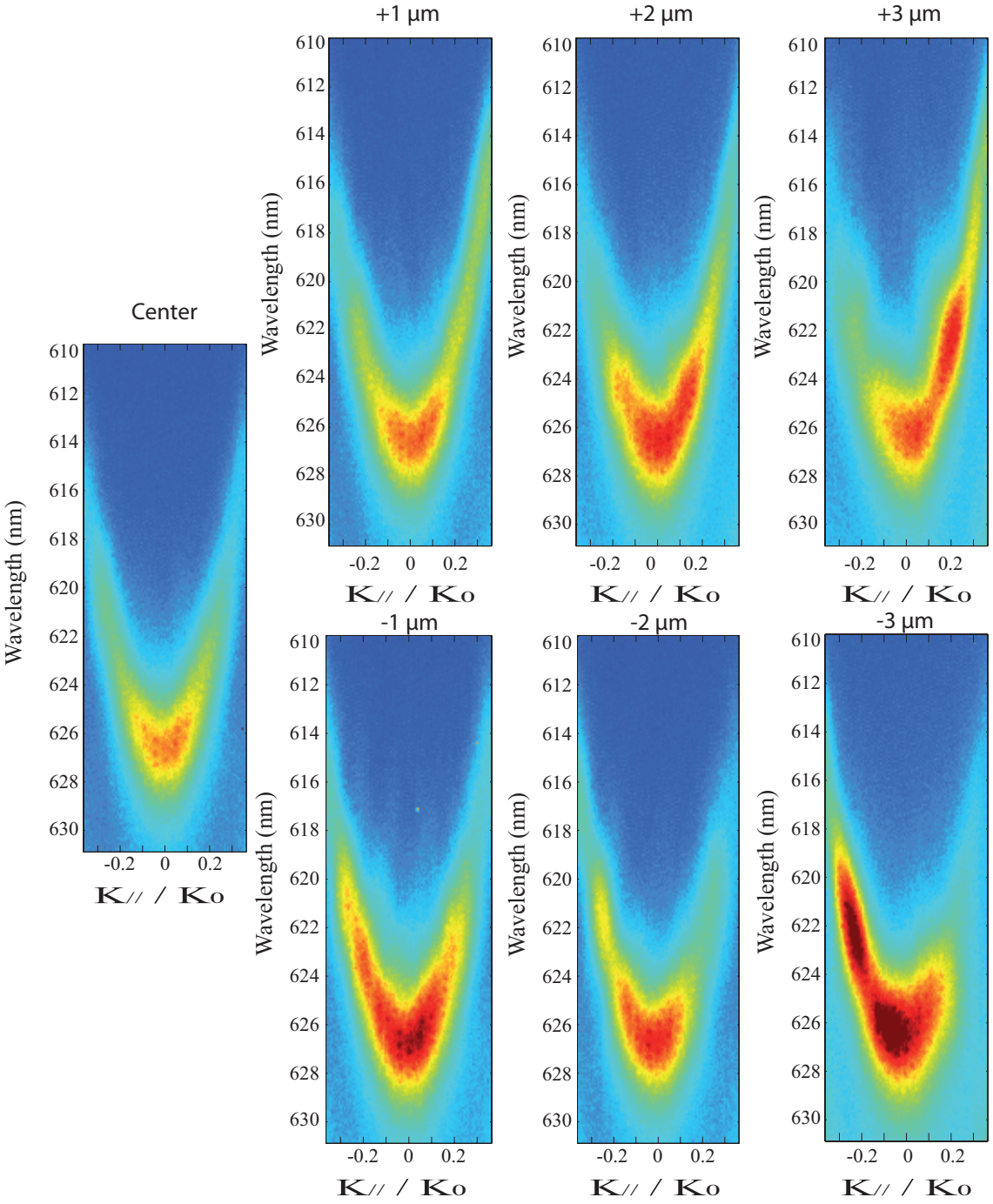

Figure 2.31: Measured emission pattern from a 10μm disk with respect to the laser excitation position

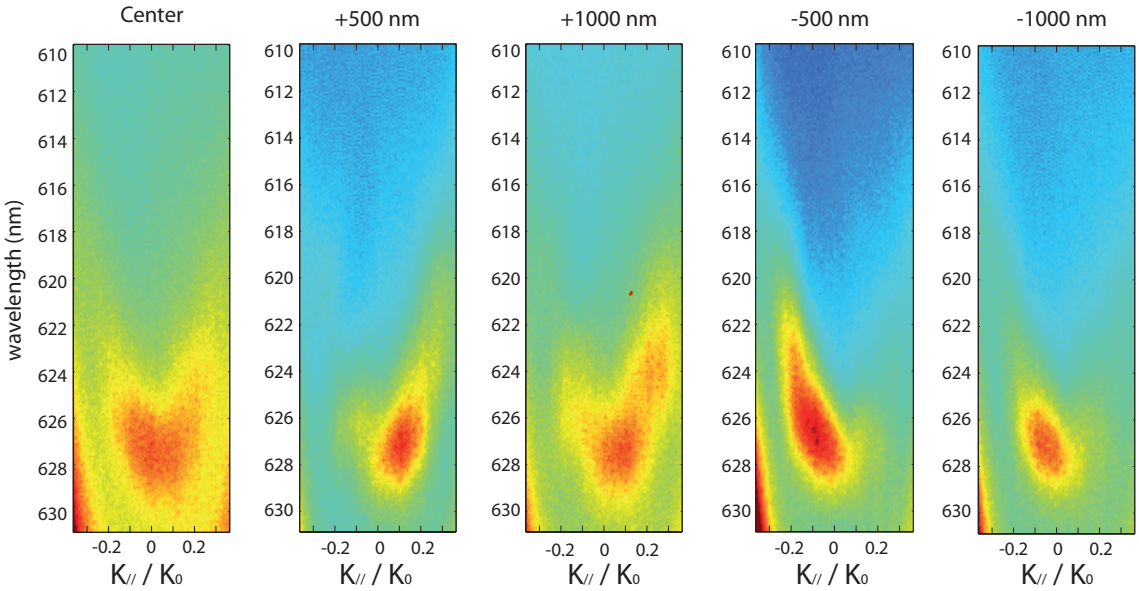

Figure 2.32: Measured emission pattern from a 4μm disk with respect to laser excitation position

nanocrystals layer.

We now study the measured emission pattern from the 10-μm and 4-μm disks. We plot the **radiation pattern for two given wavelengths**, at the fundamental and at the next discrete energy state. We limit the plot to the lower angles corresponding to the Tamm states excited by the nanocrystals beneath ; at higher angles, a strong contribution from photoresist around the disk may appear, as seen clearly on fig.2.32.

Figure 2.33 shows the measured emission pattern **from a 10μm disk**. For the fundamental mode, the emission pattern moves by a few degrees with the excitation position. At $\pm$ 3 μm, the angular shift is 4.6°, which is the same order as the value 5.5° in the 2D simulation. For the mode at 622 nm ($\Delta E = 16.5$ meV above the fundamental), we see a significant modification for the emission pattern with respect to the excitation position. When the emission is centered, the emission pattern has two symmetric peaks. When the excitation is at $X > 0$, the emission angle of these two peaks does not change but the peak at $\theta < 0$ becomes more and more important, while for $X < 0$, the peak at $\theta > 0$ is more important. Changing the excitation position thus provides a way, here, to modulate the emission either forwards or backwards along the x direction.

For a more quantitative comparison between experiment and theory, Jean-Paul Hugonin at

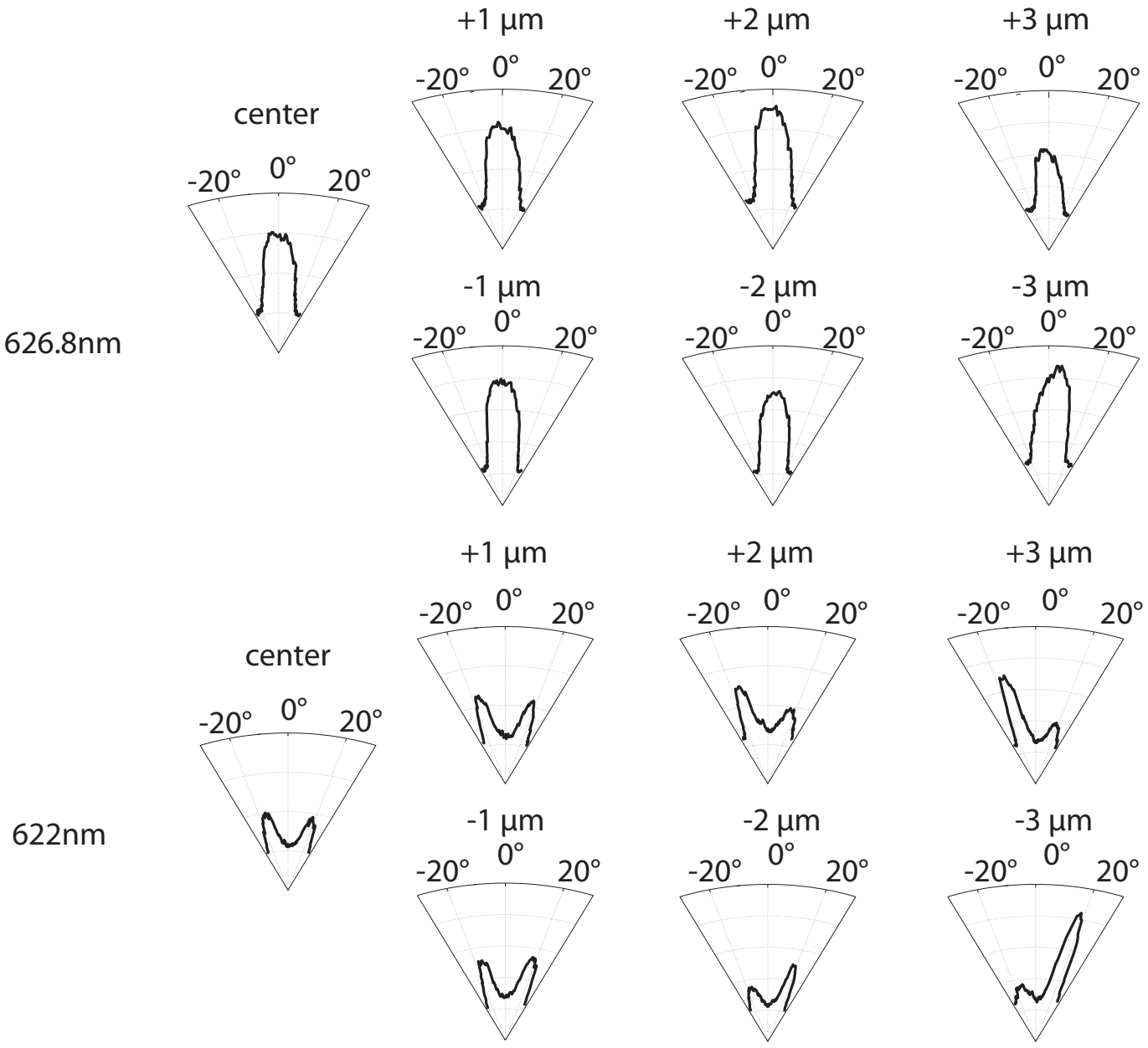

Figure 2.33: Measured emission pattern from a 10μm disk with respect to laser excitation position at 626.8nm(fundamental mode) and 622nm

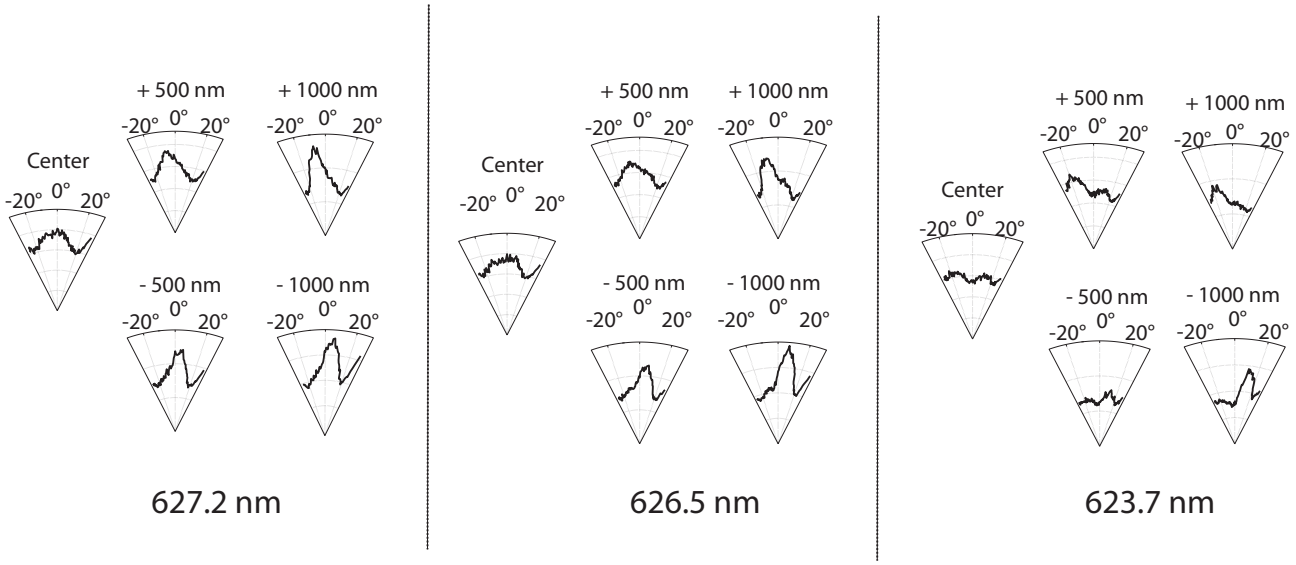

Figure 2.34: Measured emission pattern from a 4μm disk with respect to laser excitation position at 627.2nm(fundamental mode), 626.5nm and 623.7nm

the Institut d'Optique Graduate School (IOGS) performed exact 3D simulations of the Tamm structure with a 10-μm disk [27]. Figure 2.35 shows the obtained radiation pattern for various source-dipole positions and orientations (the case of a z-oriented dipole is not shown as it leads to much weaker emission), for an emission at $\Delta E = 16.5$ meV from the fundamental. As the emitter is moved along the x axis into the $+x$ direction, a clear asymmetry of the emission pattern appears, with more emission into the $-x$ direction. However, to this general tendency are added more complex variations of the pattern lobes, related to resonances inside the Tamm structure.

Figure 2.36 (a) plots the simulated ratio of emission along the $+x$ direction (at $\phi = 0$) divided by the emission along the $-x$ direction. For the two dipole orientation x and y, this ratio can be compared with the ratio between the two lobes of the experimental radiation pattern plotted at 622 nm ($\Delta E = 16.5$ meV) which is shown in Figure 2.36 (b). The experimental values are well reproduced by the results of the 3D simulation.

Figure 2.34 shows the emission pattern of the confined Tamm cavity **with a 4 μm disk**. Note that, as the disk is smaller, we collect more emission from the photo resist outside the disk which disturbs the measurement (the peak appearing at the right edge of the emission pattern is the signal from the photo resist). A behavior similar to the 10 μm disk is observed, with much stronger contribution from the surrounding photoresist.

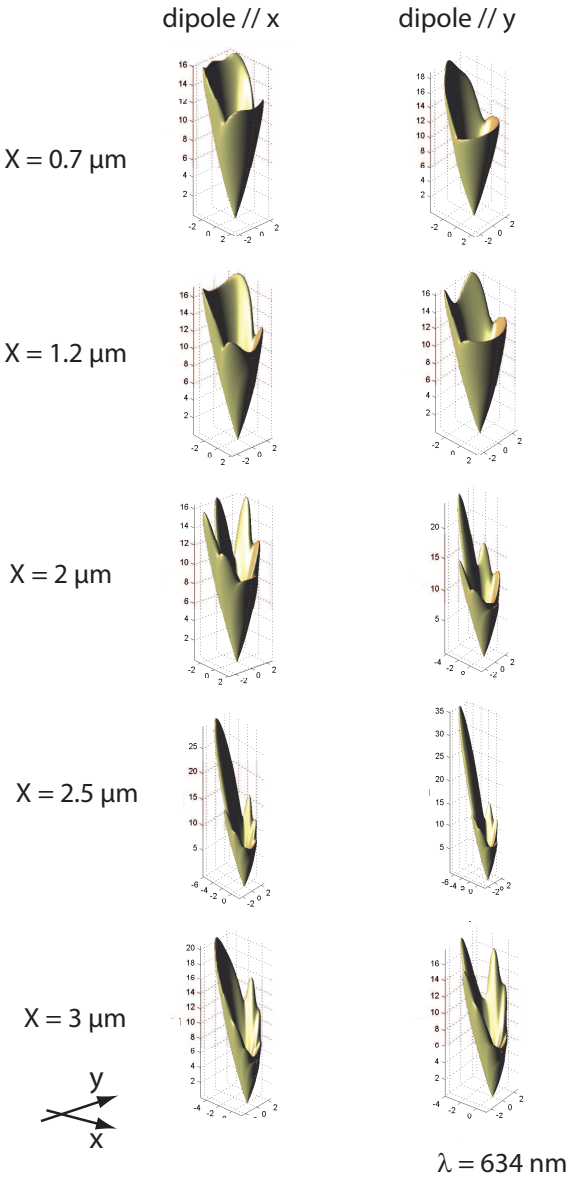

Figure 2.35: Simulated emission with 3D Tamm structure at $\Delta E = 16.5$ meV with an individual dipole along different directions (x and y)

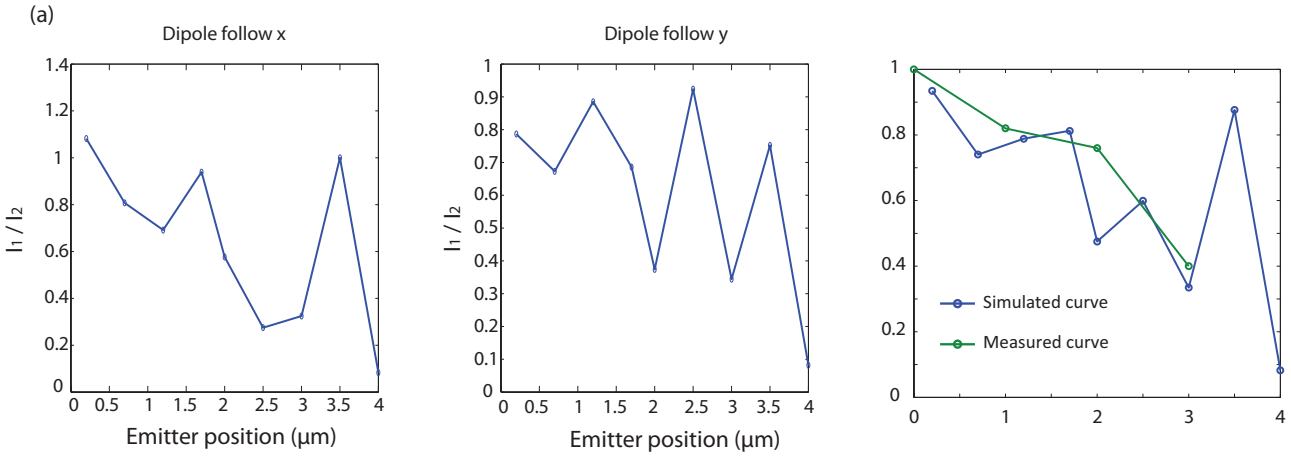

Figure 2.36: (a) Simulated emission intensity ratio for different dipole position and orientation. I_1 is the emission along $+x$ at $\phi = 0$, and I_2 is the emission along $-x$ direction (b) The blue curve is the simulated emission intensity ratio (half contribution from dipole along x and half contribution from dipole along y); The green curve is the measured intensity ratio along $+x$ and $-x$ direction

In conclusion, we have demonstrated in this section the possibility to modify the emission pattern of the Tamm structure by exciting the emitters in different positions. The 2D simulation provides a qualitative description of the measured radiation patterns, and a good quantitative agreement with experiment was obtained for the 3D simulations from the IOGS. The physical reason for this behavior is that by exciting the emitters in different positions under the metallic disk, the different eigenmodes of the structure are excited with different efficiency and phase. Let us point out that, unlike others structures such as the antennas [25], the level of control over the emitters' position need to be only of 0.5 or 1 μm, so that optical methods such as in situ lithography could be used to fabricate structures with manipulation of the emission direction.

Conclusion

Tamm states offer the possibility to create nanophotonic structures with resonances in the visible range and quality factors of a few hundreds, with relatively versatile fabrication methods, including the possibility to create 0D Tamm structures (disk on a Bragg mirror) centered on a single nano-emitter by in-situ photolithography. Experimental realization of single-photon emitters and nano-lasers involving Tamm structures in the near-infrared have already been

reported in the literature. We fabricated 2D and 0D Tamm structures containing a dense layer of colloidal nanocrystals. Photoluminescence emission from these structures demonstrated a dispersion relation characteristic of Tamm states, indicating a good coupling of the nanocrystals with the Tamm states. For disks of 2 to 4 μm, confinement of the 0D Tamm states was evidenced as a discretization and blueshift of the dispersion relation.

By introducing a pinhole in an intermediate image plane, we were able to select a spatial subportion of the metallic disk and analyze its dispersion relation. It was then shown that a portion on the right side of the disk radiates rightwards, while a portion on the left radiates leftwards, in good agreement with our numerical simulations. This original characterization method in fact probes the spatial distribution of the electric-field phase gradient in the Tamm structure, while standard direct imaging of the Tamm disk would only provide the modulus of the electric field. Such characterization could be applied to a wide range of nanophotonic structures. Diffraction is the main limitation to this measurement, as a good spatial resolution is always associated with a low angular resolution.

We further showed that, by exciting different positions on the disk, the Tamm structure radiation pattern could be modified : depending on their position, the nanocrystals, which are excited by the laser, excite a different sum of Tamm states, which radiates in different directions. A large asymmetry between forward and backward emission can be generated, as confirmed by numerical simulations performed at IOGS. By in-situ lithography, it would be possible to fabricate a 0D Tamm structure containing a single nanocrystal, with deterministic control over the position of the nanocrystal of the order of 50 nm. A control of the emission direction of a single-photon source would then be provided. More studies could also be performed on the coupling between a single nanocrystal and a resonant photonic structure, which has seldom been achieved, such as analysis of the role of temperature on the spectral agreement between emitter and Tamm structure.

Bibliography

[1] M. Kaliteevski, I. Iorsh, S. Brand, R. A. Abram, J. M. Chamberlain, A. V. Kavokin, and I. A. Shelykh. Tamm plasmon-polaritons: Possible electromagnetic states at the interface of a metal and a dielectric bragg mirror. *Phys. Rev. B*, 76(16):165415, 2007.

[2] Ritwick Das. Optical tamm mode based refractometer in all-dielectric configuration. *Photonics and Nanostructures - Fundamentals and Applications*, 12(3):252–258, 2014.

[3] Ramachandram Badugua, Emiliano Descrovib, and Joseph R. Lakowicza. Radiative decay engineering 7: Tamm state-coupled emission using a hybrid plasmonicphotonic structure. *Analytical Biochemistry*, 445(3):1 – 13, 2014.

[4] C J R Sheppard. Approximate calculation of the reflection coefficient from a stratified medium. *Pure and Applied Optics: Journal of the European Optical Society Part A*, 4(5):665, 1995.

[5] P. B. Johnson and R. W. Christy. Optical constants of the noble metals. *Phys. Rev. B*, 6(12):4370–4379, 1972.

[6] Ramachandram Badugu and Joseph R. Lakowicz. Tamm state-coupled emission: Effect of probe location and emission wavelength. *The Journal of Physical Chemistry C*, 118(37):21558–21571, 2014.

[7] B. I. Afinogenov, V. O. Bessonov, A. A. Nikulin, and A. A. Fedyanin. Observation of hybrid state of tamm and surface plasmon-polaritons in one-dimensional photonic crystals. *Applied Physics Letters*, 103(6), 2013.

[8] M. Lopez-Garcia, Y.-L. D. Ho, M. P. C. Taverne, L.-F. Chen, M. M. Murshidy, A. P. Edwards, M. Y. Serry, A. M. Adawi, J. G. Rarity, and R. Oulton. Efficient out-coupling

and beaming of tamm optical states via surface plasmon polariton excitation. *Applied Physics Letters*, 104(23), 2014.

[9] O. Gazzano, S. Michaelis de Vasconcellos, K. Gauthron, C. Symonds, J. Bloch, P. Voisin, J. Bellessa, A. Lemaître, and P. Senellart. Evidence for confined Tamm plasmon modes under metallic microdisks and application to the control of spontaneous optical emission. *Phys. Rev. Lett.*, 107(24):247402, 2011.

[10] O. Gazzano, S. Michaelis de Vasconcellos, K. Gauthron, C. Symonds, P. Voisin, J. Bellessa, A. Lematre, and P. Senellart. Single photon source using confined tamm plasmon modes. *Applied Physics Letters*, 100(23), 2012.

[11] A. Dousse, L. Lanco, J. Suffczyński, E. Semenova, A. Miard, A. Lemaître, I. Sagnes, C. Roblin, J. Bloch, and P. Senellart. Controlled light-matter coupling for a single quantum dot embedded in a pillar microcavity using far-field optical lithography. *Phys. Rev. Lett.*, 101(26):267404, 2008.

[12] T. Braun, V. Baumann, O. Iff, S. Hfling, C. Schneider, and M. Kamp. Enhanced single photon emission from positioned InP/GaInP quantum dots coupled to a confined tamm-plasmon mode. *Applied Physics Letters*, 106(4), 2015.

[13] C. Symonds, G. Lheureux, J. P. Hugonin, J. J. Greffet, J. Laverdant, G. Brucoli, A. Lemaitre, P. Senellart, and J. Bellessa. Confined tamm plasmon lasers. *Nano Letters*, 13(7):3179–3184, 2013.

[14] Guillaume Lheureux, Stefano Azzini, Clementine Symonds, Pascale Senellart, Aristide Lematre, Christophe Sauvan, Jean-Paul Hugonin, Jean-Jacques Greffet, and Joel Bellessa. Polarization-controlled confined tamm plasmon lasers. *ACS Photonics*, 2(7):842–848, 2015.

[15] S.-K. Kim S.-H. Kim and Y.H. Lee. Vertical beaming of wavelength-scale photonic crystal resonators. *Phys. Rev. B*, 73(23):235117, 2006.

[16] S. Combrie N.-V.-Q. Tran and A. De Ross. Directive emission from high-q photonic crystal cavities through band folding. *Phys. Rev. B*, 79(4):041101, 2009.

[17] Sylvain Combrié, Nguyen Vi. Tran, and Alfredo De Rossi. Directive emission from high-Q photonic crystal cavities through band folding. *Conference on Lasers and Electro-Optics/International Quantum Electronics Conference*, page CMP2, 2009.

[18] C. Reardon T. F. Krauss L. OFaolain L. C. Andreani S. Portalupi, M. Galli and D. Gerace. Planar photonic crystal cavities with far-field optimization for high coupling efficiency and quality factor. *Opt. Express*, 18(15):16064, 2010.

[19] H. Frederich, F. Wen, J. Laverdant, W. Daney de Marcillac, C. Schwob, L. Coolen, and A. Maitre. Determination of the surface plasmon polariton extraction efficiency from a self-assembled plasmonic crystal. *Plasmonics*, 9(4):917, 2014.

[20] Qi. Wang C. Q. Chen X. H. Liu L. X. Sun Bo. Zhang J. Zi X. W. Yuan, L. Shi and Wei. Lu. Spontaneous emission modulation of colloidal quantum dots via efficient coupling with hybrid plasmonic photonic crystal. *Opt. Express*, 22(19):23473, 2014.

[21] F. Bigourdan F. Marquier J.-P. Hugonin S. Michaelis de Vasconcellos X. Lafosse L. Coolen C. Schwob C. Javaux B. Dubertret J.-J. Greffet P. Senellart C. Belacel, B. Habert and A. Maitre. Controlling spontaneous emission with plasmonic optical patch antennas. *Nano Lett*, 13(4):1516, 2013.

[22] T. H. Taminiau M. P. Kreuzer R. Quidant A. G. Curto, G. Volpe and N. F. van Hulst. Unidirectional emission of a quantum dot coupled to a nanoantenna. *Science*, 329(5994):930–933, 2010.

[23] S. Maeda H. F. Hofmann T. Sugita, K. Yanazawa and Y. Kadoya. Radiation pattern of plasmonic nano-antennas in a homogeneous medium. *Opt. Express*, 22(11):13263, 2014.

[24] T. V. Teperik R. Esteban and J.-J. Greffet. Optical patch antennas for single photon emission using surface plasmon resonances. *Phys. Rev. Lett.*, 104(2):026802, 2010.

[25] Abbas Mohtashami, Toon Coenen, Alessandro Antoncecchi, Albert Polman, and A. Femius Koenderink. Nanoscale excitation mapping of plasmonic patch antennas. *ACS Photonics*, 1(11):1134–1143, 2014.

[26] F. Bigourdan F. Marquier J.-P. Hugonin S. Michaelis de Vasconcellos X. Lafosse L. Coolen C. Schwob C. Javaux B. Dubertret J.-J. Greffet P. Senellart A. Maitre C. Belacel,

B. Habert. Controlling spontaneous emission with plasmonic optical patch antennas. *Nano lett*, 13(4):1516–1521, 2013.

[27] C. Sauvan, J. P. Hugonin, I. S. Maksymov, and P. Lalanne. Theory of the spontaneous optical emission of nanosize photonic and plasmon resonators. *Phys. Rev. Lett.*, 110:237401, 2013.

Chapter 3

Study of dipole nature and orientation of CdSe/CdS colloidal nanoplatelets

Introduction

Understanding the luminescence properties of a nano-emitter and its coupling with the optical environment requires the knowledge of its dipolar nature, as well as of its orientation. Most fluorescent molecules behave as a linear (one-dimensional - 1D) electric dipole [1, 2]. However, for some molecules, the energy levels structure presents two denegerate orthogonal 1D dipoles which contribute together to the emission : the emission is then an incoherent sum of two orthogonal dipoles ; we refer to this case as a two-dimensional (2D) dipole.

As for colloidal semiconductor nanostructures, the 1D or 2D nature seems to depend on its geometry. For dots-in-rods (spherical core with an elongated rod-like shell), experiments indicate a 1D structure [3–6]. Spherical nanocrystals, on the other hand, behave as 2D dipoles [7]. This can be explained by the electron-hole pair fine structure : as calculated by Efros et al. in 1996 [8], the degeneracy between the eight $1S1P_{3/2}$ electron-hole pair states (defined in the first chapter) can be lifted by the wurtzite crystalline structure or by a slightly prolate shape. Emission then originates from an incoherent sum of two $\sigma+$ and $\sigma-$ transitions - which, by a change of basis, can be rewritten as an incoherent sum of two orthogonal linear dipoles. For both spherical and dot-in-rod structures, some observations have suggested the possibility of intermediate states, such as a sum of 1D and 2D dipoles.

Experimental characterization of the 1D or 2D nature of nano-emitters is intricately related with measurement of their orientation, as these two parameters affect together most measured quantities and are difficult to measure independently. Some authors have considered the emission radiation pattern, sometimes through Fourier image as presented in the first chapter, but most often through a defocused imaging [9, 10] of the emitter, which is experimentally more convenient but requires a heavier formalism to be modelled. Other authors have considered the emission polarization. The PhD work of Clotilde Lethiec at INSP has shown that the orientation of a nano-emitter can be obtained through its degree of polarization, provided that its 1D or 2D nature are known, and that the 1D or 2D nature can be obtained by a polarization analysis over a statistics of emitters - assuming that they are identical [11] and references therein for a state of the art on such characterizations and their applications to colloidal semiconductor nanostructures).

In this chapter, we show that the combination of polarization and Fourier analysis of a single emitter (not a collection of identical emitters) can provide both its 1D and 2D dipole nature and its orientation. The possibility of an intermediate case (between 1D and 2D or between 2D and 3D) can also be analyzed. This method relies on the careful choice of the substrate (either gold or glass) and objective (air or oil), in order to create conditions were the 1D and 2D emissions present clearly distinct properties. We apply these methods to the study of high quality colloidal semiconductor nanoplatelets synthesized recently by the group of B. Dubertret (ESPCI).

The first section of this chapter presents the theoretical polarization and radiation pattern for the 1D and 2D case and summarizes the calculation formalism.

The second section presents the nanoplatelets, the measurement setup and a few preliminary characterizations of single platelets.

The third, forth and fifth sections then describe, respectively, the experimental results for the square, rectangular and cubic platelet samples.

3.1 Theoretical modelling of emission polarization and radiation patterns

Let us now present the theoretical result of an experiment of polarization or Fourier plane analysis. The measured quantities depend on the nature (1D or 2D) of the emitting dipole - the emission from the 2D dipole being the incoherent sum of the emission from two 1D dipoles (sum of emitted intensities and not emitted electric fields). They depend also on the orientation of these dipoles as presented in Figure 3.1 : for a 1D dipole, the orientation of the dipole is defined by its zenithal and azimuthal coordinates (Θ, Φ). For a 2D dipole, we describe the orientation by the zenithal and azimuthal coordinates (Θ, Φ) of a "dark" axis which is the axis perpendicular to the plane created by the two orthogonal dipoles.

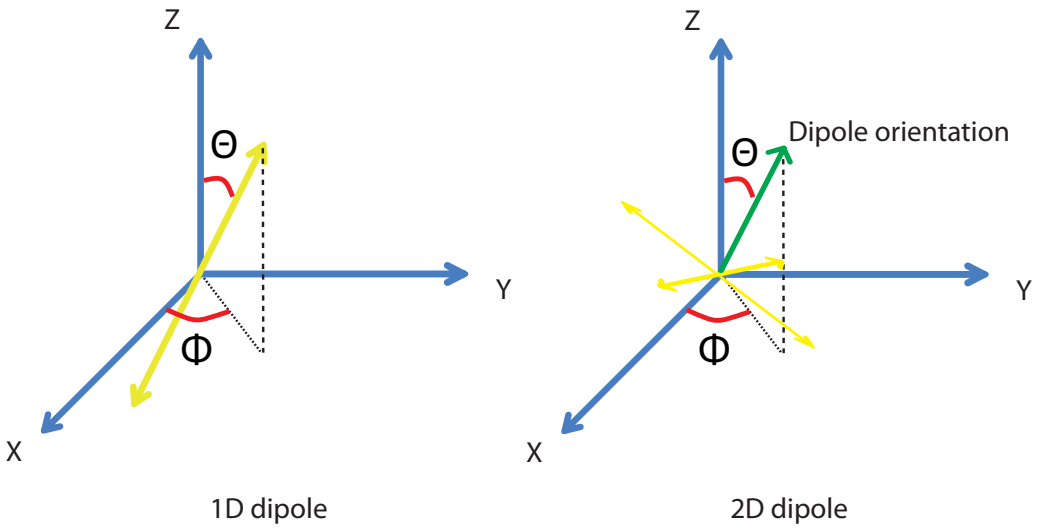

Figure 3.1: Schematic of the structure of a nanoplatelet.

The polarization and radiation pattern of the emission also depend on the environment of the emitter. We describe below an experimental configuration for which, depending on the dipole nature and orientation, different results should be measured.

3.1.1 Polarization for a dipole close to a gold/glass interface

We consider, as shown on figure 3.2, the configuration of a thick layer of gold (more than 100 nm : the thickness can be considered infinite as it is larger than the penetration depth of the

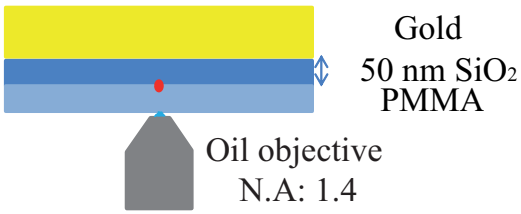

Figure 3.2: Simulated situation : emitter near a planar gold/glass interface.

electromagnetic field at visible wavelengths), covered by 50 nm of SiO_2 as spacer and then the nanoemitters, covered by a PMMA layer of 50 nm. The measurements are performed with an oil objective (of numerical aperture 1.4) so that we can consider that the emitter is in a semi-infinite dielectric medium of index 1.5, at 50 nm from a semi-infinite medium of gold.

An analytical description of the emission polarization can be obtained, as shown in our group during the PhD of Clotilde Lethiec. It shows that the emission intensity along a polarization direction α can be expressed, for a 1D dipole, by the following equation :

$$P(\alpha) = P_{min} + (P_{max} - P_{min}) \cos^2(\Phi - \alpha) \tag{3.1}$$

where

$$P_{min} = Asin^2(\Theta) + Bcos^2(\Theta) \tag{3.2}$$

$$P_{max} - P_{min} = Csin^2(\Theta) \tag{3.3}$$

with A, B, C three constant parameters which only depend on the experimental configuration and the environment around the emitter.

If we define the degree of polarization by :

$$\delta(\theta) = \frac{P_{max} - P_{min}}{P_{max} + P_{min}} \tag{3.4}$$

The calculated degree of polarization (the case of the 2D dipole being deduced by summing two 1D dipoles) is plotted as a function of the dipole orientation in figure 3.3.

Figure 3.3 shows that, if Θ is small (vertical 1D dipole or horizontal 2D dipole), the degree of polarization of emission is small : for $\Theta = 0$, the emission is unpolarized for symmetry reasons. If Θ increases, the degree of polarization increases. For a 1D dipole, in the mentioned configuration of experiment, the degree of polarization δ can reach nearly 100% if the dipole

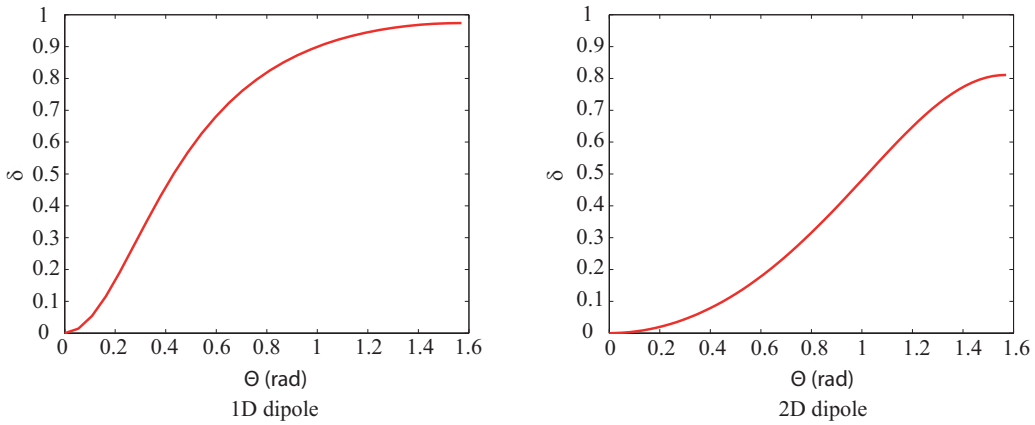

Figure 3.3: Theoretical relation between degree of polarisation and dipole orientation.

is orientated at $\Theta = 90^o$. For a 2D dipole, δ can reach around 80% when dipole is orientated at $\Theta = 90^o$; as expected, the emission from two incoherent dipoles is less polarized than the emission from a single (1D) dipole. Let us note that, for both cases, the emission can never be exactly 100% polarized, as the emitted field has a different polarization depending of the direction of emission, and we detect a sum of the emission into all directions.

Emission pattern for a dipole near a gold/glass interface

The calculation of the emission pattern is based on the calculations by Lukosz [12] [13]. Some simulated results (plotted in the Fourier plane as described in the previous chapter) are shown in Figure 3.4. When the dipole, 1D or 2D, is vertical ($\Theta = 0°$), the emission pattern shows revolution symmetry around the z-axis, while if the dipole is horizontal ($\Theta = 90°$), the emission pattern has an preferred axis. For the case $\Theta = 0°$, there is a clear difference between the 1D dipole case (high emission for higher angles) and the 2D dipole case (high emission at normal direction).

To make a short summary of the polarization behavior and the emission pattern, the emission behavior we expect to have is shown in the Figure 3.5. From the figure, it is clear that, in this experimental configuration, one can distinguish qualitatively whether the emitter behaves as a 1D or 2D dipole. Let us point out that this possibility depends crucially on the experimental conditions : environment (presence of an interface), objective. In the more typical case of the emitters deposited on a glass coverslip and observed by an oil objective, the polarization and radiation pattern are very similar for a vertical 1D or 2D dipole, so we cannot discriminate

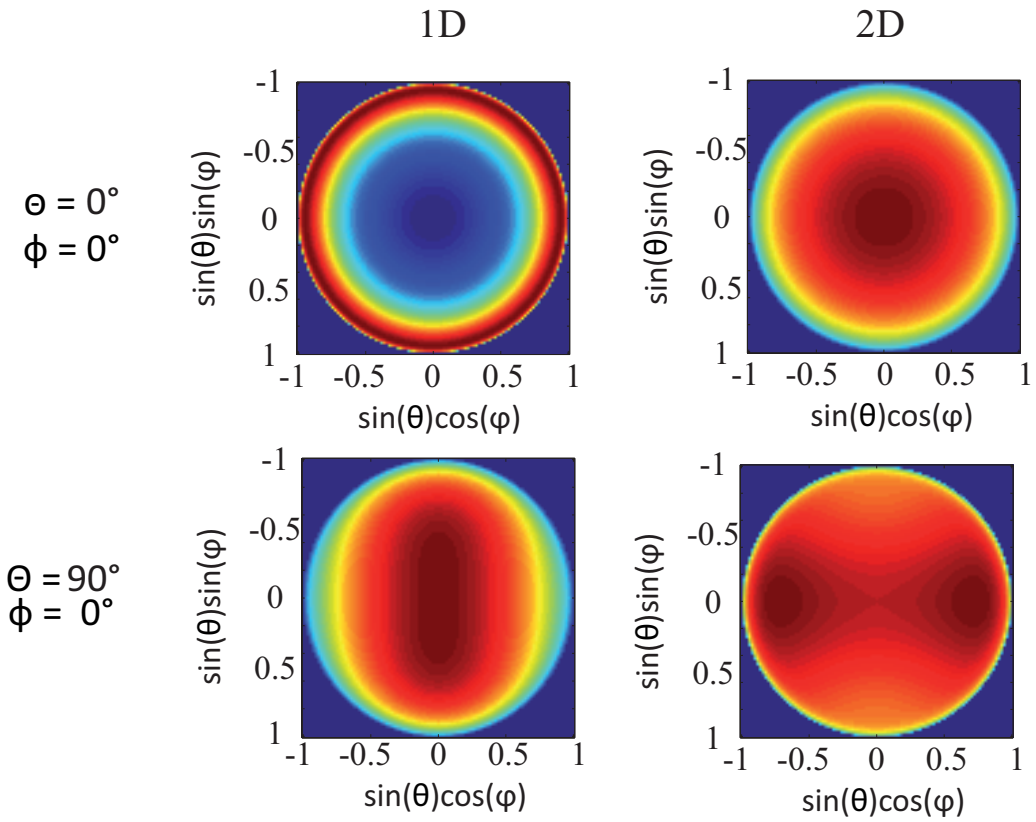

Figure 3.4: Theoretical Fourier plane emission pattern for different dipole types and orientations and angle.

between 1D and 2D dipole in this configuration. We choose this configuration with a gold film in order to create conditions for which the 1D and 2D dipoles can be distinguished.

	1D	2D
$\Theta = 0°$ $\Phi = 0°$	Not polarized Isotropic emission pattern	Not polarized High intensity at center
$\Theta = 90°$ $\Phi = 0°$	Highly polarized High intensity at center and a prefered axis	Highly polarized Low intensity at center and a prefered axis

Figure 3.5: Summary theoretical emission polarization and radiation pattern for different dipole types and orientations.

3.2 Experiment

3.2.1 Nanoplatelet samples

Semiconductor nanoplatelets are a type of colloidal nanostructure, obtained by chemical synthesis, where the control of the reaction parameters leads to a highly anisotropic growth with planar square/rectangular shape. By subsequent growth of another semiconductor with higher bandgap, a core-shell sandwich can be obtained, as shown on fig. 3.6.

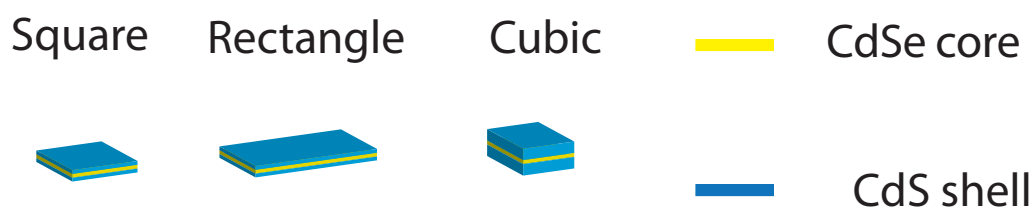

Figure 3.6: Schema of the structure of a nanoplatelet

For this section, the study will consider three different nanoplatelet structures : core-shell squares, rectangles and cubic (thick shell) structures, synthesized in B. Dubertret's group (ES-

PCI). Figure 3.7 are transmission electron microscope images of the square and rectangle structures and their emission and absorption spectra.

These nanoplatelets are composed by CdSe core and CdS shell. For the square platelets the length, width and height are about (15-20 nm) x (15-20 nm) x (1.5-2 nm) respectively, while the rectangle ones are about (15-20 nm) x (7-10 nm) x (1.5-2 nm), and the cubic ones are about (15-20 nm) x (15-20 nm) x (10-15 nm)

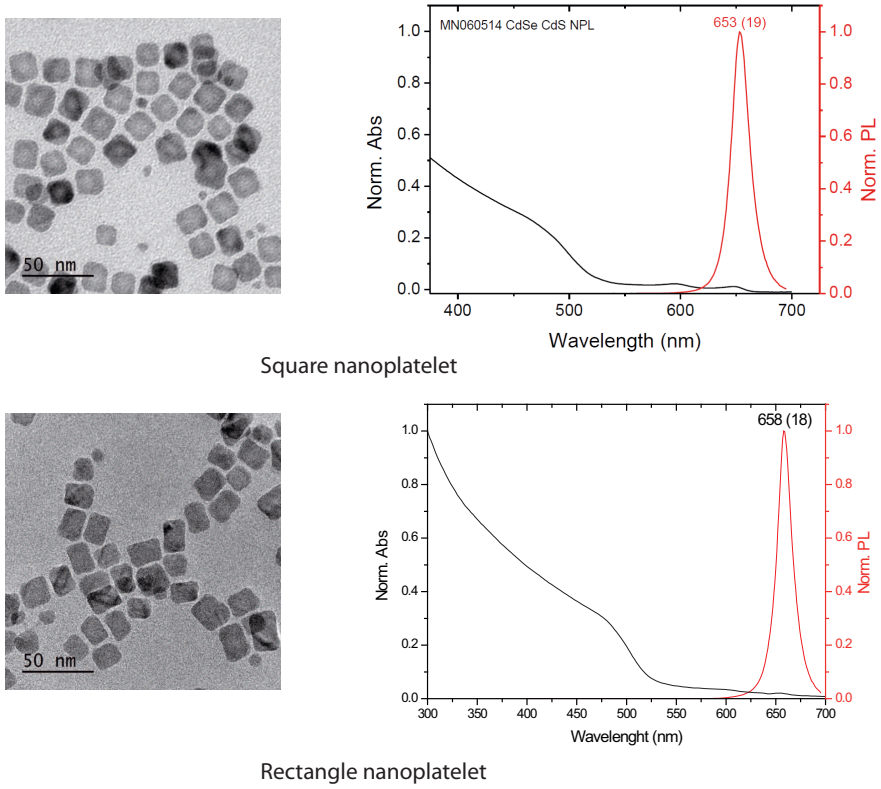

Figure 3.7: TEM image, absorption and emission spectra (in solution) of the square and rectangle nanoplatelets excited by a UV lamp. (Figure from Benoit Dubertret, ESPCI)

Colloidal nanoplatelets display remarkably narrow emission spectrum. For spherical core shell structures, the typical emission bandwidth at room temperature is around 25 nm, while it is below 10 nm for CdSe/CdS nanoplatelets. When studied at the single-particle level, the width of the spectrum is similar compared with the ensemble measurement. This shows that there is very low inhomogenous broadening for the nanoplatelets which proves the excellent control of the chemical synthesis and the low dispersion in the thickness of these nanoplatelets [14].

Time-resolved photoluminescence has also been studied for the nanoplatelets. The CdSe/CdS

platelets show a decay time at around 15-20 ns at room temperature and it decrease to around 200 ps at cryogenic temperature. The photoluminescence intensity increases when decreasing the temperature, and the emission becomes more stable at cryogenic temperature also. This suggests that there is a strong reduction of non-radiative recombination paths [14].

3.2.2 Measurement set-up

The experimental set-up is based on a fluorescence microscope (fig. 3.8). The emitter is centered with respect to the laser spot with the help of a piezoelectric. A pulsed blue laser at 450 nm with a power of 2 μW is reflected by a dichroic mirror with cut off wavelength at 510 nm and focused by an objective with oil immersion with numerical aperature of 1.4. The emission is collected by the same objective. The emitted light then passes through the dichroic mirror and a band-pass filter centered at 632 nm with 94 nm width. Two detection systems are installed on the optical path for polarization analysis and emission pattern measurement.

For the emission pattern measurements, the Fourier Plane (rear focus plane of the objective) of the sample is imaged onto an EMCCD so that the image on EMCCD yields the emission pattern. For the polarization analysis, a motorized $\lambda/2$ plate is inserted in the optical path, the beam will then be separated by a polarized cube beamspliter and sent separately to two photodiodes. By rotating the $\lambda/2$ plate, the emission polarization P(α) can be analyzed. The polarization measurement setup was installed by Clotilde Lethiec during her PhD at INSP (dir. A. Maitre and L. Coolen) and further developed by Nguyen Thu Loan, who is currently doing her PhD research (dir. A. Maitre) in the group and participated in the measurements of this chapter. Precise characterization and correction of the polarization behavior of the microscope setup, as will be developed in her PhD manuscript, shows that polarizing and depolarizing effects, affecting the measurement of the degree of polarization, can be limited to 2-3 %.

The emission pattern measurements and emission polarization analysis were performed on the same nanoplatelets with the same laser excitation power. With these measurements, one can know the emission pattern and emission polarization from a same nanoplatelet.

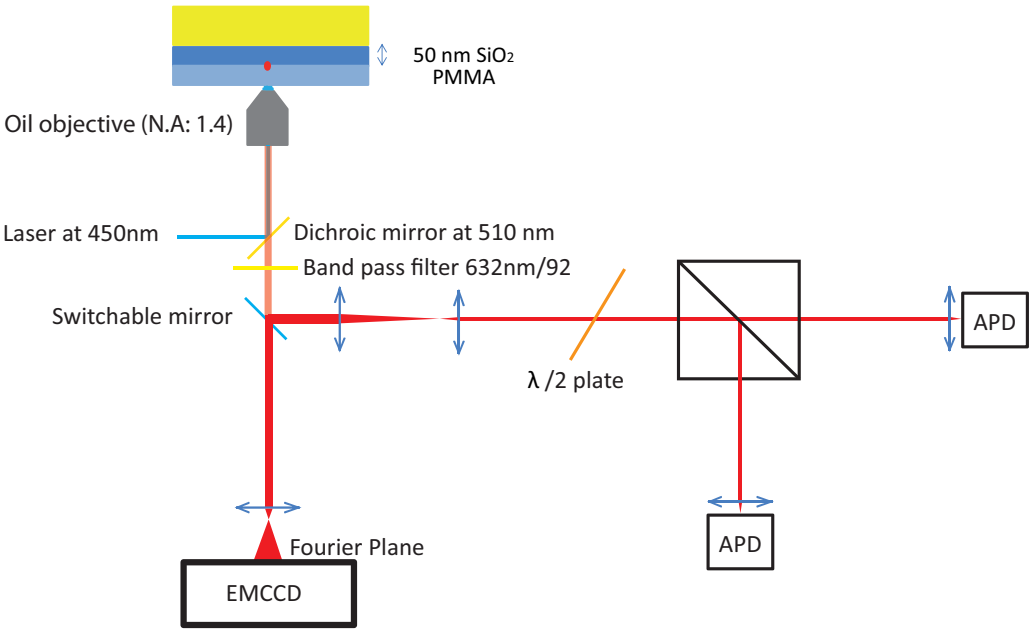

Figure 3.8: Configuration of experiment set-up

3.2.3 Luminescence properties of single square nanoplatelets

We first perform preliminary characterizations of the emission blinking and decay time for the squared nanoplatelets.

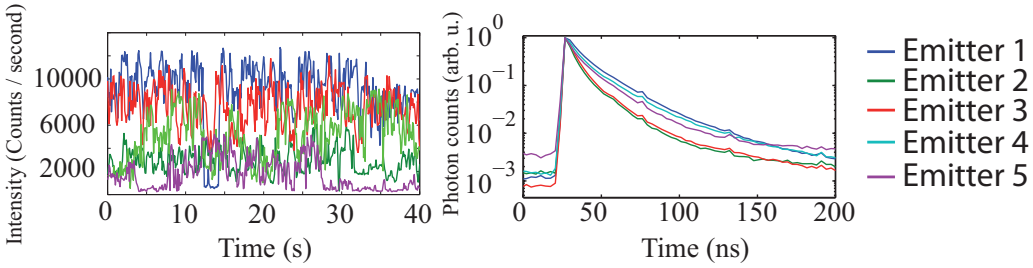

Figure 3.9: (a) Emission intensity variation as a function of time, and (b) Decay curve for in semilog scale 5 square nanoplatelets.

Figure 3.9(a) shows the emission intensity fluctuations under constant laser excitation. It is shown that, the emission of squared platelet is not perfectly stable (unlike the thick shell CdSe/CdS nanocrystals), a clear dark state is observed. Figure 3.9(b) displays the decay curves of the five measured squared nanoplatelets. The decay time of the squared nanoplatelets is around 10 ns. This decay time is faster than the CdSe/CdS quantum dots which have characteristic decay time around 25 ns.

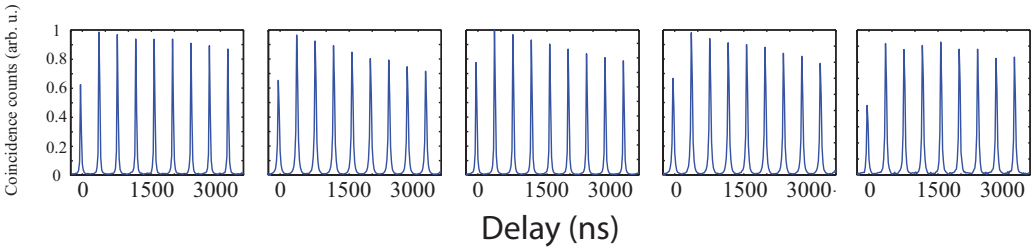

Figure 3.10: Antibunching measurements curve for the five squared nanoplatelets presented in Figure 3.9

Figure 3.10 plots the coincidence rate of photon counting on two photodiodes with different delay time, under pulsed excitation. The emission coincidence rate from the squared nanoplatelets is lower at zero delay ($\tau = 0$): the peak at $\tau = 0$ reaches between 0.5 and 0.8 with respect to the other peaks. This means that, for these platelets, the emission is partially antibunched. The much larger size of the platelets, as compared to spherical nanocrystals, leading to reduced Auger effect, likely explains the lower degree of antibunching for these emitters.

3.3 Square nanoplatelets

We now present the results for the combined polarization and radiation pattern measurements, starting with the square platelets.

On figure 3.11(a) are plotted for four platelets the polarization analysis curves (intensity at polarization angle α, normalized by the total intensity in order to account for the fluctuations of the total emission intensity). For all platelets (around 25), the emission is only weakly polarized. The dependence on α follows a $\cos^2$ law in agreement with eq. 3.4. A fit of the experimental curve gives a measured degree of polarization $\delta < 0.05$ for all emitters.

Such weak polarization indicates either a vertical 1D dipole ($\Theta = 0$), or an in-plane ($\Theta = 0$) 2D dipole. In order to discriminate between these possibilities, we plot the emission Fourier image of the same nanoplatelets in figure 3.5(b). For all platelets considered, the emission was highest at normal direction, in strong qualitative disagreement with the radiation pattern of a 1D dipole, suggesting a 2D dipole.

In order to confirm quantitatively the agreement of the radiation pattern with the hypothesis

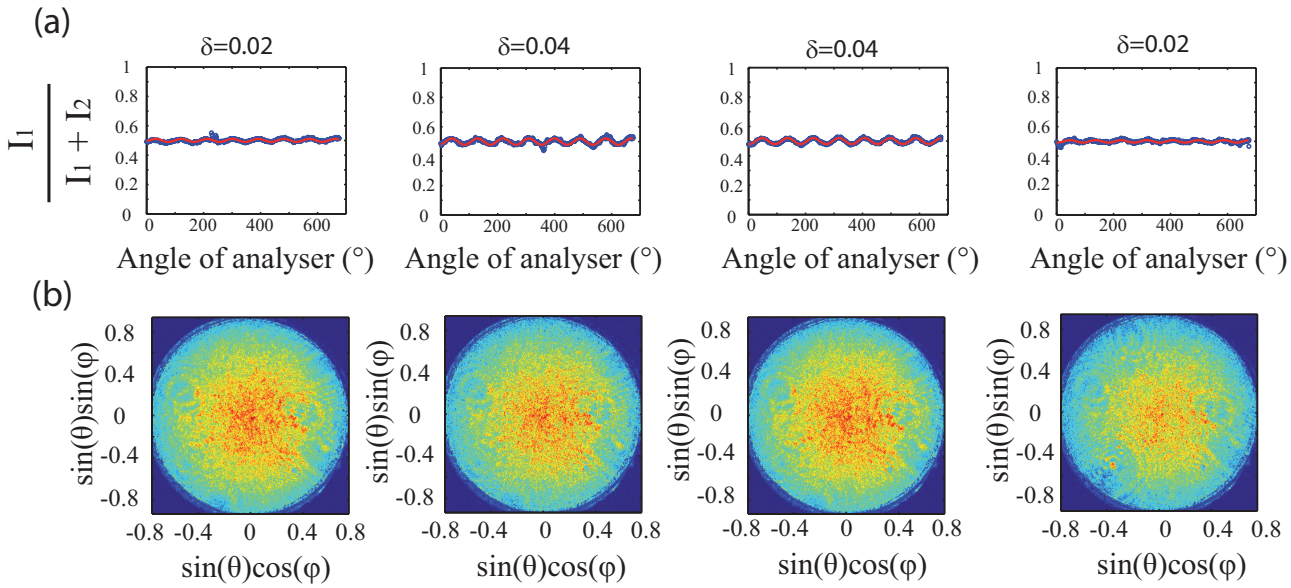

Figure 3.11: (a) Emission polarization measurements and (b) radiation pattern measurement for four square nanoplatelets. For (a), the blue dots are experimental data, the red curve is a fit following eq. 3.4 from which we find δ the degree of polarization.

of an in-plane ($\Theta = 0$) 2D dipole, detailed analysis has been performed of the emission pattern by comparing the measured emission pattern with the simulated emission pattern of a 2D dipole with $\Theta = 0$. Following the protocol developed in the previous chapter (including apodization factor), from the measured Fourier image we deduce the radiation pattern $dI/d\Omega$ and plot it on fig. 3.12(a), and compare it with a simulated figure.

Figure 3.12 (a) shows that the emission is similar (within imaging noise) for all angles ϕ, and decreases when θ increases. This indicates that the emission pattern has a symmetry axis, as expected for a 2D dipole at $\Theta = 0$ and in agreement with the theoretical data. We also plot on fig. 3.12(b) the radiation pattern profile along directions (chosen arbitrarily as the emission pattern is mostly centrosymmetric) $\phi = 0$ and 90°. Note that the experimental curves are obtained by interpolating from the (x, y) coordinates in the Fourier image to the (θ, ϕ) angular coordinates and averaging over +- 2.5° around the values $\phi = 0°$ and $\phi = 90°$: the points of low θ are averaged over less pixels of the camera, which explains why the radiation patterns present more noise for emission at low θ

The experimental curves are in excellent agreement with the simulation, confirming that the emission can be attributed to a 2D dipole which is horizontal on the sample. Most likely,

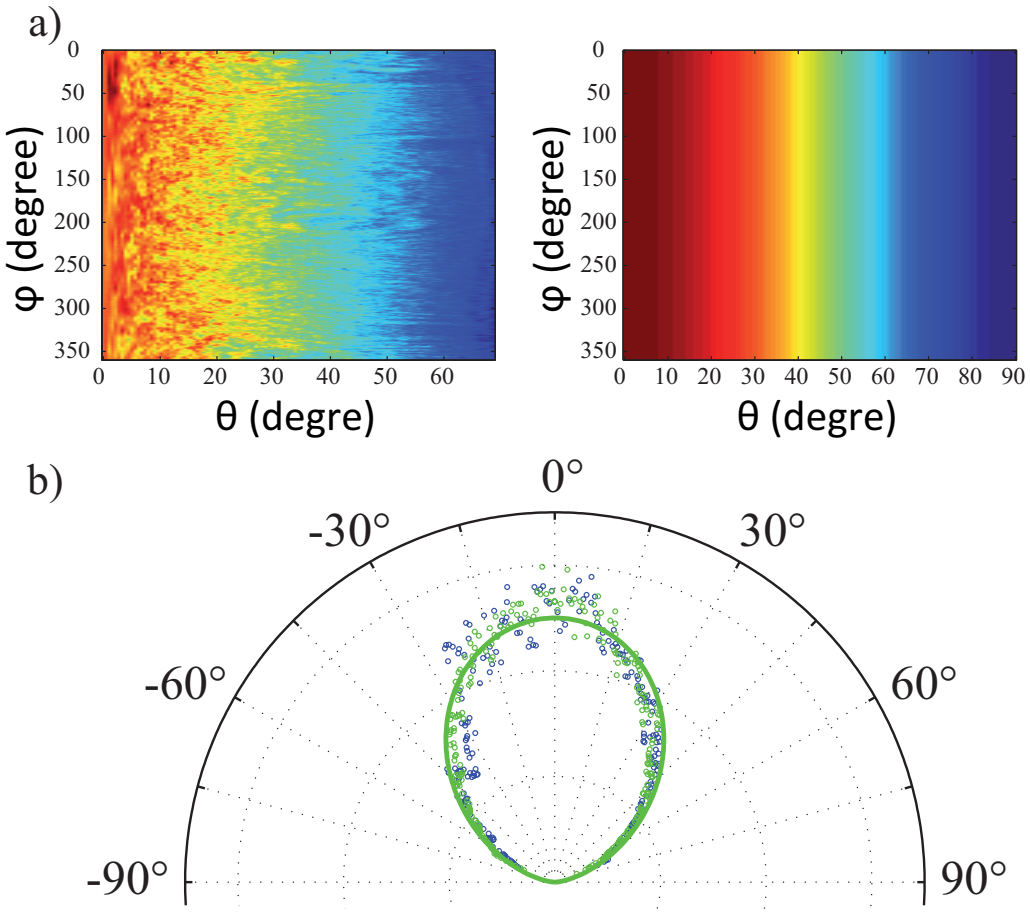

Figure 3.12: a) Measured (left) and simulated (right) emission diagram ($dI/d\Omega$) as a function of the emission directions θ and ϕ. b) Green solid line: Simulated emission pattern as a function of the emission angle θ, along direction $\phi = 0°$ (or 90°, as the pattern does not depend on ϕ). Dots : Measured radiation pattern as a function of angle θ, along directions $\phi = 0°$ (green) and $\phi = 90°$ (blue).

the nanoplatelet is deposited horizontally on the sample plane, and its 2D emission dipole lies parallel to the plane of the nanoplatelets. Note that the nanoplatelets will always deposit horizontally on the sample (as seen on the TEM image of fig. 3.7), unlike the spherical nanocrystals. This ensures a control of the orientation of the emitting dipole of these nanoplatelets, which will be the same for all platelets.

We have not discussed for the moment the possibility of a "3D" dipole, which would be a sum of a horizontal ($\Theta = 0$) 2D dipole and a vertical 1D dipole - or, in other words, a sum of three orthogonal dipoles of equal oscillator strengths. Figure 3.13 (a) shows the measured Fourier plane image for a square platelet and the theoretical Fourier image for a 2D dipole with $\Theta = 0$ and for a 3D dipole.

The emission pattern from a 2D and a 3D dipole are qualitatively quite similar, so that it is difficult to rule out completely the possibility of a 3D dipole. The reason is that the emission from a z-axis dipole contributes much less than the others to the total emission, because it does not emit in the z-axis direction.

However, a quantitative comparison of the radiation pattern profiles shows some difference. Figure 3.13 (b) shows the measured emission pattern along $\phi = 0°$ and $\phi = 90°$. The measured radiation pattern can be extremely well described by a 2D dipole at $\Theta = 0$. On the other hand, let us assume the emission from a 3D dipole and we define parameter η_3 as the ratio between oscillator strengths of the horizontal 2D dipole and vertical 1D dipole : $F_x = F_y$ and $\eta_3 = \frac{F_z}{F_x}$; then, figure 3.13 (c) compares the measured emission pattern with the calculated one with $\eta_3 = 1$ and $\eta_3 = 0.5$. The agreement with experiment is significantly less good when assuming a 3D dipole with $\eta_3 = 1$, but a lower value of η_3 (weaker 1D-dipole contribution) cannot be excluded.

3.4 Cubic nanoplatelets

We now consider the cubic nanoplatelets, deposited in the same manner on a gold-silica substrate. For most emitters, the polarization analysis and radiation patterns were, as shown in Figure 3.15(b), similar to the square platelets : the degree of polarization (Figure 3.15 (a), blue histogram bars) ranged between 0 and 0.1, and the radiation pattern was in excellent agreement

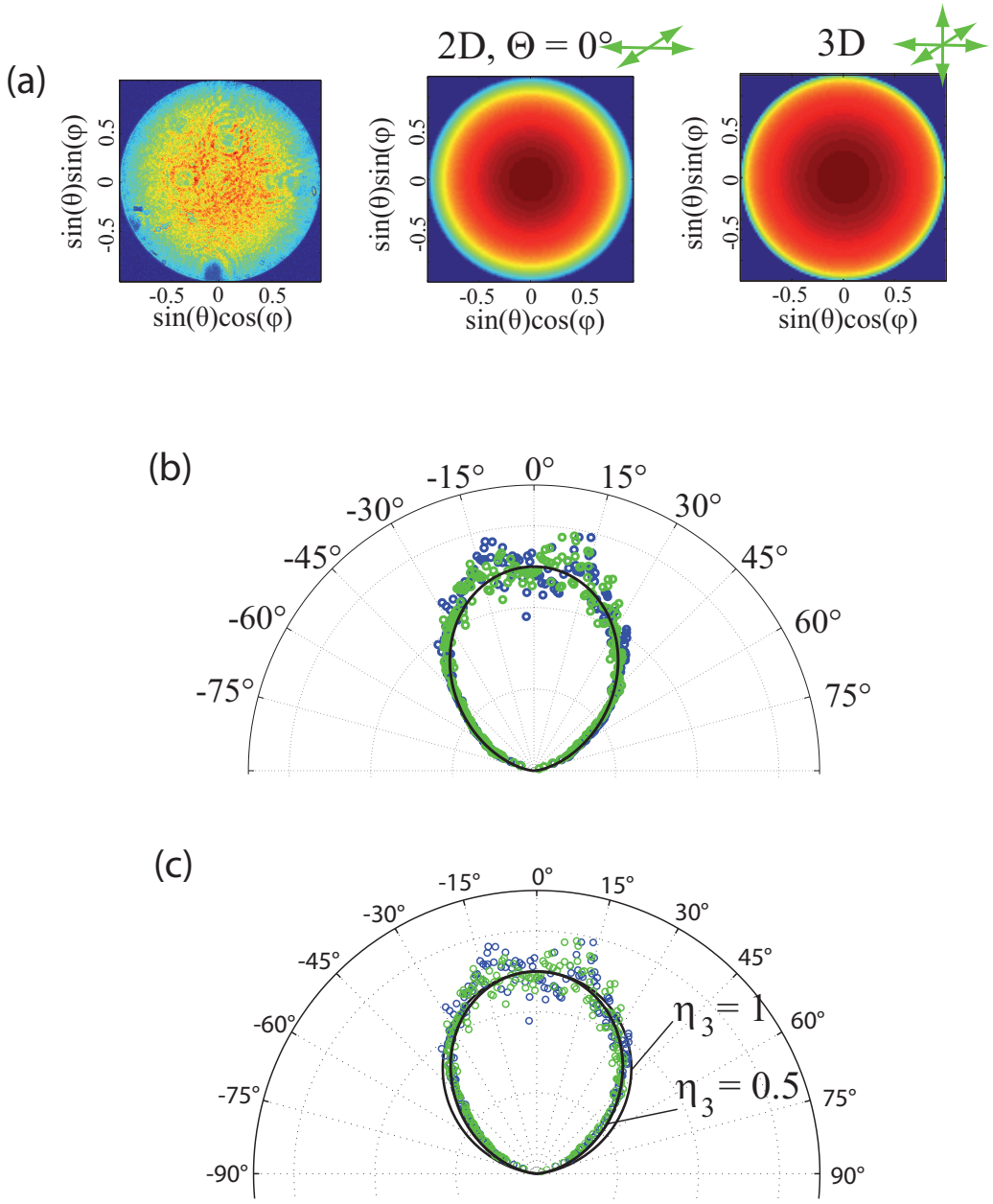

Figure 3.13: (a) Measured Fourier plane image for the square platelet and theoretical Fourier image for a 2D dipole at $\Theta = 0$ and for a 3D dipole (still in the configuration near gold-glass interface). (b) Radiation patterns measured along the $\phi = 0$ (blue dots) and $\phi = 90°$ (green dots) and simulated for a horizontal 2D dipole (line).(c) Same experimental data with simulated curve for a 2D dipole with a third z-axis contribution of relative amplitude η_3

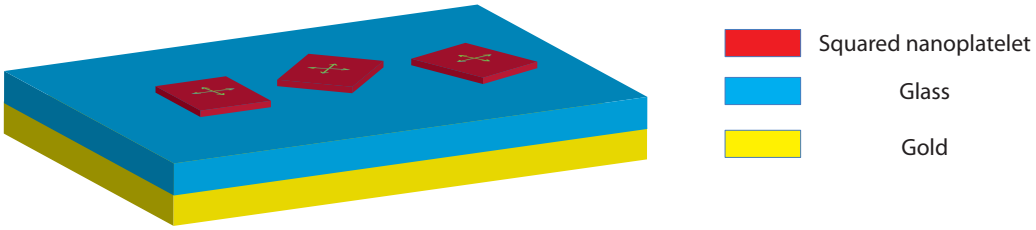

Figure 3.14: Schematic presentation of squared nanoplatelet deposited on the substrate surface with its associated dipoles

with a model of horizontal 2D dipole.

However, for some emitters (Figure 3.15 (c)), the emission was much more polarized, with values of δ between 0.78 and 0.88 (indicated by green bars on the histogram of Figure 3.15 (a)). Their in-plane orientation, which we label Φ_{max} (angle along which the emission is most strongly polarized), was randomly distributed in all directions. These emitters seem to be less bright than others. The proportion of emitters belonging to this sub-population can not be quantified precisely due to the difficulty of accurately characterizing weaker emitters, but it can be estimated to about 10 to 20 percent of the total platelet population (note that, in the histogram of figure 3.15 (a), the two blue and green populations were considered separately : the green population was obtained by targeting specifically the weaker emitters).

The Fourier image shows, for each emitter of this sub-population, two lobes located on either side of the Φ_{max} axis. We assign these observations to cubic nanoplatelets deposited with a vertical CdSe plane : if we label the orientation of a 2D dipole by the angle Θ of its dark axis, the latter population corresponds to values of Θ of 90°. For all considered emitters, the radiation pattern was in excellent agreement with a 2D dipole oriented along Φ_{max} and $\Theta = 90°$ as shown in Figure 3.15 (c). This also explains why these emitters are less bright than the others: the vertical dipole contribution emits less into the objective than the in-plane-dipole contribution.

We can discuss with more precision, for the platelets which are deposited on their side (like shown in Figure 3.16), the possibility that the platelets present a third weaker dipole. We have shown that the main contribution from the emitters with vertical CdSe plane is from a 2D dipole oriented along the CdSe plane. Let us assume that a third dipole contribution is also present, with relative amplitude η_3, oriented normal to the CdSe plane. We then have a

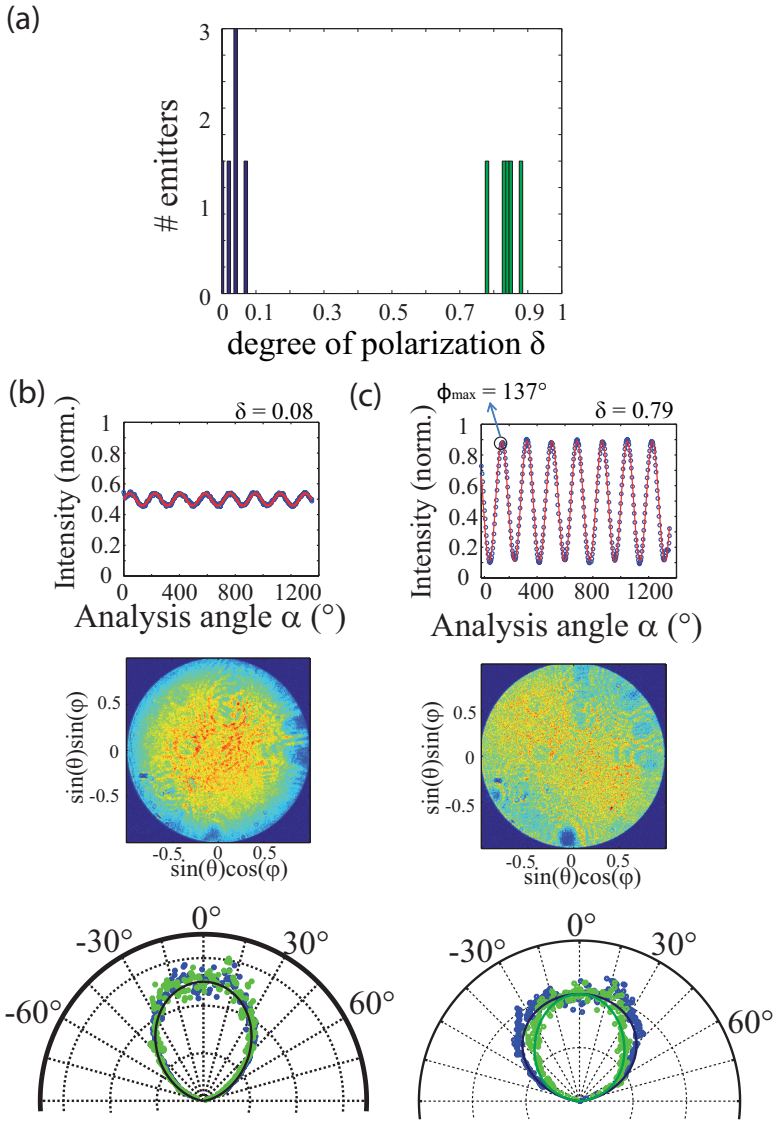

Figure 3.15: (a) Histograms of the values of degree of polarization δ measured for the horizontal (blue) and vertical standing (green) platelets. (b) and (c) : for 2 platelets, polarization analysis (top), Fourier image (middle) and radiation patterns (bottom ; along Φ_{max} in blue, $\Phi_{max} + 90°$ in green ; dots : experimental values ; lines ; theoretical values for a 2D dipole with $\Theta = 0°$ (b) or 90° (c)).

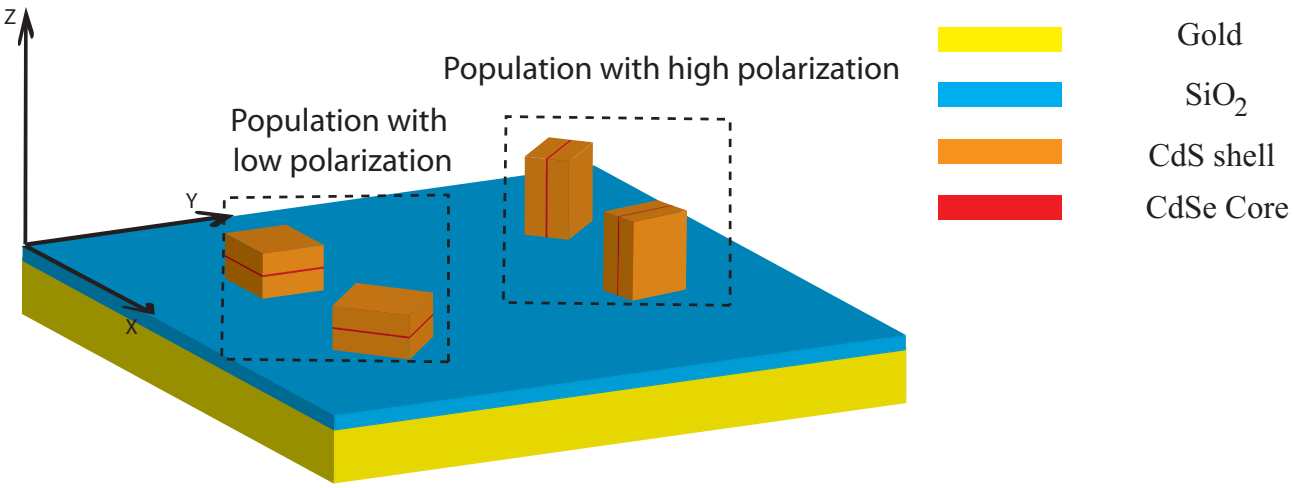

Figure 3.16: Schematic representation of cubic nanoplatelet deposited on substrate surface. For the left ones, the core plane of the nanoplatelet is parallel to the substrate, its emission polarization is low; for the right ones, the core plane of the nanoplatelet is perpendicular to the substrate, and its emission is highly polarized

2D dipole of orientation $(\Theta = \pi/2, \Phi = \Phi_{max} + \pi/2)$ (sum of two dipoles, one along $\Theta = 0$ and the other along $(\Theta = \pi/2, \Phi = \Phi_{max})$, of same amplitude) and a third 1D dipole along $(\Theta = \pi/2, \Phi = \Phi_{max} + \pi/2)$ of amplitude η_3 with respect to the 2 others. For values of η_3 above 0.1 (Figure 3.17), the quantitative disagreement with experimental data becomes significant. We can thus conclude that emission originates from a 2D dipole and exclude the presence of a third contribution of relative amplitude larger than 0.1.

From the above experiment data and calculations, it is demonstrated that the emission from the cubic nanoplatelets can be very well described by a 2D dipole oriented along the nanoplatelet plane. The existence of a third dipole (perpendicular to the nanoplatelet plane) can be excluded (relative oscillator strength smaller than 10%).

3.5 Rectangle nanoplatelets

We have left aside for the moment the residual polarization ($\delta < 0.1$) measured for the squared and horizontal cubic platelets. It can be assumed that this polarization is related to a slightly rectangular shape of the platelets. This is confirmed by considering a new sample of rectangular 20 x 10 nm^2 platelets. The emission polarization (Figure 3.18 (a) and (b)) now shows a higher

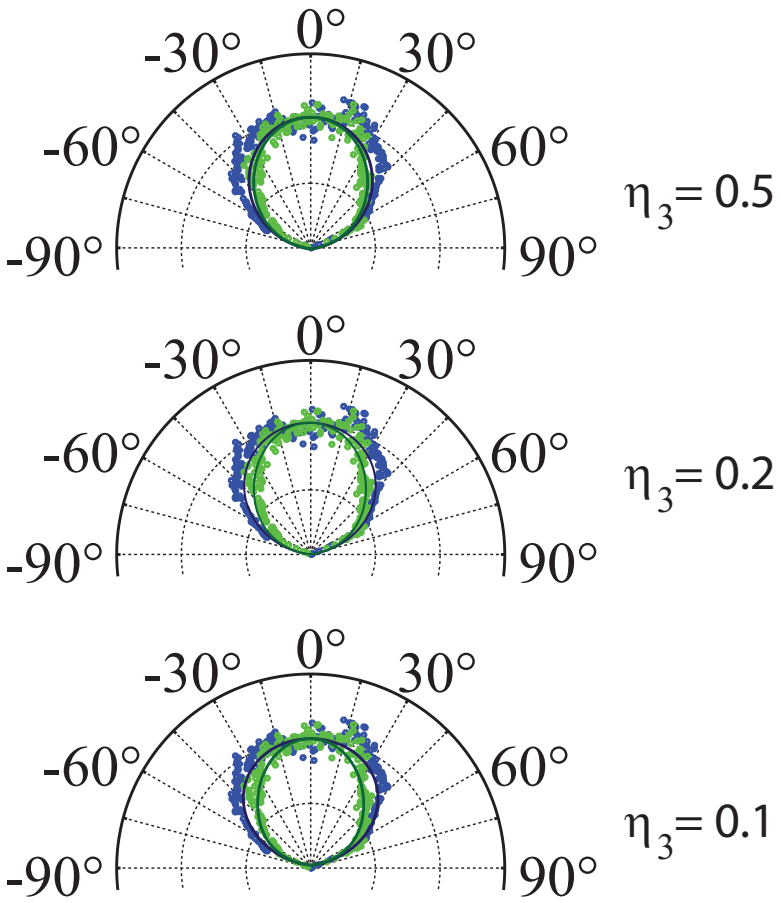

Figure 3.17: Radiation patterns along the Φ (blue) and $\Phi+90°$ (green) directions, experimental (dots) and simulated (lines) with a third z-axis component of amplitude $\eta_3 = 0.1$, 0.2 or 0.5.

degree of polarization (between 10% to 30%) compared with the squared nanoplatelets (between 0 to 10%). This suggests that the emission residual polarization is related mainly to the platelets aspect ratio.

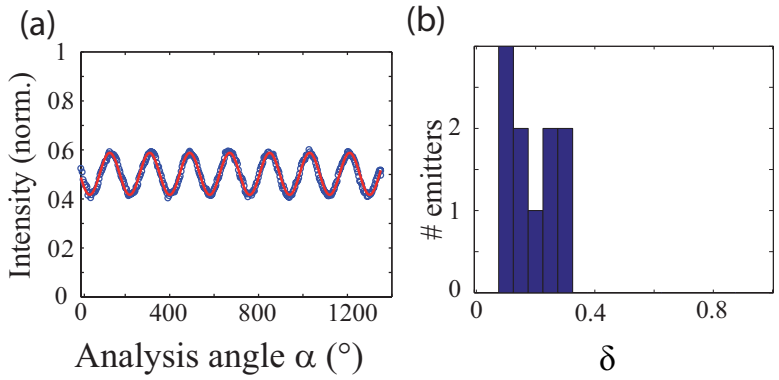

Figure 3.18: (a) Measured emission polarization analysis of a rectangular platelet. (b) Histogram of the measured values of degree of polarization δ for 10 rectangular platelets (on a gold substrate).

This polarization can be described by several mechanisms. One first hypothesis is that the 2D dipole is in fact not horizontal but tilted by a slight angle Θ, either due to defects or strains in the crystalline structure, or just because the platelet is not deposited exactly horizontally on the substrate, or some slight defect on the optics(objective orientation etc...). A second hypothesis is that the contributions of the two x and y dipoles are not exactly equal (let us label them $(1 + \eta_{12})/2$ and $(1 - \eta_{12})/2$ in relative units), either because they have different oscillator strengths due to different electron-hole wave functions overlaps, or because one of the dipoles is amplified with respect to the other by dielectric antenna effects.

The present experimental configuration does not allow us to discriminate between these two hypotheses because they would lead to very similar radiation patterns. However, the difference between these two cases appears clearly when the gold-glass substrate is replaced by a glass substrate (with now the oil objective introduced under the glass substrate, and the platelets on the glass surface directly: Figure 3.19 (a)). In both cases, the theoretical Fourier image (Figure 3.19 (b)) shows a sharp ring at the critical angle corresponding to the coupling between the evanescent wave at lower index material with the propagative wave at higher index material. However, a clear qualitative difference appears between the two images : for the the first case

with $\Theta = 30°$, there is a dissymmetry for the emission inside this ring. For the second case with $\eta_{12} = 0.2$, on the other hand, emission inside the ring remains symmetric but the ring itself is now non isotropic.

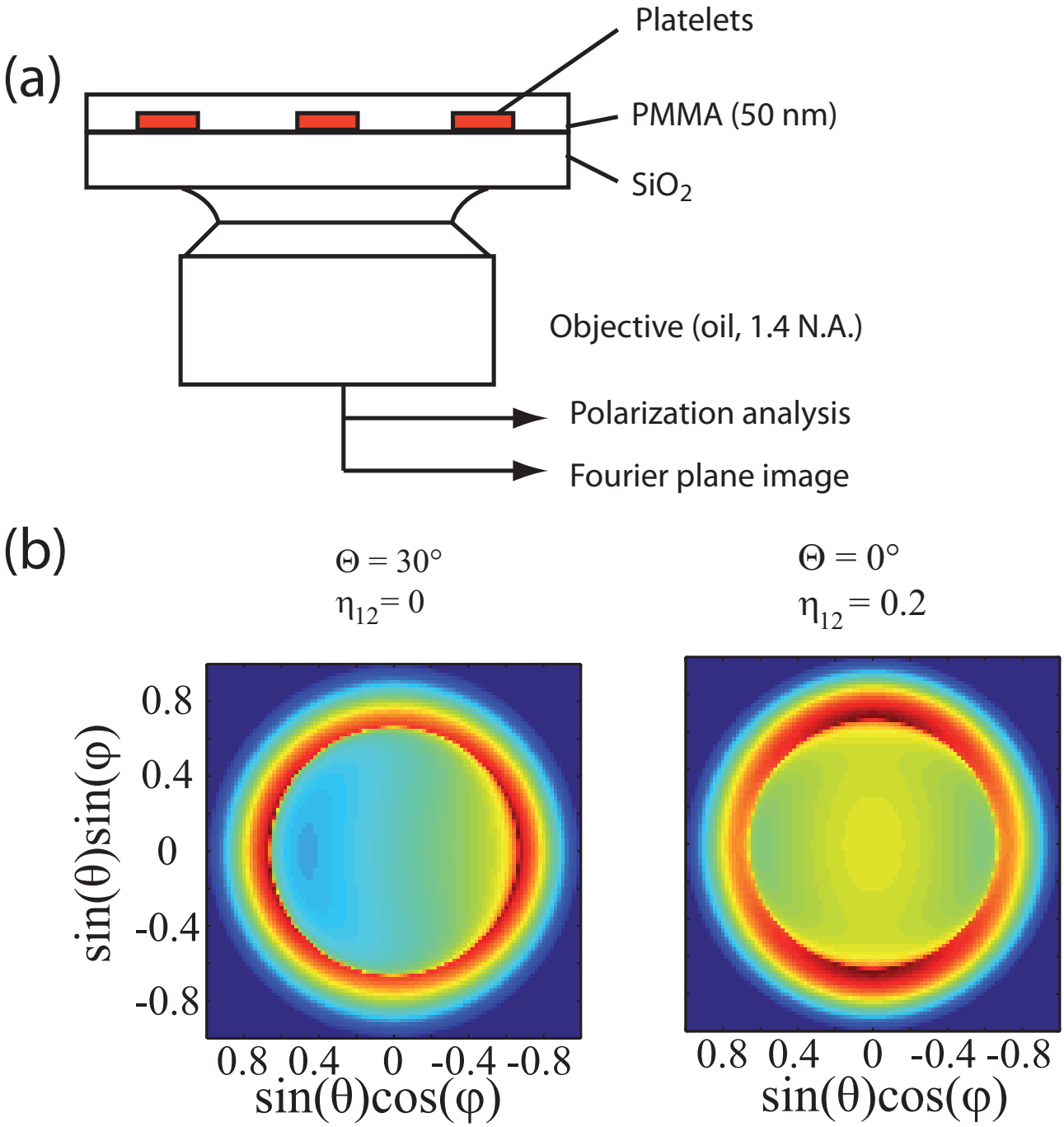

Figure 3.19: (a) Schematic of the new experimental configuration. (b) Theoretical Fourier image, in this configuration, of a 2D x-y dipole tilted by $\Theta = 30°$ (left) or disymetrized by a factor η_{12} (right).

The rectangle nanoplatelets are then deposited on the cover glass substrate($170\mu m$) and the detection is performed by an oil immersion objective with 1.4 as numerical aperture on the other side of the glass substrate. Figure 3.20 (a) shows the measured emission polarization and emission pattern. This image is qualitatively in disagreement with the first hypothesis and in better agreement with the second model. We then calculated the theoretical relation between the factor η_{12} mentioned above with the emission degree of polarization as shown in Figure 3.20(b). A measured value of $\delta = 0.15$ corresponds to $\eta_{12} = 0.075$. Figure 3.20 (c) shows excellent agreement between the measured emission pattern from a rectangle nanoplatelet and the calculated emission pattern from a 2D dipole with $\eta_{12} = 0.075$ orientated at $\Theta = 0$ and $\Phi = \Phi_{max}$, confirming the description of the platelets by a sum of two orthogonal dipoles with different oscillator strengths.

Moreover, it is possible to determine the η_{12} factor from the emission pattern measurement. For the platelet on Figure 3.21, the measured emission pattern shows a best fit when $\eta_{12} = 0.23$. And when $\eta_{12} < 0.15$ or $\eta_{12} > 0.3$, the fit is clearly less good. The η_{12} factor for this emitter is then determined to be between 0.15 - 0.3. This method give us a η_{12} factor with a precision of $\pm 7\%$. The precision is principally limited by the singnal - to - noise ratio for the emission at small angle (as explained before). The η_{12} value can also be determined by emission polarisation measurements, the precision is about $\pm 5\%$.

Finally, figure 3.20(d) compares the value η_{12} extracted from emission polarization measurements (theoretical correspondence between δ and η_{12}) and the values η_{12} extracted from the emission pattern, for 4 different rectangle nanoplatelets. These values range from 0.1 to 0.2, with an excellent agreement between the two values, confirming the validity of our model description of these emitters and the quantitative accuracy of their characterization. Further studies on rectangle nanoplatelets with different aspect ratios would give a more precise idea of the mechanism by which the rectangular shape influences the emission dipole.

3.6 Conclusion

We have applied in this chapter a combination of polarization and radiation pattern analysis on single emitters to characterize three nanoplatelet samples. The measurements were performed under conditions (substrate, type of objective) chosen in order to best discriminate between

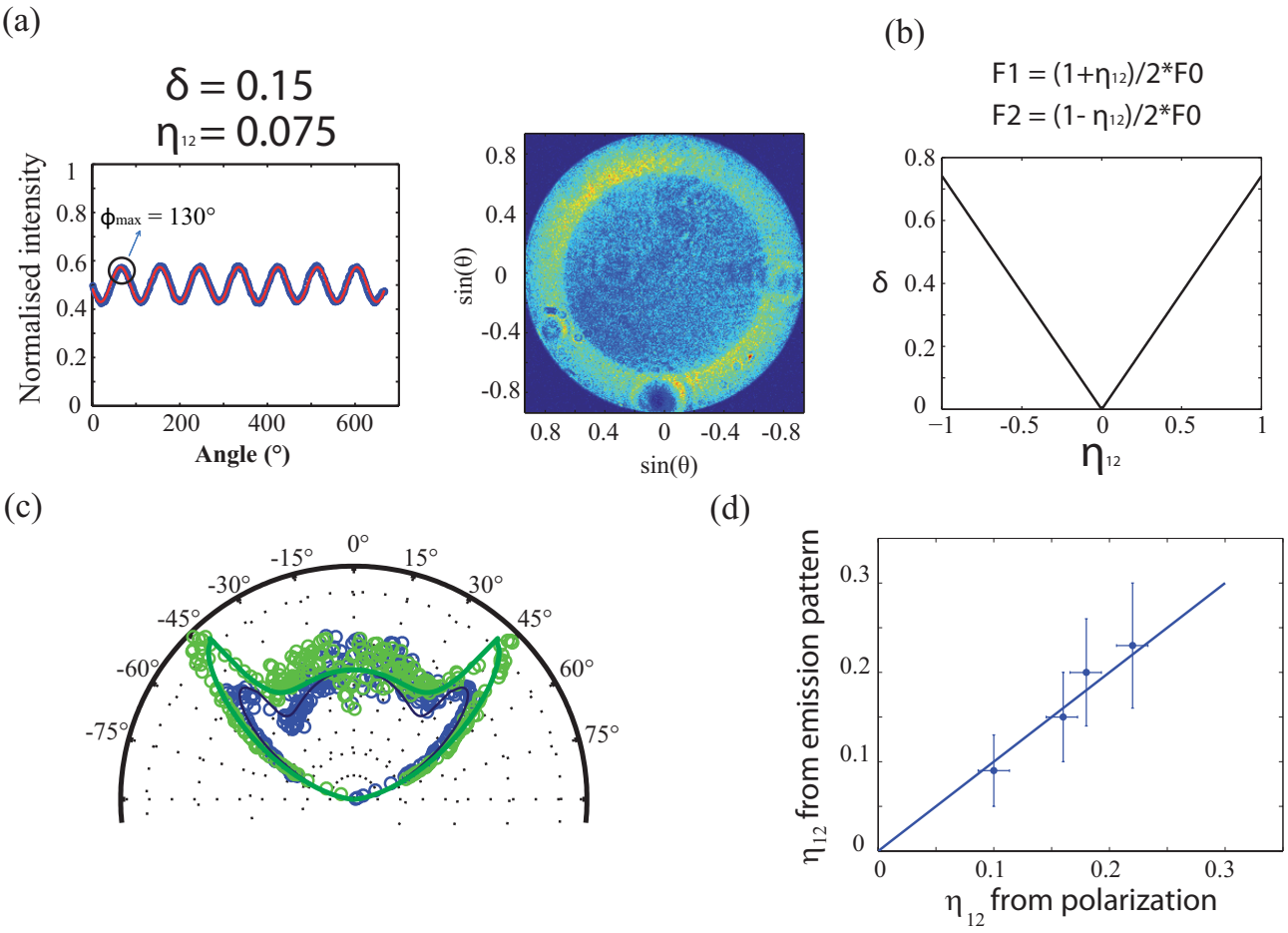

Figure 3.20: (a) Theoretical relation between the oscillator strength ratio η_{12} and the emission degree of polarization δ (in the glass-substrate configuration). (b) Measured emission polarization and emission pattern for a rectangle nanoplatelet deposited on a glass surface. (c) Dots: measured emission pattern along Φ_{max} (green) and $\Phi_{max} + 90°$ (blue). Lines : calculated emission pattern from a horizontal ($\Theta = 0$) 2D dipole with $\eta_{12} = 0.075$ along direction Φ_{max} (green) and $\Phi_{max} + 90°$(blue). (d) η_{12} values extracted from measurements of emission polarization (x axis), and emission pattern (y aixs) respectively

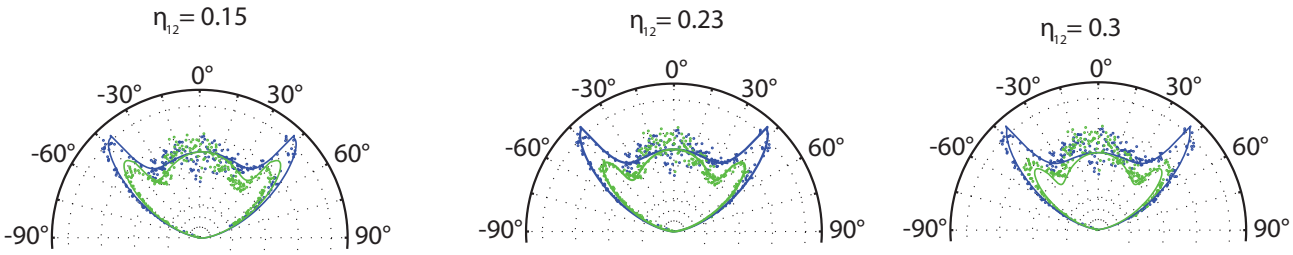

Figure 3.21: Comparaision of measured emission pattern from a rectangle nanoplatelet at $\Phi = \Phi_{max}$ and $\Phi = \Phi_{max} + 90°$ with calculated emission pattern with a 2D dipole orientated at $\Theta = 90°$ and $\Phi = \Phi_{max}$ with Φ_{max} extracted from emission polarization measurement from the same emitter

possible hypotheses : first, between 1D and 2D dipoles ; then between a tilted ($\Theta \neq 0$) and an asymmetric ($\eta_{12} \neq 0$) 2D dipole. We obtained a broad set of experimental results which could be explained very consistently by a 2D dipole model. This approach has proven remarkably rich, and further improvements can probably be expected as more questions arise about these nanoplatelets.

The square nanoplatelets were described by a 2D dipole. For the cubic nanoplatelets, which have the same square CdSe core but a thicker CdS shell, the same 2D dipole structure was found. However, for some cubic structures, this 2D dipole was along a plane normal to the sample plane, probably because the structures were deposited on their side, while all the square platelets were deposited horizontally. Comparing the two orientations of deposition for the cubic platelets provided further analysis which excluded the possibility of a third dipole normal to the platelet. The square platelets thus provide a possibility to have emitters with deterministically identical 2D-dipole orientation ; their radiation pattern can be oriented normal to the sample plane, in a $\pm 30^o$ cone which can be well collected by a microscope objective. As for the cubic platelets, they give a choice between two very distinct orientations.

Analysis of the rectangular nanoplatelets provides further insight into the emission properties of these platelets. The elongated shape of the platelets seems to be related to a higher degree of polarization. This was very well described by an asymmetric 2D dipole ; it remains to be determined whether this asymmetry is caused by an asymmetric confinement of the excitons inside the platelet, or to an optical antenna effect by the asymmetric shape of the dielectric platelet. Similar questions have arisen in order to explain the imperfect 1D-dipole emission

from dot-in-rods. More studies with different samples of nanoplatelets, different geometries and different aspect ratios could discriminate between these mechanisms.

Bibliography

[1] T. D. Harris J. J. Macklin, J. K. Trautman and L. E. Brus. Imaging and timeresolved spectroscopy of single molecules at an interface. *Science*, 272(5259):272–255, 1996.

[2] D. S. Chemla P. R. Selvin T. Ha, Th. Enderle and S. Weisss. Single molecule dynamics studied by polarization modulation. *Phys. Rev. Lett*, 77(4):3979, 1996.

[3] P. Spinicelli A. Fiore J.P. Hermier L. Manna R. Cingolani E. Giacobino M. De Vittorio F. Pisanello, L. Martiradonna and A. Bramati. Dots-in-rods as polarized single photon sources. *Superlattices and Microstructures*, 47(5):165–169, 2010.

[4] D. Goorskey M. Xiao Z. A. Peng X. Chen, A. Nazzal and X. Pengi. Polarization spectroscopy of single cdse quantum rods. *Phys. Rev. B*, 64(24):245304, 2001.

[5] G. Menagen A. Sitt, A. Salant and U. Banin. Highly emissive nano rod-in-rod heterostructures with strong linear polarization. *Nano Lett*, 11(6):2054–2060, 2011.

[6] A. Sitt A. Faust I. Hadar, G. B. Hitin and U. Banin. Polarization properties of semiconductor nanorod heterostructures : from single particles to the ensemble. *J. Phys. Chem. Lett.*, 4(3):502–507, 2013.

[7] Clotilde Lethiec, Julien Laverdant, Henri Vallon, Clémentine Javaux, Benoît Dubertret, Jean-Marc Frigerio, Catherine Schwob, Laurent Coolen, and Agnès Maître. Measurement of three-dimensional dipole orientation of a single fluorescent nanoemitter by emission polarization analysis. *Phys. Rev. X*, 4(2):021037, 2013.

[8] Al. L. Efros, M.Rosen, M.Kuno, M. Nirmal, D. J. Norris, and M. Bawendi. Band-edge exciton in quantum dots of semiconductors with a degenerate valence band: Dark and bright exciton states. *Physical Review B*, 54(7):4843–4856, 1996.

[9] J. Jasny and J. Sepiol. Single molecules observed by immersion mirror objective. a nouvel method of finding orientation of a radiating dipole. *Chem. Phys. Lett.*, 273(2):439–443, 1997.

[10] M. Bohmer and J. Enderlein. Orientation imaging of single molecules by wide-field epifluorescence microscopy. *J. Opt. Soc. Am B*, 20(5):554–559, 1966.

[11] Clothilde Lethiec. Emission polarise de nanometteurs : excitation de plasmons sur une surface mtallique. *PhD thesis of University Pierre et Marie Curie - Paris VI*, 2014.

[12] W. Lukosz. Light emission by magnetic and electric dipoles close to a plane dielectric interface. iii. radiation patterns of dipoles with arbitrary orientation. *J. Opt. Soc. Am*, 42(3):18, 1981.

[13] W. Lukosz. Light emission by multipole sources in thin layers. i. radiation patterns of electric and magnetic dipoles. *J. Opt. Soc. Am*, 69(5):11, 1979.

[14] Mickal D. Tessier, Clmentine Javaux, Ivan Maksimovic, Vincent Loriette, and Benoit Dubertret. Spectroscopy of single cdse nanoplatelets. *ACS Nano*, 6(8):6751–6758, 2012.

Conclusion

The emission properties of fluorescent nano-emitters, such as their decay rate, radiation pattern or polarization, depend on the emitter itself (its emission wavelength, its orientation, its 1D or 2D dipole nature) but also on its optical environment. In the first chapter of this thesis, I described the emission properties of colloidal spherical nanocrystals, and I presented the microphotoluminescence setup which I installed during my PhD to characterize such emission properties. In particular, I described how imaging in the Fourier plane can be used to measure the radiation pattern, possibly in combination with spectroscopic analysis. In the second chapter, the luminescence from nanocrystals inside an optical 0D Tamm structure was used to analyze the optical properties of such a photonic structure. In the third chapter, on the other hand, the optical environment was used to characterize the emission properties (1D or 2D dipole) of single colloidal nanoplatelets : we tailored the environment so that the polarization and radiation pattern would be different for a 1D and 2D dipole.

We fabricated 2D and 0D Tamm structures coupled to an ensemble of colloidal nanocrystals by depositing a dense layer of nanocrystals on a Bragg mirror and covering it by a layer of silica and either a layer (2D structure) or 2- to 10-μm disks (0D structure) of silver. The fluorescence from these structures followed the Tamm states dispersion law : all of the emission occurred into the optical Tamm states, indicating a good coupling of the nanocrystals with the Tamm states. The lateral confinement of the Tamm states in the 0D structures was evidenced by a discretization of the dispersion relation for the smaller disks. These structures were modeled either by transfer matrix method (2D structures) or finite-elements method (0D structures). A good description of the experimental observations was obtained, with some differences likely due to fabrication imperfections.

We then placed a pinhole in an intermediate image plane, which allowed us to select spatially

a sub portion of the 0D Tamm structure and image its dispersion relation. This method, which combines spatial and angular measurement, requires care as the spatial and angular resolutions are related by diffraction laws. We showed that different portions of the Tamm structure radiate to different directions, which was well reproduced by our simulations. This provides in fact a map of the electric field phase gradient in the Tamm structure. This method could be used to characterize many other kinds of photonic structures.

We also excited different points of the 0D Tamm structures. Depending on the position of the excited nanocrystals, a different radiation can be obtained : nanocrystals on the right side of the disk will emit preferentially to the left direction. For a single emitter inserted in a 0D Tamm structure, a control of the radiation direction can thus be obtained by choosing the position of the emitter inside the structure, with a low required level of precision. Other aspects of the coupling of a single emitter to a nanphotonic structure, such as temperature dependence, could also be studied.

In the last part of this PhD, we considered the fluorescence of colloidal semiconductor nanoplatelets. These structures are obtained by chemical synthesis with an excellent control and monodispersity of their thickness, as evidence by the extremely narrow ensemble emission spectrum. Sandwich core-shell CdSe/CdS structures were considered, which allowed better photostability. Various lateral dimensions (square and rectangle) and shell thicknesses (square and cubic platelets) were considered.

We deposited these emitters on gold-silica substrates and calculated that, in these conditions, 1D and 2D dipoles with orientation $\Theta = 0$ would show very different radiation patterns. Experimentally, we measured for the square platelets almost no polarization, corresponding to $\Theta \simeq 0$. The radiation pattern was very different from the 1D dipole, and in much better agreement with a 2D dipole with its two degenerate dipoles along a horizontal plane. The emission pattern is mostly into the vertical direction for all the platelets, which allows a deterministic control of the emission direction.

For the cubic platelets, the emission dipole could also be well described by a 2D dipole. Some platelets were deposited on their side, with a vertical CdSe plane. For these platelets, the emission could be well described by a 2D dipole with $\Theta = 90^o$, confirming the 2D-dipole nature of these emitters. The existence of a strong third dipolar component normal to the 2D

dipole could be excluded. These cubic platelets provide, unlike the square ones, the possibility to have emitters standing on their side ; then there is one vertical dipole component, which can be necessary for coupling to some plasmonic structures.

For the rectangular platelets, a more polarized emission was observed. It could be described, based on polarization and radiation pattern comparison, by a 2D dipole with stronger oscillator strength for one dipole than the other. The origin of this asymmetry is not clear yet, as it could be attributed either to different wave functions of the radiating electron-hole pair, or to an optical antenna effect by the dielectric nanoplatelet structure. More information could be obtained by comparing platelets with different sizes and aspect ratios, possibly in different optical environments. Ultimately, a comparison with Atomic Force Microscopy (AFM) or SEM data would provide the most complete relation between the platelet's structure and its optical properties.